Ph.D. Program in Civil, Chemical and Environmental Engineering

Curriculum in Structural and Geotechnical Engineering, Mechanics and Materials

Department of Civil, Chemical and Environmental Engineering

Polytechnic School, University of Genoa, Italy.

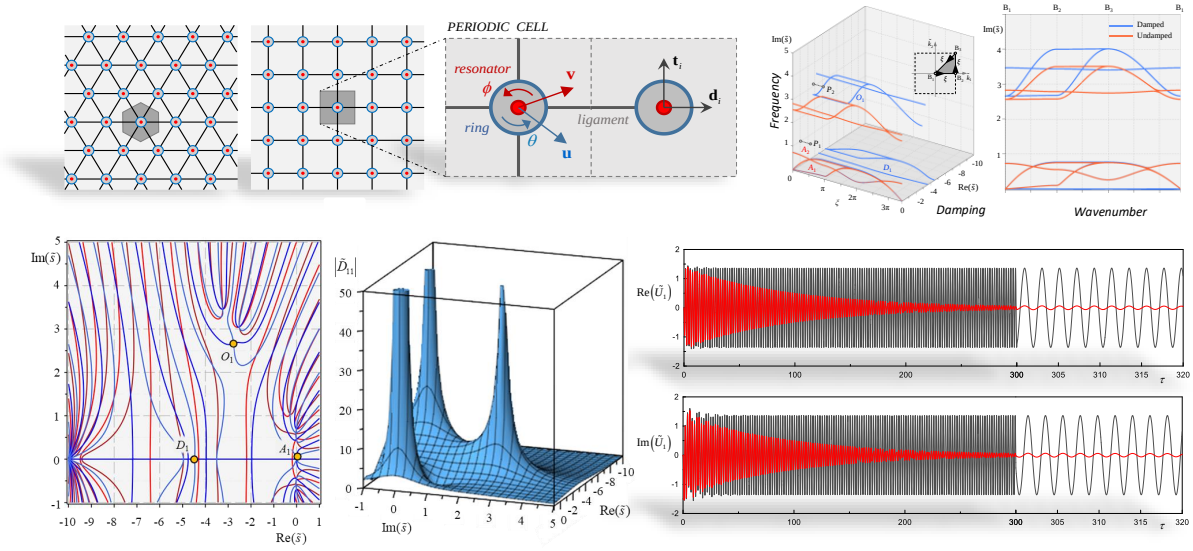

Free and forced propagation of Bloch waves in viscoelastic beam lattices

Francesca Vadalà

FREE AND FORCED PROPAGATION OF BLOCH WAVES

IN VISCOELASTIC BEAM LATTICES

BY

FRANCESCA VADALÀ

Dissertation discussed in partial fulfillment of
the requirements for the Degree of

DOCTOR OF PHILOSOPHY

Civil, Chemical and Environmental Engineering
curriculum in Structural and Geotechnical Engineering, Mechanics and Materials,
Department of Civil, Chemical and Environmental Engineering, University of Genoa, Italy

March, 2020

Advisers:
Prof. Marco Lepidi – Department of Civil, Chemical and Environmental Engineering, University of Genoa
Prof. Andrea Bacigalupo – Department of Civil, Chemical and Environmental Engineering, University of Genoa

External Reviewers:
Prof. Valery P. Smyshlyaev – Department of Mathematics, University College London
Prof. Michele Brun – Department of Mechanical, Chemical and Material Engineering, University of Cagliari

Examination Committee:
Prof. Massimiliano Gei – School of Engineering, Cardiff University
Prof. Francesco Romeo – Department of Structural and Geotechnical Engineering, Sapienza University of Rome
Prof. Federica Tubino – Department of Civil, Chemical and Environmental Engineering, University of Genoa

Ph.D. program in Civil, Chemical and Environmental Engineering

Curriculum in Structural and Geotechnical Engineering, Mechanics and Materials

Cycle XXXII

ABSTRACT

Beam lattice materials can be characterized by a periodic microstructure realizing a geometrically regular pattern of elementary cells. Within this framework, governing the free and forced wave propagation by means of spectral design techniques and/or energy dissipation mechanisms is a major issue of theoretical interest with applications in aerospace, chemical, naval, biomedical engineering.

The first part of the Thesis addresses the free propagation of Bloch waves in non-dissipative microstructured cellular materials. Focus is on the alternative formulations suited to describe the wave propagation in the bidimensional infinite material domain, according to the classic canons of linear solid or structural mechanics. Adopting the centrosymmetric tetrachiral cell as prototypical periodic topology, the frequency dispersion spectrum is obtained by applying the Floquet-Bloch theory. The dispersion spectrum resulting from a synthetic Lagrangian beam lattice formulation is compared with its counterpart derived from different continuous models (high-fidelity first-order heterogeneous and equivalent homogenized micropolar continua). Asymptotic perturbation-based approximations and numerical spectral solutions are compared and cross-validated. Adopting the low-frequency band gaps of the dispersion spectrum as functional targets, parametric analyses are carried out to highlight the descriptive limits of the synthetic models and to explore the enlarged parameter space described by high-fidelity models. The microstructural design or tuning of the mechanical properties of the cellular microstructure is employed to successfully verify the wave filtering functionality of the tetrachiral material.

Alternatively, band gaps in the material spectrum can be opened at target center frequencies by using metamaterials with inertial resonators. Based on these motivations, in the second part of the Thesis, a general dynamic formulation is presented for determining the dispersion properties of viscoelastic metamaterials, equipped with local dissipative resonators. The linear mechanism of local resonance is realized by tuning periodic auxiliary masses, viscoelastically coupled with the beam lattice microstructure. As peculiar aspect, the viscoelastic coupling is derived by a mechanical formulation based on the Boltzmann superposition integral, whose kernel is approximated by a Prony series. Consequently, the free propagation of damped Bloch waves is governed by a linear homogeneous system of integro-differential equations of motion. Therefore, differential equations of motion with frequency-dependent coefficients are obtained by applying the bilateral Laplace transform. The corresponding complex-valued branches characterizing the dispersion spectrum are determined and parametrically analyzed. Particularly, the spectra corresponding to Taylor series approximations of the equation coefficients are investigated. The standard dynamic equations with linear viscous damping are recovered at the first order approximation. Increasing approximation orders determine non-negligible spectral effects, including the occurrence of pure damping spectral branches. Finally, the forced response to harmonic single frequency external forces in the frequency and the time domains is investigated. The response in the time domain is obtained by applying the inverse bilateral Laplace transform. The metamaterial responses to non-resonant, resonant and quasi-resonant external forces are compared and discussed from a qualitative and quantitative viewpoint.

INDEX

1. INTRODUCTION 1
2. CRYSTAL LATTICE 9
2.1. Undamped monoatomic lattice material 9
2.2. Damped monoatomic lattice material 12
2.3. Undamped biatomic lattice material 17
2.4. Damped biatomic lattice material 21
2.5. Undamped biatomic lattice metamaterial 25
2.6. Damped biatomic lattice metamaterial 28
3. ELASTIC BEAM LATTICE 33
3.1. Tetrachiral material 34
3.1.1. Beam lattice model 34
3.1.2. Microscopic first order continuum model 38
3.1.3. Homogenized micropolar continuum model 39
3.2. Wave propagation 41
3.2.1. Dispersion spectrum 41
3.2.2. Perturbation solution 42
3.3. Parametric analysis 46
3.3.1. Mechanical tuning 51
3.3.2. Performance as acoustic filters 54
3.4. Parametric optimization 56
4. INERTIAL METAMATERIAL WITH VISCOELASTIC RESONATORS 61
4.1. Governing equations of the beam lattice model 62
4.2. In-plane Bloch waves 64
4.3. Free wave propagation 66
4.3.1. Complex-valued dispersion spectra 68
4.4. Asymptotic approximation 72
4.5. Forced wave propagation 76
4.5.1. Compliance matrix 77
4.5.2. Forced response 78
5. CONCLUSIONS 85
REFERENCES 91

CHAPTER 1

INTRODUCTION

Microstructured material and metamaterial science is a challenging frontier of theoretical and applied research that is currently attracting growing interest by the scientific community of solid and structural mechanicians (Fleck et al., 2010; Meza et al., 2015; Schaedler and Carter, 2016; Kadic et al., 2019). Specifically, the conceptualization and development of novel materials, characterized by smart or unconventional functionalities, are continuously propelled by the recent extraordinary developments in the technological fields of super-computing, micro-engineering and high-precision manufacturing (Lee et al., 2012; Rashed et al., 2016; Sha et al., 2018). As valuable result of this successful research trend, a new generation of architected composites is deeply transforming and rapidly remodeling the traditional paradigms of rational design in a variety of technical multidisciplinary applications across all the classical and advanced branches of mechanics, including – among the others – extreme mechanics, nanomechanics, mechatronics, acoustics, thermomechanics, biomechanics (Zheng et al., 2014; Overvelde et al., 2017; De Bellis et al., 2019; Wu et al., 2019; Zadpoor, 2019). In general, the microstructured materials are heterogeneous at nano/micro scale in which different constituents (or phases) are distinguished (Figure 1.1).

Basing on the geometry and mechanical properties of the microstructure, the materials can be classified in periodic and non-periodic microstructured materials. Periodic materials are characterized by a repetitive microstructure realizing a regular pattern of elementary cells. Regular masonry and laminated composites are some examples of periodic materials having a rigid phase with dominant volumetric fraction and a soft phase with a vanishing volume fraction. Other very common periodic microstructured materials are characterized by an ordered microstructure that can be composed by ligaments, as in the case of re-entrant honeycomb structures (Figure 1.2a), or by composite assemblies of rigid elements (cylindrical rings or disks), connected with light and flexible ligaments. The periodic materials made by cylinders connected with tangential ligaments can be characterized by chiral or anti-chiral topologies (Figure 1.2b,c) (Prall and Lakes, 1997; Alderson et al., 2010; Lorato et al., 2010; Cicala et al., 2012; Liu

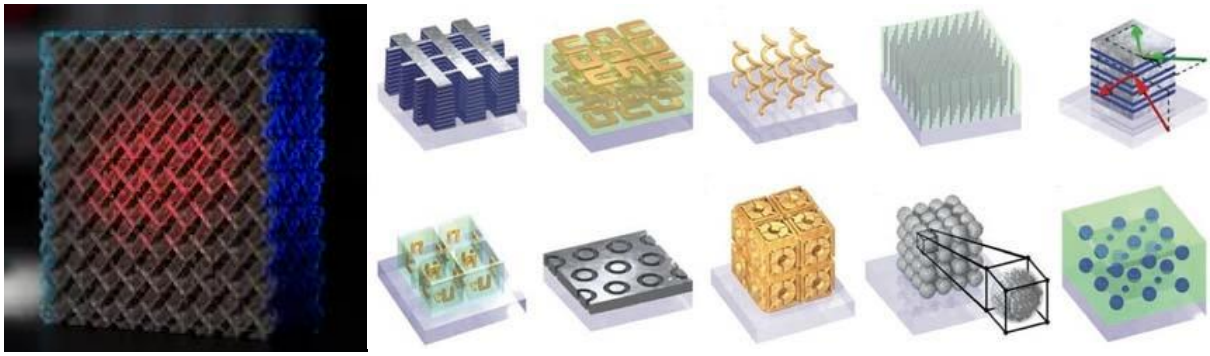

Figure 1.1 Picture and sketches of microstructured materials.

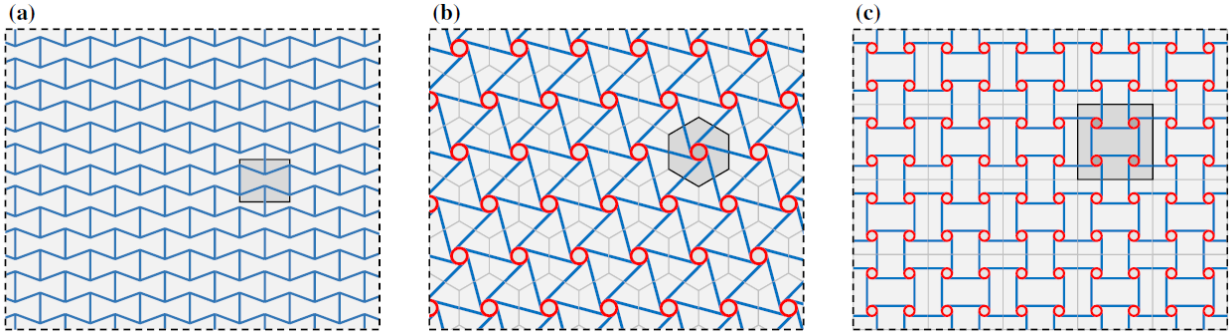

Figure 1.2 Periodic materials: (a) reentrant honeycomb, (b), hexachiral and (c) anti-tetrachiral topologies (Lepidi and Bacigalupo, 2017).

et al., 2012; Chen et al., 2013; Gatt et al., 2013). The materials with a chiral configuration display a rotational symmetry, while the materials with an anti-chiral configuration display reflective and rotational symmetry (Abramovitch et al., 2010). Another interesting periodic display are realized by 2D sheets with predefined crease patterns (origami materials) or by introducing arrays of cuts into thin sheets of the material (kirigami materials) (Scarpa et al., 2013; Wei et al., 2013; Cheung et al., 2014; Lv et al., 2014; Shyu at al., 2015; Carta et al., 2016; Chen et al., 2016; Neville et al., 2016). Non-periodic materials are not characterized by a repetitive microstructure. Among the non-periodic microstructured materials there are the foams characterized by a microstructure with open cells consisting of an interconnected network of ligaments that form along the edges of randomly packed cells that evolve during the foaming process (Figure 1.3) (Gibson et al., 1982, Ashby et al., 2000; Kraynik et al., 2004; Gong and Kyriakides, 2006; Jang et al., 2008).

The work of this Thesis is focused on the theoretical study, development and application of periodic microstructured materials. These materials are studied by adopting crystal lattice models (Brillouin, 1946; Magid, 1964) or beam lattice models (Langley, 1994; Mead, 1996). For both models, the material can be studied by considering the unit cell, which is repeated periodically in different directions. The configuration of each periodic cell is described by a finite number of Lagrangian coordinates. In the crystal lattice model, the reciprocal interactions between pairs of point masses (atoms) are purely

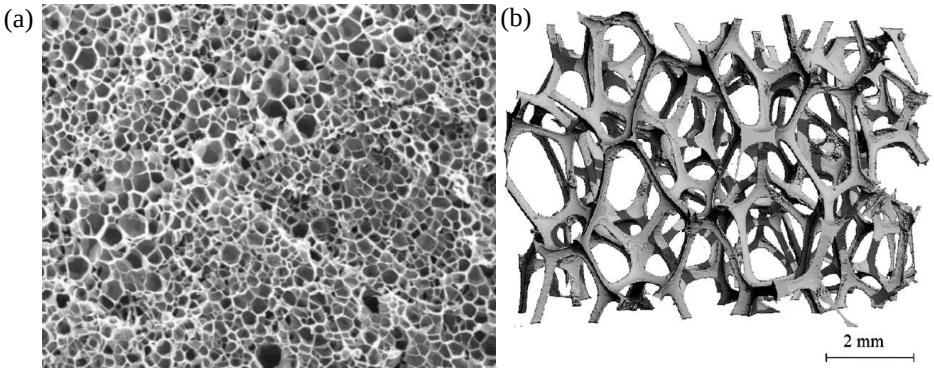

Figure 1.3 (a) Scanning electron micrograph of a first stage microcellular foam, (b) Computed tomography image of a polyester urethane foam (Jang et al., 2008).

attractive and repulsive. In the beam lattice model, instead, axial-bending elastic potentials are defined to describe the elastic coupling between close pairs of orientable massive points (nodes). The periodic material can be also modeled by high-fidelity first-order heterogeneous continuum (Dobrzynski et al., 1984; Dowling, 1992; Kushwaha et al., 1993; Phani et al., 2006; Spadoni et al., 2009; Liu et al., 2011; Zhu et al. 2016) or equivalent local and non-local homogeneous continua obtained with different homogenization techniques (Smyshlyaev, 2009; Craster et al., 2010; Lombardo and Askes, 2012; Bacigalupo and Gambarotta, 2014a; Bacigalupo and De Bellis, 2015; Rosi and Auffray, 2016; Reda et al., 2016; Kamotski and Smyshlyaev, 2019; Piccardo et al., 2019). Non-local homogeneous continua can be distinguished in micromorphic (Mindlin, 1963) and multipolar continua (Green and Naghdi, 1964).

The periodicity in the constituent material phases, or in the internal geometry of the microstructured materials governs their static and dynamic response. In this regards, the microstructured periodic materials are attractive for the unusual properties that they can exhibit as ultralightness and ultrastiffness (Zheng et al., 2014; Berger et al., 2017), auxeticity (Malischewsky et al., 2012; Dirrenberger et al., 2013; Cabras and Brun, 2014; Ren et al., 2018, Auricchio et al., 2019), negative refraction index (Li and Chan, 2004; Brunet et al., 2015) and exotic performance as energy focusing or harvesting, controllable wave guiding, obstacle cloaking, acoustic filtering (Khelif et al., 2004; Bigoni et al., 2008, 2013; Craster and Guenneau, 2012; Chen et al., 2014; Colquitt et al., 2014; Misseroni et al., 2016; Bacigalupo and Lepidi, 2018; Vadalà et al., 2018).

The location of the ultralight materials on the stiffness versus density chart is shown in Figure 1.4. The stretch-dominated microlattices, characterized by ultralightness and ultrastiffness, populate the upper left of the chart (Gibson and Ashby, 1999) and have stiffness to weight ratios that do not degrade when density decreases by several orders of magnitude.

Materials with exotic properties are also the auxetic materials characterized by a negative Poisson's ratio. They elongate along directions perpendicular to the tensile loading direction (Figure 1.5). The term

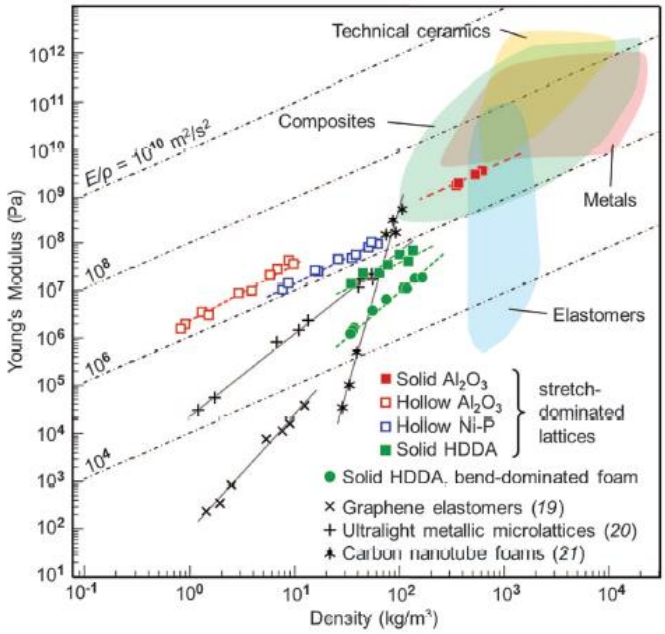

Figure 1.4 An Ashby chart plotting compressive stiffness versus density for ultralight, ultrastiff mechanical materials (Zheng et al., 2014).

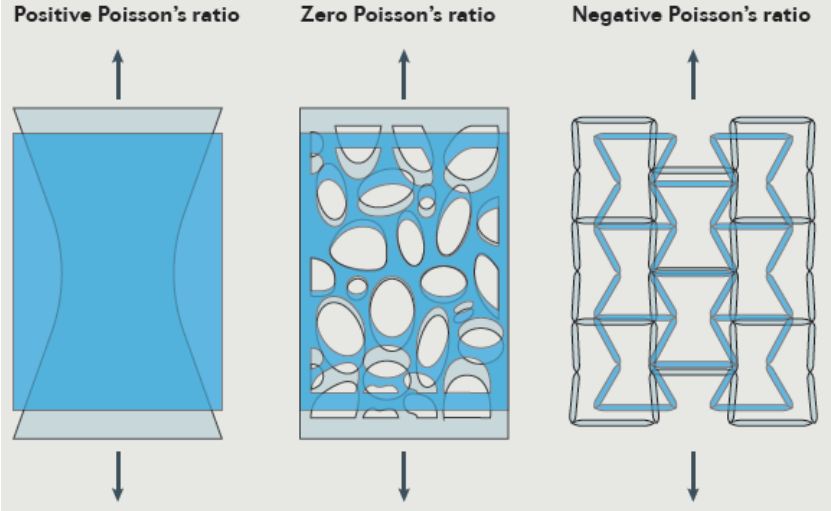

Figure 1.5 A rubber sheet, a random cellular material and an auxetic metamaterial are shown before (blue) and after (grey) the application of a longitudinal stretch (Bertoldi et al., 2017).

auxetic is firstly introduced in 1991 (Evans, 1991), but already a decade earlier a material with negative Poisson's ratio was fabricated in the form of 2D silicone rubber or aluminum honeycombs deforming by flexure of the ribs (Gibson et al., 1982). In the following years, various types of artificial fabricated auxetic materials are proposed and fabricated with advanced manufacturing techniques. Among these, there are the chiral and anti-chiral honeycomb materials where the auxetic behavior is activated by rolling-up deformation mechanisms. The superior properties of auxetic materials make them interesting also for potential applications as intelligent filters, sensors and protection devices.

In general, in the dynamical field, the microstructured materials can be distinguished in *phononic crystals* (Yang et al., 2004; Khelif et al., 2006; Lu et al., 2009) and *acoustic metamaterials* (Cummer et al., 2016; Ma and Sheng, 2016) (Figure 1.6). In the *phononic crystal* the internal microstructure interacts with the wave propagation depending on its size. Scattering from the internal microstructure can be observed when their sizes are comparable with the wavelength of the propagating wave. This phenomenon is usually called *Bragg scattering* (Brillouin, 1946) and it is associated to the possible presence of stop bands (band gaps) o pass bands in the dispersion spectrum that represents the relations between the wavevector and the frequency.

The *acoustic metamaterials* are characterized by the introducing of local resonant elements, mechanically coupled to the microstructure. The metamaterial exhibits a band gap at a wavelength below the regime corresponding to band gap generation based on spatial periodicity, which leads to *Bragg scattering*. The concept of metamaterials was introduced for the first time with the electromagnetic materials and then it is spreaded in thermal, mechanical and acoustic fields. The term metamaterial was coined by using the prefix meta, which can be translated from the Greek as beyond, to indicate artificials structures, typically periodic, that exhibit unusual properties that are not found in any known natural material. The first acoustic metamaterial is realized by 3D array of lead spheres coated with a layer of silicone rubber stacked in a cubic arrangement within an epoxy matrix (Figure 1.7) (Liu et al., 2000). Upon excitation with acoustic waves, the material exhibits negative elastic constants and a band gap at certain frequency ranges around the frequency associated to the local resonator. The possibility to open

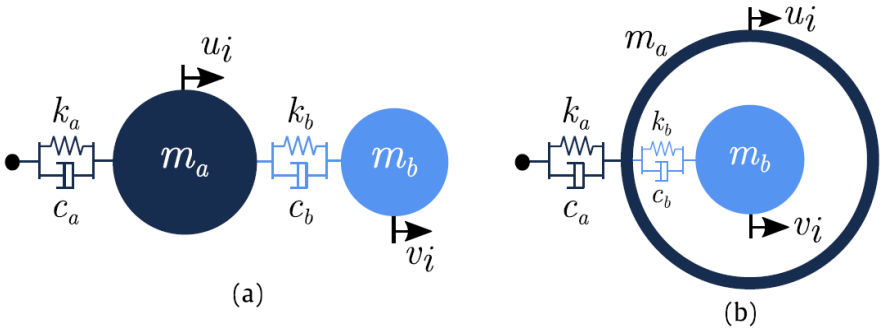

Figure 1.6 Discrete models of a monodimensional (a) phononic crystal (b) acoustic metamaterial (DePauw et al., 2018).

band gaps in the low-frequency range by using the local resonance gave a new major thrust in acoustic materials research. Among the new metamaterials studied there are materials with the very soft inclusion (Wang et al., 2004; Hsu and Wu, 2007), hollow cylinders or spheres (Sainidou et al., 2006), split hollow rings or spheres (Guenneau et al., 2007), beams or plates with suspended masses (Hong-Gang, 2006; Yu et al., 2006; Haslinger et al., 2017), plates or surfaces with pillars (Pennec, 2008; Wu, 2008; Oudich, 2010; Khelif, 2010).

The dispersion spectrum of the periodic material can be determined by solving the problem related to low-dimensional discrete models or to continuous models and by applying the Floquet-Bloch theory (Floquet, 1883; Bloch, 1929; Brillouin, 1946).

Analytical approximate solutions of the *direct* and *inverse* dispersion problem for low-dimensional discrete models can be determinated by using the asymptotic techniques (Pierre et al., 1996; Romeo and Luongo, 2002; Bacigalupo and Lepidi, 2016; Lepidi and Bacigalupo, 2018). The *direct* problem consists in determining the dispersion functions of the material, known the parameters that characterize the microstructure. In reverse, the *inverse* problem consists in determining which parameters realize an unknown periodic material characterized by a desired dispersion spectrum.

An approximation of the dispersion functions of the discrete model can be obtained through the formulation of an equivalent continuum model based on a continualization approach for discrete models (Reda et al., 2016, 2017; Bacigalupo and Gambarotta, 2016, 2017a, 2019; Bacigalupo et al., 2019a).

The microstructured materials with tuned parameters are attractive for several applications including the filtering of the wave propagation obtained designing the microstructural parameters of the material to open band gaps in the dispersion spectrum at target-center frequencies. Tuning the oscillator frequency with the desired center-frequency in the low-frequency range and achieving the largest possible bandwidth is a challenging multi-objective optimization issue (Wang et al., 2015, 2016; Bacigalupo et al., 2016, 2017, 2019b). The optimal solution must be sought for in a properly bounded multi-dimensional space of the mechanical parameters describing the periodic microstructure and the resonators.

Starting from this scientific background, the possible advanced applications of the periodic microstructured materials in aerospace, chemical, naval, biomedical engineering as wave guides, obstacle cloaks, low-frequency noise filters, energy harvesters motivated the study conducted in this Thesis. The research activity is focused on the metamaterials containing inertial viscoelastic resonators. The

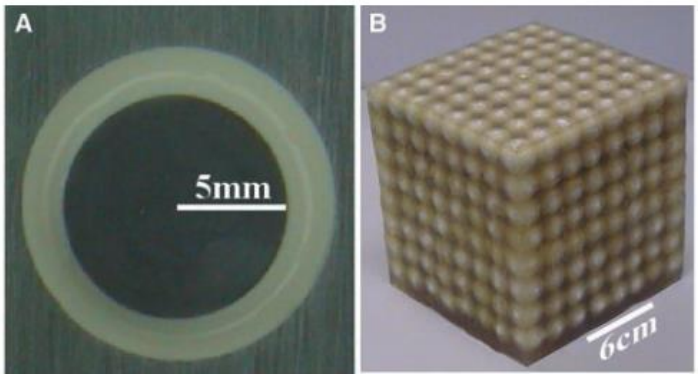

Figure 1.7 (A) Cross section of a coated lead sphere that forms the basic structure unit (B) sonic crystal (Liu et al., 2000).

development of this research field is motivated by some open investigation issues. First, a general improvement in the elastodynamic description of the linear and non-linear dissipation mechanisms occurring in infinite periodic phononic systems has been recognized as the theoretical key point for the future advances in the energetically consistent modelization and spectral design of acoustic metamaterials (Hussein et al., 2014). Second, a completely new class of mechanical meta-behaviours has been postulated to be developable in the next few years, by exploiting the virtuous contrast and synergy among constituent ingredient materials featured by strongly dissimilar elastic, plastic and viscous properties (Bertoldi et al., 2017).

The study of dissipation mechanisms is interesting to understand how the inevitable presence of damping in periodic materials influences their behavior. The first studies on damped periodic materials are focused on the analisys of a monocoupled periodic chain with a complex stiffness (Mead, 1973) and on damped laminates (Mukherjee and Lee, 1975), for which the dispersion relations for various levels of damping are obtained by using the finite difference method. The dispersion spectrum for a damped material is characterized by complex-valued wavevector or frequency with imaginary parts representing spatial or temporal wave attenuation, respectively (Lakes, 2009; Achenbach, 2012). The complex-valued dispersion spectrum is obtained with two different approaches. The first approach allows to evaluate frequencies of real-valued harmonic waves and complex-valued wavevectors (Mead, 1973; Romeo and Luongo, 2003; Luongo and Romeo, 2005; Merheb et al., 2008; Zhao and Wei, 2009; Gei, 2010; Moiseyenko and Laude, 2011; Farzbod and Leamy, 2011; Andreassen and Jensen, 2013; Krushynska et al., 2016; Morini and Gei, 2018). The second approach deals with the dispersion spectrum with complex-valued frequencies and real-valued wavevector (Mukherjee and Lee, 1975; Hussein, 2009; Phani and Hussein, 2013; Drugan, 2017). These works about the phononic crystal highlight that the viscoelasticity causes a shifting band gaps along the frequency axis and a variation of the band gap amplitude.

In the metamaterials, the studies are focused on the interaction between the resonance and the dissipative effects with the possibility of tuning the damping to achieve the band gap amplitude (Mead and Markuš, 1983; Smith et al., 1986; Thompson, 2008; Manimala and Sun, 2014). By comparing the acoustic metamaterials and the phononic crystals with the same material damping properties, the metamaterials exhibit higher levels of dissipation of the wave propagation. This phenomenon is called *metadamping* (Hussein and Frazier, 2013).

Based on this background in this field, the principal objectives of the research activity are:

- Evaluating the effects of variations in geometric and mechanical parameters of the non-dissipative beam lattice material on the dispersion spectrum to verify, for a suited parameter combination, the potential of the material as phononic filter in passively controlling the forced wave propagation.
- Studying the dispersion properties (frequencies and waveforms) of a metamaterial with viscoelastic resonators and analyzing the spectral effects of the viscoelastic constitutive parameters. The original aspect is the viscoelastic coupling derived by a physical-mathematical construct based on the Boltzmann superposition integral, whose kernel is approximated by a Prony series (Ferry, 1980; Lakes, 2009; Christensen, 2012). Consequently, the Bloch wave propagation is governed by a linear homogeneous system of integral-differential equations of motion. This integral description of the viscoelastic metamaterial dissipation enriches the classic formulations of viscous damping, sometimes following the rheological Rayleigh or Maxwell models.
- Evaluating the forced response of a metamaterial with viscoelastic resonators to harmonic single frequency external forces for the cases of non-resonant, resonant and quasi-resonant external forces (Mead, 1996; Movchan and Slepyan, 2014).

The Thesis is organized as follows. In chapter 2, the study of the dispersion properties of the microstructured materials is introduced. In particular, monodimensional crystal lattices, where the reciprocal interactions between the atoms are purely attractive and repulsive, are studied with focus on the effects that the presence of a viscoelastic device causes on the dispersive properties of the material.

In chapter 3, the dispersion spectra of 2D elastic beam lattice are determined by solving the dispersion problem related to low-dimensional discrete model and two alternative continuous models (high-fidelity first-order heterogeneous and equivalent homogenized micropolar continuum). Parametric analyses concerning the effects of variations in the enlarged space of geometric and mechanical parameters on the dispersion spectra are carried out. A satisfying tuning of the micromechanical properties is employed to verify the filtering functionality of the material in the forced wave propagation. At last, a parametric optimization for the search of full and partial band gaps with the largest amplitude and lower center frequency is carried out.

In chapter 4, a discrete linear model of the periodic beam lattice microstructure, visco-elastically coupled with local resonators, is formulated. Therefore, the dynamic problem concerning the wave propagation of damped waves is stated according to the Floquet-Bloch theory. First, the complex dispersion spectrum characterizing the free dynamics is determined and the effects of different approximations of the coupling relaxation functions are parametrically analysed, with reference to the exact dispersion curves. Second, the forced response to harmonic single frequency external sources is investigated in the frequency and time domain for the fundamental cases of non-resonant, resonant and quasi-resonant external forces.

Finally, in chapter 5 the conclusions are reported and possible developments are outlined.

CHAPTER 2

CRYSTAL LATTICE

A crystal or crystalline solid is a periodic material whose constituents are organized in a geometric lattice of material points or bodies that can be infinitely extended in all directions. By virtue of the periodicity, the mechanical behavior of a crystal lattice can be fully described by a suited physical-mathematical model of the elementary cell, which repeats itself in different directions.

Historically the first study of a crystal lattice that is extended in one direction, that is, one-dimensional lattice, is attributed to Newton's work done to derive a formula of the velocity of sound in a medium. The medium studied by Newton consists in a lattice of equal masses equispaced along the direction of sound propagation and attracted by the neighbor masses with an elastic force. Later, the same model was studied by Cauchy, who first obtained the wavelength-dependent velocity of propagation. At the end of the nineteenth century, Kelvin, studying a monodimensional lattice of equidistant point masses – previously treated by Baden-Powell – deduced that the frequency varies according to the wavenumber, defined as the inverse of the wavelength. The results just mentioned constitute the starting point for the development of the work conducted by Brillouin on the propagation of waves in crystal lattices (Brillouin, 1946).

In this chapter, the one-dimensional (or monodimensional) lattice materials are analyzed, by properly distinguishing between lattices with monoatomic cell and lattices with biatomic cell, including the mass-in-mass lattice where an auxiliary atom is introduced inside the other and plays the role of internal local resonator (Huang et al., 2009). Furthermore, the attention is focused on the effects that the presence of a viscoelastic coupling causes on the dispersive properties of the material.

2.1. Undamped monoatomic lattice material

The monodimensional monoatomic lattice material is characterized by an infinite chain of equidistant atoms that exchange linear elastic forces with the adjacent atoms. A discrete model (Figure 2.1) is formulated to describe the linear elastodynamic behavior of the monoatomic elementary cell where the atom is modeled as a point body with mass m and the linear interaction with the atoms of the adjacent cells is simulated by linear elastic spring with stiffness k_m. Furthermore, the lattice is ideally supposed to be perfectly non-dissipative. The configuration of the *i*-th mass is described by the time-dependent horizontal displacement $u_i(t)$. The free dynamics of the elementary cell is governed by an ordinary differential equation of motion

$$m\ddot{u}_i + 2k_m u_i - k_m u_{i-1} - k_m u_{i+1} = 0, \tag{2.1}$$

where the dots indicate the differentiation with respect to the time t.

Given the periodicity of the material, the displacements of two adjacent cells are related by the Floquet-Bloch conditions (Brillouin, 1946)

$$u_i = u_{i-1}e^{\imath ka}, \quad u_{i+1} = u_i e^{\imath ka}, \tag{2.2}$$

where a is the distance between the point masses and k is the wavenumber.

The propagation of harmonic waves is studied by applying the bilateral Laplace transform $\mathcal{L}[\bullet] = \int_{-\infty}^{\infty}(\bullet)e^{-st}dt$ to the equations (2.1)

$$ms^2\hat{u}_i + 2k_m\hat{u}_i - k_m\hat{u}_i e^{-\imath ka} - k_m\hat{u}_i e^{\imath ka} = 0, \tag{2.3}$$

where s is the Laplace variable and $\hat{u}_i$ is the bilateral Laplace transform of the displacement u_i that converges according to Paley and Wiener, 1934, and Van der Pol, 1955. By excluding the trivial solution ($\hat{u}_i = 0$) and dividing eq. (2.3) by m the equation is

$$s^2 + 2\omega_m^2 - \omega_m^2 e^{-\imath ka} - \omega_m^2 e^{\imath ka} = 0, \tag{2.4}$$

in which $\omega_m^2 = k_m / m$ is the square of the *circular frequency* of the harmonic oscillator of mass m and stiffness k_m.

Two different approaches can be followed in order to estimate the relations between the Laplace variable and the wavenumber (Hussein et al., 2014). The first technique, called *inverse method*, consists in imposing the real wavenumber and solving the equation in terms of the complex-valued variable s. A second technique, known as the *direct method*, leads to the dispersion relations by imposing the real variable s and solving for complex wavenumber. By using the *inverse method*, the solutions of eq. (2.4), expressed in exponential and trigonometric form, are

$$s^2 = \omega_m^2(-2 + e^{-\imath ka} + e^{\imath ka}) = \omega_m^2 2(\cos(ka) - 1), \tag{2.5}$$

that can be rewritten by introducing the non-dimensional variables $\tilde{s} = s / s_0$, where $s_0 = \omega_m$, and $\tilde{k} = ka$

$$\tilde{s} = \pm\sqrt{2(\cos(\tilde{k}) - 1)}. \tag{2.6}$$

The values of the variable $\tilde{s}$ obtained by the relations (2.6) are purely imaginary for each real value of the wavenumber $\tilde{k}$, except for $\tilde{k} = 0$ where $\tilde{s} = 0$. Furthermore, the dispersion curves are symmetric about $\tilde{k} = 0$ and periodic with period 2π (Figure 2.2). Consequently the characteristics of harmonic waves in terms of the relations between their wavenumber and the Laplace variable are described in the period $\tilde{k} \in [-\pi, \pi]$, called *First Brillouin zone*, defined by the reciprocal lattice that represents the Fourier transform of the lattice (Brillouin, 1946). Given the symmetry of the dispersion spectrum, the dispersion

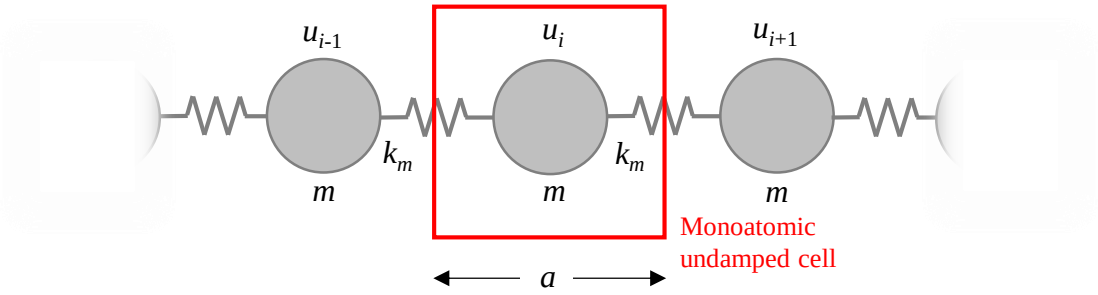

Figure 2.1 Undamped monoatomic lattice material.

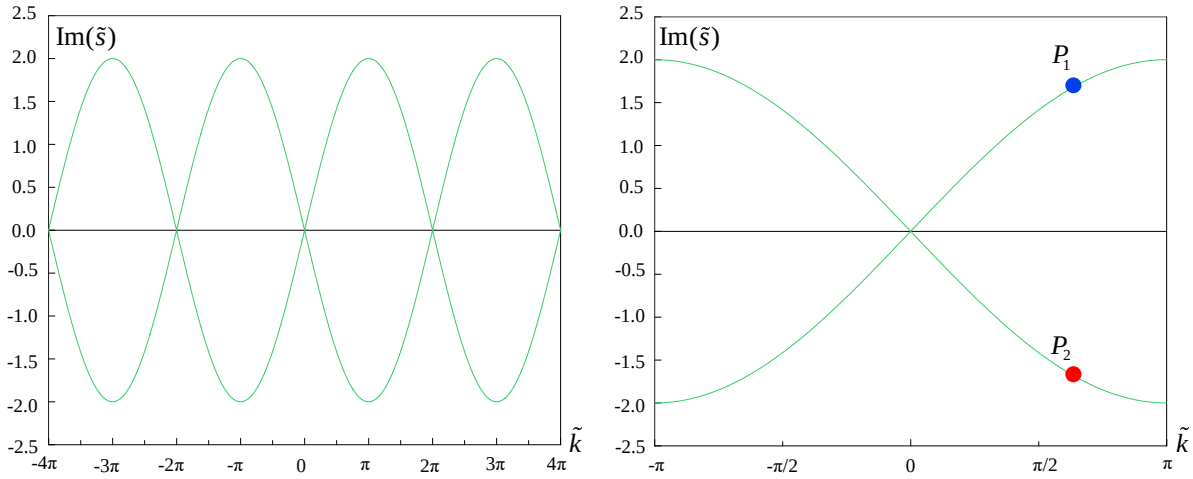

Figure 2.2 Dispersion curves of undamped monoatomic lattice material.

properties of the lattice can be fully described only considering $\tilde{k} \in [0, \pi]$, defined *Irreducible Brillouin zone*.

For each value of the wavenumber k the imaginary value of s is computed and the displacement of the *i*-th mass $u_i = \bar{u} e^{(\imath kx + st)}$, where $\bar{u}$ is the amplitude of the wave, is obtained. The displacement can be defined in non-dimensional form $\tilde{u}_i = u_i / l_0$ where l_0 is a characteristic length. Chosen the value of the wavenumber $\tilde{k}$ equal to 2, from which it is obtained through the relations (2.6) $\tilde{s} = 1.68294\imath$ and $\tilde{s} = -1.68294\imath$ (points P_1 and P_2 in Figure 2.2), the displacement $\tilde{u}_i$ is achieved (Figure 2.3). The wave characterized by a positive value of Im($\tilde{s}$) (points P_1) is a *forward* propagating wave while the wave characterized by a negative value of Im($\tilde{s}$) (points P_2) is a *backward* propagating wave (Figure 2.3). In this regard, defined the complex velocity as $\tilde{v}_c = \tilde{s} / \tilde{k}$ (Carcione, 2007), it can be evaluated the speed at which the phase of the wave propagates in space, called phase velocity, through the relation (Figure 2.4a)

$$\tilde{v}_{ph} = \mathrm{Im}(\tilde{v}_c) = \frac{\mathrm{Im}(\tilde{s})}{\tilde{k}}. \tag{2.7}$$

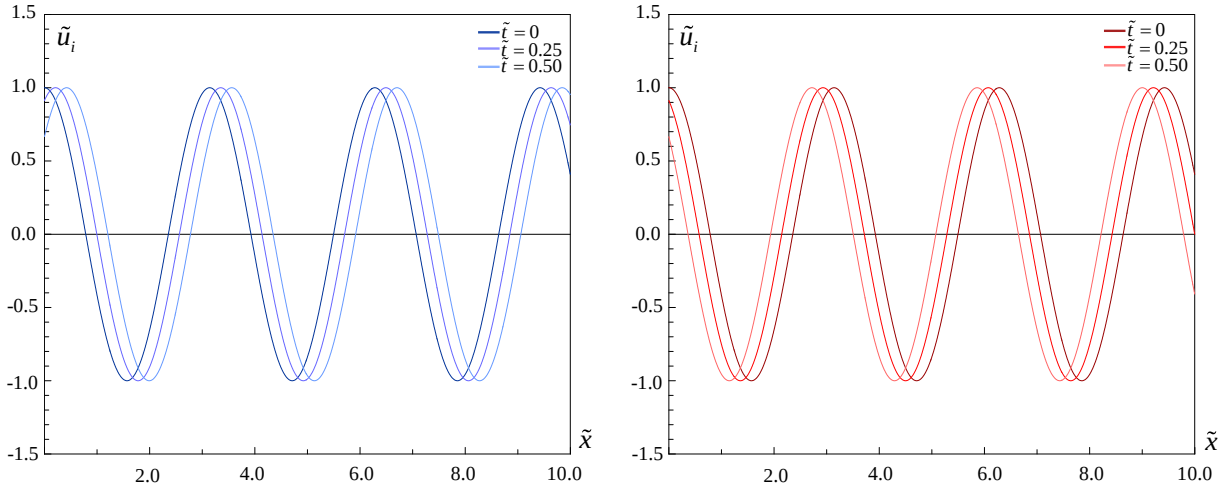

Figure 2.3 Displacement of the *i*-th mass of the undamped monoatomic lattice material ($\tilde{k} = 2$).

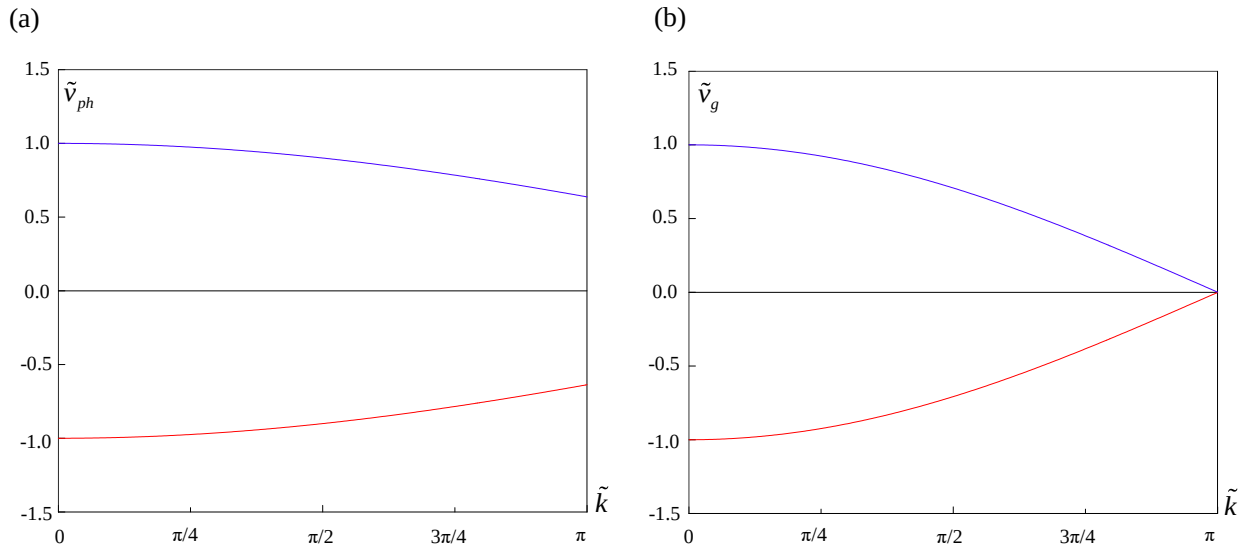

Figure 2.4 (a) Phase velocity, (b) Group velocity in the undamped monoatomic lattice material.

By evaluating the values of the phase velocity corresponding to the wavenumber and variable $\tilde{s}$ associated to the points P_1 and P_2 of the diagram, it is obtained $\tilde{v}_{ph} = 0.841471$ for the point P_1 and $\tilde{v}_{ph} = -0.841471$ for the point P_2.

The relation (2.6) between the wavenumber and the variable $\tilde{s}$ is not linear and consequently the phase velocity does not coincide with the group velocity, which is the velocity with which the overall shape of the waves' amplitudes propagates through space, defined as

$$\tilde{v}_g = \frac{d\tilde{s}}{d\tilde{k}}. \tag{2.8}$$

Deriving with respect to $\tilde{k}$ the relation (2.6), the group velocity is $\tilde{v}_g = \mp \sin(\tilde{k}) / \sqrt{-2 + 2\cos(\tilde{k})}$. Given the symmetry about $\tilde{k} = 0$ of the dispersion diagram, the phase and group velocity are evaluated in the interval $\tilde{k} \in [0, \pi]$ (Figure 2.4). The values of the phase velocity and the group velocity are equal for $\tilde{k} = 0$, but they are different for the other values of $\tilde{k}$. In particular, for $\tilde{k} = \pi$ the group velocity is equal to zero while the phase velocity is $\tilde{v}_{ph} = \pm 0.63662$ (Figure 2.4).

2.2. Damped monoatomic lattice material

The model of the monodimensional lattice material can be enriched by removing the hypotheses of non-dissipative lattice. The linear interaction between the atoms of the adjacent cells and the dissipation are simulated by a viscoelastic device characterized by a stiffness k_m and a translational relaxation function $k_d(t)$ (Figure 2.5). The free damped vibrations of the discrete model are governed by integral-differential equation of motion

$$m\ddot{u}_i + 2k_m u_i - k_m u_{i-1} - k_m u_{i+1} + \int_{-\infty}^{t} k_d(t-\tau)\frac{d}{d\tau}(u_i - u_{i-1})d\tau + \int_{-\infty}^{t} k_d(t-\tau)\frac{d}{d\tau}(u_i - u_{i+1})d\tau = 0, \tag{2.9}$$

where dots indicate differentiation with respect to time t.

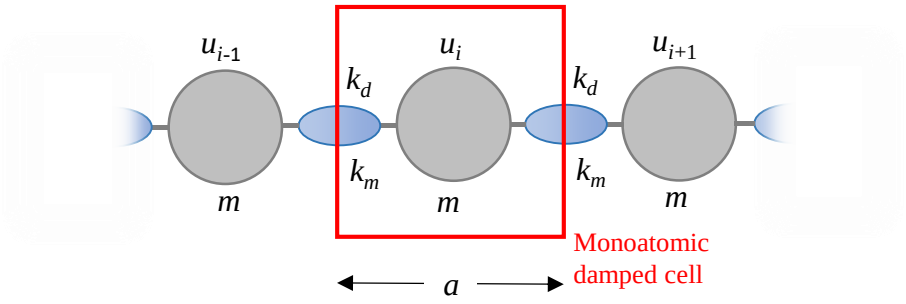

Figure 2.5 Damped monoatomic lattice material.

The integral formulation of the viscoelasticity is based on the idea of Boltzmann to assume that the material has memory of the events that have affected it and that, therefore, the mechanical response is a function of the previous history. This theory was revived at the beginning of the twentieth century by Volterra and deepened by Benvenuti (Volterra, 1913).

The translational relaxation function $k_d(t)$ can be modeled by using the Prony series. To simplify the model, only the first exponential term of the series (Maxwell model) is considered

$$k_d(t) = e^{-\frac{t}{t_r}} k_{d1}\,\mathrm{U}(t), \tag{2.10}$$

where t_r is the relaxation time, k_{d1} is the relaxation function at $t=0$ and $\mathrm{U}(t)$ is the unit step function. It is worth noting that the function (2.10) is a causal function. The relaxation function expressed by the relation (2.10) has a decreasing trend over time (Figure 2.6).

By applying the Floquet-Bloch conditions (2.2) and the bilateral Laplace transform to equation (2.9), by remembering the causality of the function (2.10) (Paley and Wiener, 1934; Van der Pol, 1955)

$$ms^2\hat{u}_i + 2k_m\hat{u}_i - k_m\hat{u}_i e^{-\imath ka} - k_m\hat{u}_i e^{\imath ka} + \frac{k_{d1}t_r}{1+st_r}(\hat{u}_i - \hat{u}_i e^{-\imath ka}) + \frac{k_{d1}t_r}{1+st_r}(\hat{u}_i - \hat{u}_i e^{\imath ka}) = 0, \tag{2.11}$$

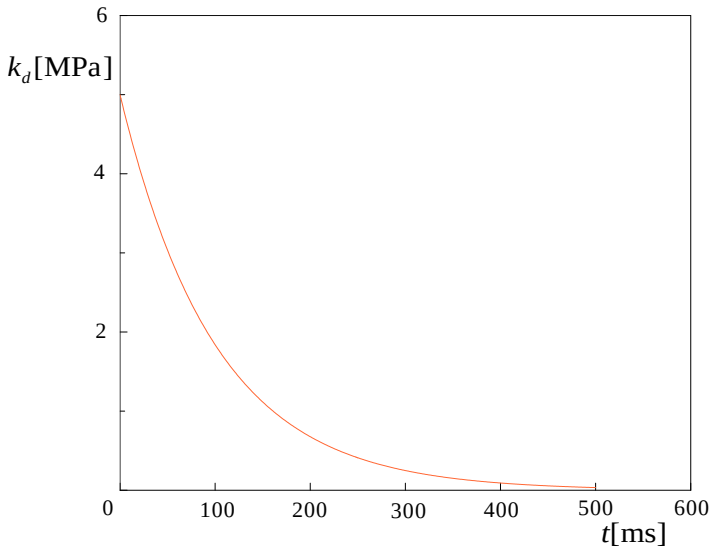

Figure 2.6 Relaxation function ($k_{d1} = 5\mathrm{MPa}$, $t_r = 100\mathrm{ms}$).

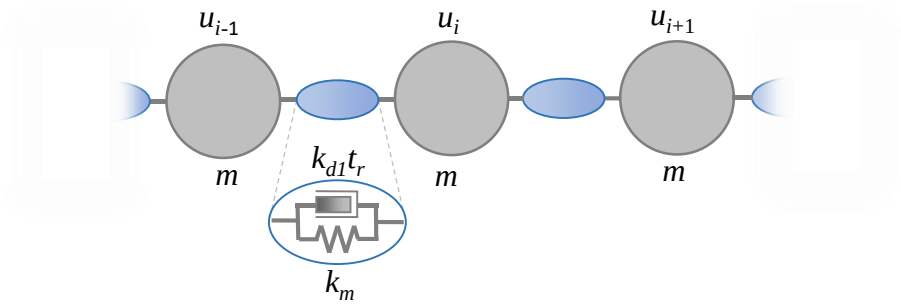

Figure 2.7 Damped monoatomic lattice material with springs and dashpots.

where the bilateral Laplace transform $\mathcal{L}[k_d] = \int_{-\infty}^{\infty} k_d e^{-st} dt = k_{d1} t_r / (1 + s t_r)$ can be approximated with its first order Taylor polynomials centered at $s = 0$

$$k_d = k_{d1} t_r s + O(s^2), \tag{2.12}$$

It is worth noting that, considering the first order Taylor polynomial, the viscoelastic terms are linear in the Laplace variable, recovering the classical viscous damping originated by velocity-proportional dissipation. This behavior is modeled with a spring connected in parallel to a dashpot as in the Figure 2.7. By replacing the (2.12) in the (2.11) the equation becames

$$m s^2 \hat{u}_i + 2k_m \hat{u}_i - k_m \hat{u}_i e^{-\imath ka} - k_m \hat{u}_i e^{\imath ka} + k_{d1} t_r s(\hat{u}_i - \hat{u}_i e^{-\imath ka}) + k_{d1} t_r s(\hat{u}_i - \hat{u}_i e^{\imath ka}) = 0. \tag{2.13}$$

Excluding the trivial solution ($\hat{u}_i = 0$) and dividing the equation (2.13) by m

$$s^2 + 2\omega_m^2 - \omega_m^2 e^{-\imath ka} - \omega_m^2 e^{\imath ka} + \xi_d s(1 - e^{-\imath ka}) + \xi_d s(1 - e^{\imath ka}) = 0, \tag{2.14}$$

where $\xi_d = k_{d1} t_r / m$ in the following sections is called the *damping parameter*.

By introducing the non-dimensional variable $\tilde{s} = s / s_0$ and damping parameter $\tilde{\xi}_d = \xi_d / s_0$, where s_0 is a real-valued circular frequency that can be arranged equal to ω_m, and the non-dimensional wavenumber

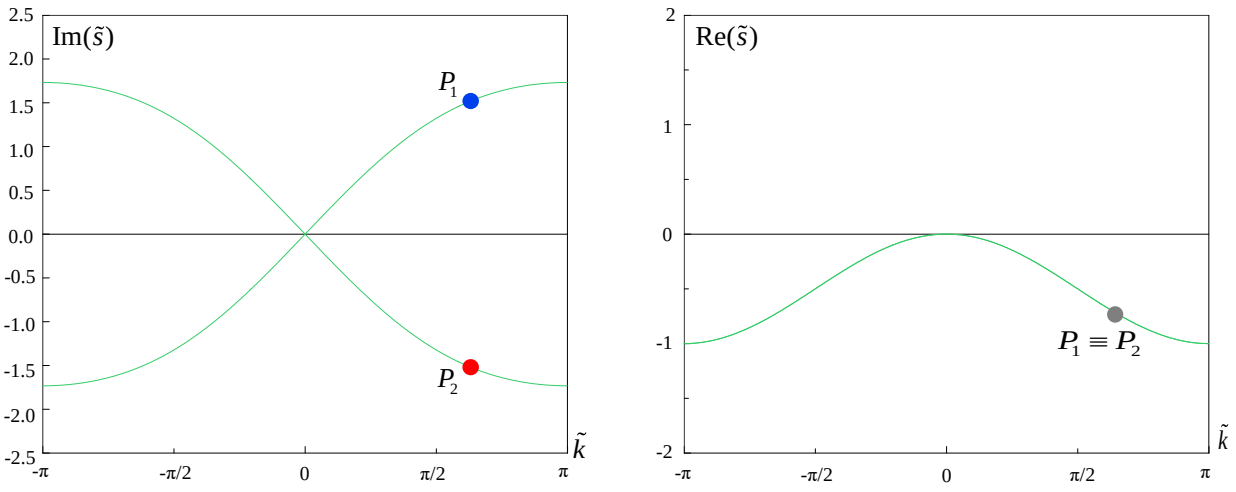

Figure 2.8 Dispersion curves of damped monoatomic lattice material ($\tilde{\xi}_d = 0.5$).

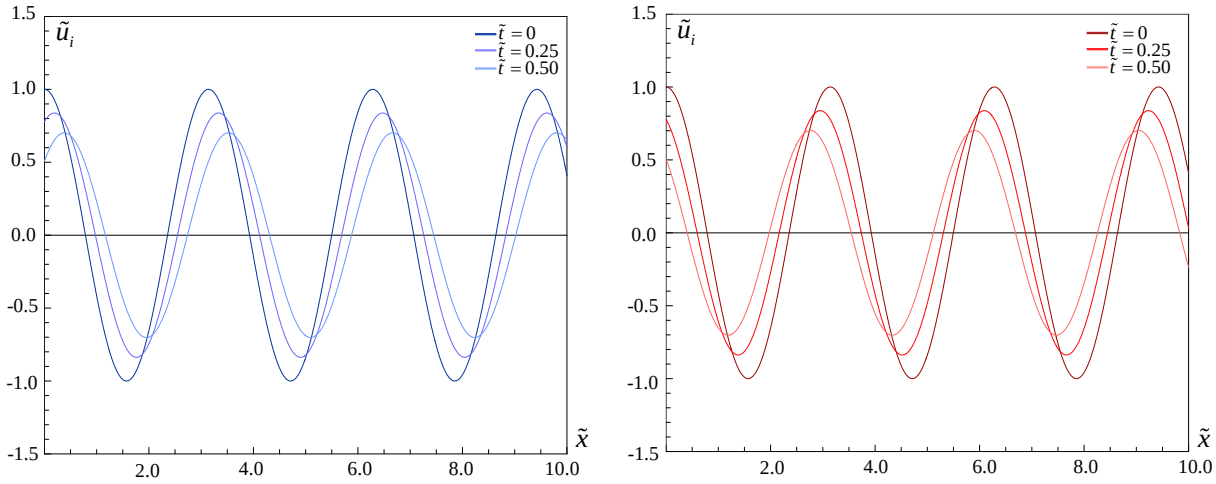

Figure 2.9 Displacement of the *i*-th mass of the damped monoatomic lattice material ($\tilde{k} = 2$).

$\tilde{k} = ka$, the complex-valued dispersion relations in exponential and trigonometric form are obtained (Figure 2.8)

$$\begin{aligned}\tilde{s} &= \frac{1}{2}\left[-\tilde{\xi}_d(2-e^{-\imath\tilde{k}}-e^{\imath\tilde{k}}) \pm \sqrt{\tilde{\xi}_d^2(2-e^{-\imath\tilde{k}}-e^{\imath\tilde{k}})^2 - 4(2-e^{-\imath\tilde{k}}-e^{\imath\tilde{k}})}\right] = \\ &= -\tilde{\xi}_d + \tilde{\xi}_d\cos(\tilde{k}) \pm \frac{1}{2}\sqrt{-8+2\tilde{\xi}_d+8\cos(\tilde{k})-2\tilde{\xi}_d{}^2\cos(\tilde{k})},\end{aligned} \tag{2.15}$$

where the imaginary part of the variable $\tilde{s}$ is the *wave frequency* and the ratio $z_d = -\mathrm{Re}(\tilde{s})/\mathrm{Abs}(\tilde{s})$ is the *damping ratio* (Hussein et al., 2014), where $\mathrm{Re}(\tilde{s})$ is a negative value.

Chosen the wavenumber $\tilde{k}$ equal to 2, from which $\tilde{s} = -0.708073 + 1.52674\imath$ and $\tilde{s} = -0.708073 - 1.52674\imath$ (points P_1 and P_2 in Figure 2.8) are obtained through the dispersion relations (2.15), the displacement $\tilde{u}_i$ is computed (Figure 2.9). With respect to the undamped lattice, an attenuation of the displacement is observed. This dissipation of the wave can be related to the *damping ratio* that is zero in the undamped lattice.

By evaluating, through the relation (2.7), the phase velocity corresponding to the values of wavenumber and variable $\tilde{s}$ associated to the points P_1 and P_2 of the diagram, it is obtained $\tilde{v}_{ph} = 0.763368$ for the point P_1 (*forward* propagating wave) and $\tilde{v}_{ph} = -0.763368$ for the point P_2 (*backward* propagating wave). The dispersion relations (2.15) are not linear functions of $\tilde{s}$ and consequently the phase velocity does not coincide with the group velocity defined as

$$\tilde{v}_g = \frac{\partial\tilde{s}}{\partial\tilde{k}}, \tag{2.16}$$

that applied to equations (2.15) gives $\tilde{v}_g = -\tilde{\xi}_d\sin(\tilde{k}) \pm \dfrac{-4\sin(\tilde{k}) + \tilde{\xi}_d{}^2\sin(\tilde{k})}{2\sqrt{-8+2\tilde{\xi}_d+8\cos(\tilde{k})-2\tilde{\xi}_d{}^2\cos(\tilde{k})}}$.

Given the symmetry about $\tilde{k} = 0$ of the dispersion diagram, the phase and group velocities are evaluated in the interval $\tilde{k} \in [0, \pi]$ (Figure 2.10). Except $\tilde{k} = 0$, the values of the phase velocity and the group

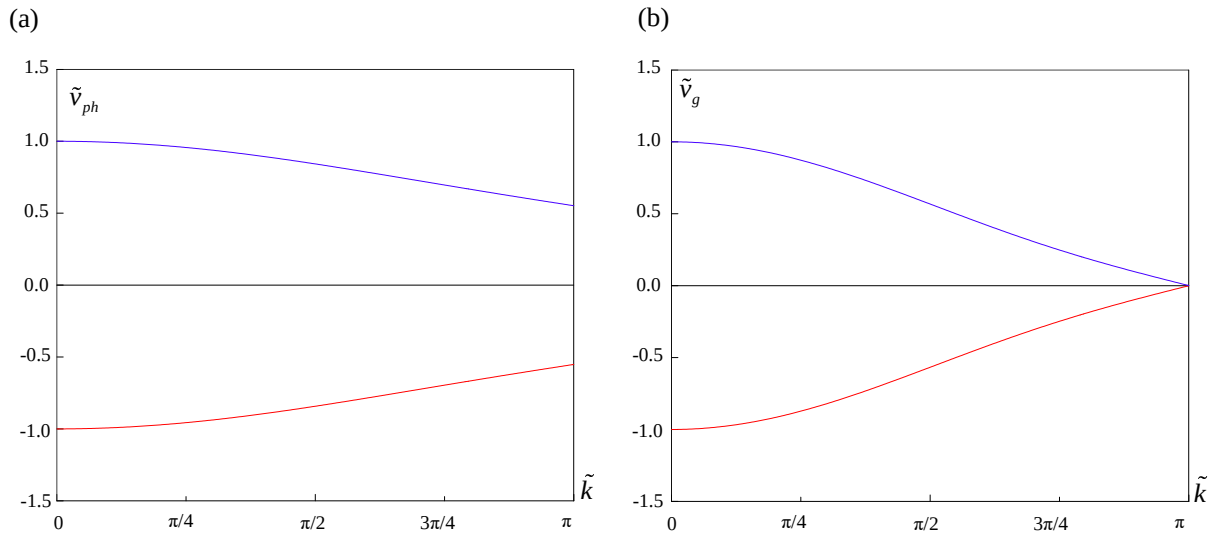

Figure 2.10 (a) Phase velocity, (b) Group velocity in the damped monoatomic lattice material.

velocity are different and, in particular, for $\tilde{k}=\pi$ the group velocity is equal to zero while the phase velocity is $\tilde{v}_{ph}=\pm 0.551329$ (Figure 2.10). The variations of the real and imaginary parts of $\tilde{s}$ are related to the non-dimensional parameters $\tilde{\omega}_m^2=\omega_m^2/s_0^2$ and $\tilde{\xi}_d=\xi_d/s_0$, where s_0 is a circular frequency that can be arranged equal to a fraction of the *circular frequency* ω_m. Fixing the values of $\tilde{\omega}_m^2$ and the wavenumber $\tilde{k}$ (Figure 2.11), by increasing the value of $\tilde{\xi}_d$, the *wave frequency* decreases. By imposing $\mathrm{Im}(\tilde{s})=0$, the relation is obtained $\tilde{\xi}_d^*=\sqrt{2\tilde{\omega}_m^2}\Big/\sqrt{1-\cos(\tilde{k})}$ between the *damping parameter* with the wavenumber and the *circular frequency* and which allows to achieve the value $\tilde{\xi}_d^*$ for which $\tilde{s}$ is real. For $\tilde{\xi}_d<\tilde{\xi}_d^*$ the system is *under damped* and $\tilde{s}$ is a complex-valued. For $\tilde{\xi}_d=\tilde{\xi}_d^*$ the system is *critically damped* and $\tilde{s}$ is real-valued. Also for $\tilde{\xi}_d>\tilde{\xi}_d^*$ the variable $\tilde{s}$ is real and the system is *overdamped*. This behavior can be observed in the dispersion diagram for fixed values of the *circular frequency* and the *damping parameter* (Figure 2.12).

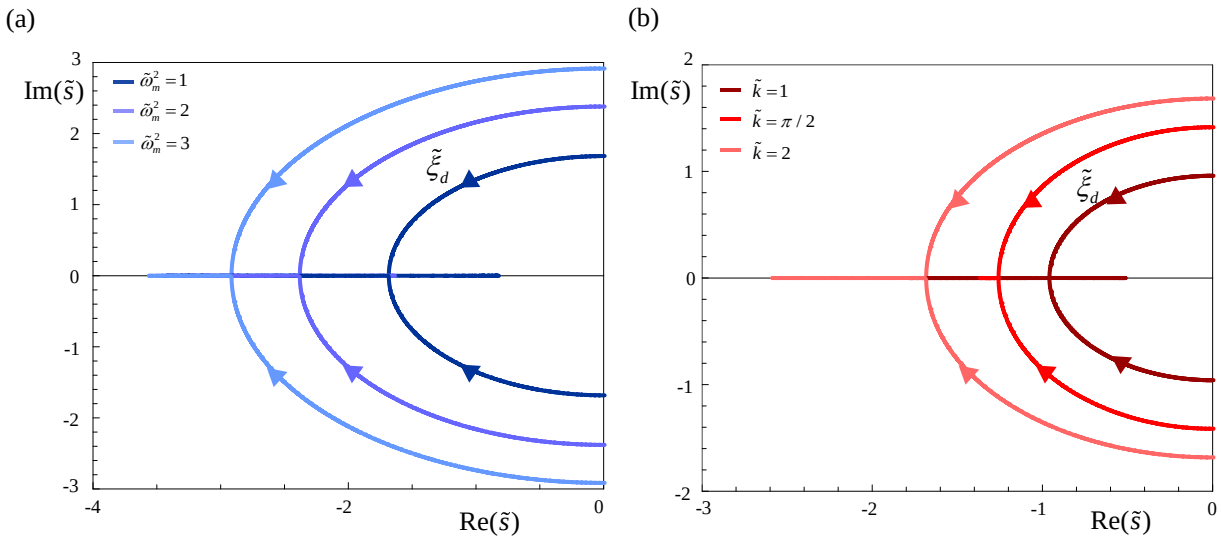

Figure 2.11 Imaginary and real part of the variable $\tilde{s}$ a) $\tilde{k}=2$ b) $\tilde{\omega}_m^2=1$.

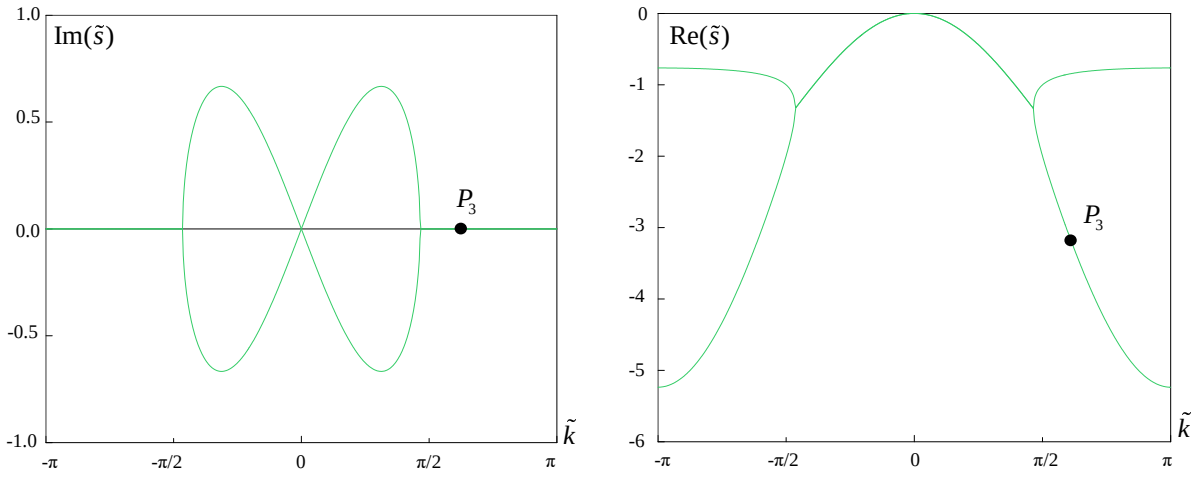

Figure 2.12 Dispersion curves of damped monoatomic lattice material ($\tilde{\omega}_m^2 = 1$, $\tilde{\xi}_d = 1.5$).

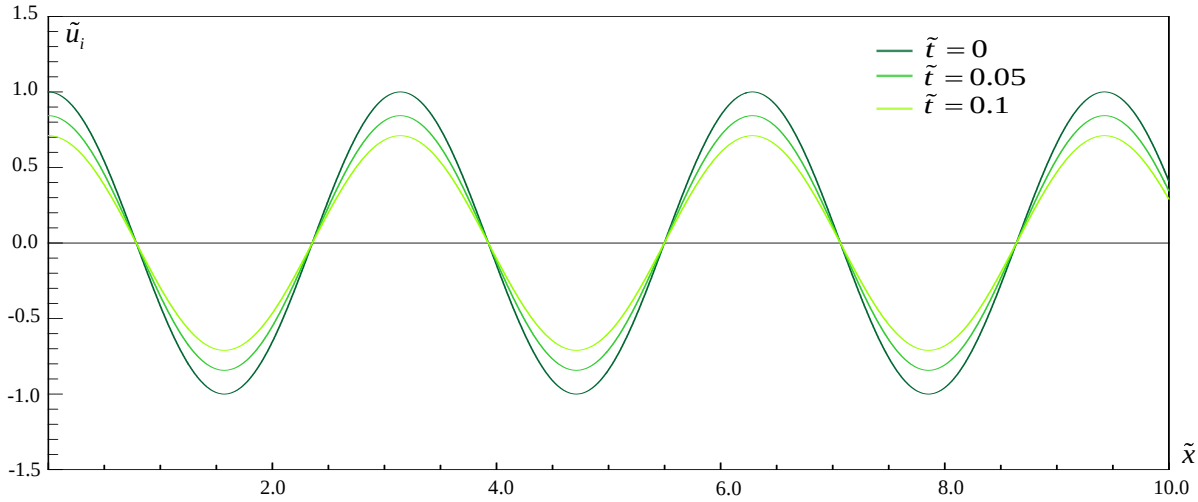

Figure 2.13 Displacement of the i-th mass of the damped monoatomic lattice material ($\tilde{\omega}_m^2 = 1$, $\tilde{\xi}_d = 1.5$, $\tilde{k} = 2$).

Chosen the $\tilde{k}$ -value equal to 2 in which $\mathrm{Im}(\tilde{s}) = 0$ (point P_3 in Figure 2.11), the phase velocity is equal to zero. In this case, the wave is stationary because its amplitude does not move in space, but it is damped in time (Figure 2.13).

2.3. Undamped biatomic lattice material

The monodimensional biatomic lattice material is characterized by an infinite chain of equidistant atoms that exchange linear elastic forces with the adjacent atoms having different mass. The linear elastodynamic behavior of the biatomic elementary cell is described by a discrete model where two atoms are modeled as a point bodies with masses m_1 and m_2 and the linear interaction with the atoms of the adjacent cells is simulated by linear elastic spring with stiffness k_m (Figure 2.14). Furthermore, the

lattice is ideally supposed to be perfectly non-dissipative. The configuration of the elementary cell is described by the time-dependent horizontal displacements $u_i(t)$ and $u_{i+1}(t)$ of the point bodies with masses m_1 and m_2, respectively. The free undamped dynamics of the elementary cell is governed by ordinary differential equations of motion

$$\begin{cases} m_1\ddot{u}_i + 2k_m u_i - k_m u_{i-1} - k_m u_{i+1} = 0 \\ m_2\ddot{u}_{i+1} + 2k_m u_{i+1} - k_m u_i - k_m u_{i+2} = 0. \end{cases} \tag{2.15}$$

Given the periodicity of the system, the displacements of the masses of *i*-th cell are related with the displacements of the adjacent cell with the Floquet-Bloch conditions

$$u_{i+2} = u_i e^{\imath ka}, \quad u_{i+1} = u_{i-1} e^{\imath ka}, \tag{2.16}$$

To study the propagation of harmonic waves in monodimensional lattice material, the bilateral Laplace transform and the Floquet-Bloch conditions (2.16) are applied to the equations (2.15)

$$\begin{cases} (m_1 s^2 + 2k_m)\hat{u}_i - k_m(1 + e^{-\imath ka})\hat{u}_{i+1} = 0 \\ (m_2 s^2 + 2k_m)\hat{u}_{i+1} - k_m(1 + e^{\imath ka})\hat{u}_i = 0. \end{cases} \tag{2.17}$$

Dividing the first and the second equation (2.17) by m_1 and m_2, respectively, the equations (2.17) is rewritten in the matrix form as

$$\begin{bmatrix} s^2 + 2\omega_{m1}^2 & -\omega_{m1}^2(1 + e^{-\imath ka}) \\ -\omega_{m2}^2(1 + e^{\imath ka}) & s^2 + 2\omega_{m2}^2 \end{bmatrix} \begin{pmatrix} \hat{u}_i \\ \hat{u}_{i+1} \end{pmatrix} = \begin{pmatrix} 0 \\ 0 \end{pmatrix}, \tag{2.18}$$

where $\omega_{m1}^2 = k_m / m_1, \omega_{m2}^2 = k_m / m_2$ are the square of the *circular frequencies* of the harmonic oscillators with mass m_1 and m_2, respectively, and stiffness k_m.

By introducing the non-dimensional parameter $\tilde{\gamma} = \omega_{m2} / \omega_{m1} = \sqrt{m_1 / m_2}$, the wavenumber $\tilde{k} = ka$ and the variable $\tilde{s} = s / s_0$, where s_0 is a real-valued circular frequency that can be arranged equal to ω_{m1}, the dispersion relations are found by solving the eigenvalues problem associated to (2.18). By equating to zero the characteristic polynomial, the equation to be solved is

$$\tilde{s}^4 + 2\tilde{s}^2 + 2\tilde{s}^2\tilde{\gamma}^2 + 2\tilde{\gamma}^2 - e^{-\imath\tilde{k}}\tilde{\gamma}^2 - e^{\imath\tilde{k}}\tilde{\gamma}^2 = 0. \tag{2.19}$$

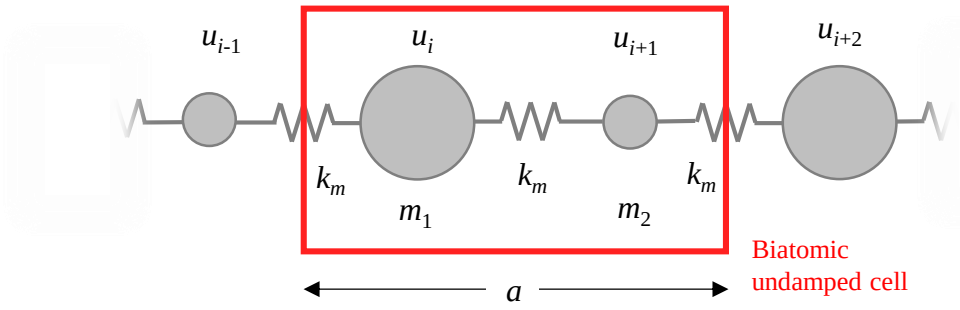

Figure 2.14 Undamped biatomic lattice material.

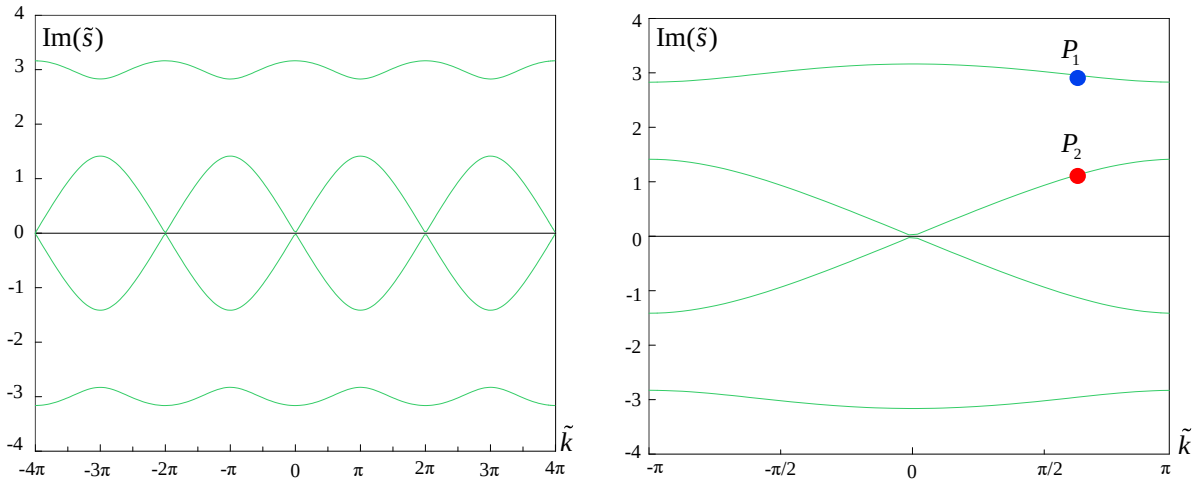

Figure 2.15 Dispersion curves of undamped biatomic lattice material ($\tilde{\gamma} = 2$).

The relations between the variable $\tilde{s}$ and the wavenumber $\tilde{k}$ in trigonometric form are (Figure 2.15)

$$\begin{aligned} \tilde{s}_{1,2} &= \pm\sqrt{-1-\tilde{\gamma}^2-(\cos\tilde{k}-\imath\sin\tilde{k})b} \\ \tilde{s}_{3,4} &= \pm\sqrt{-1-\tilde{\gamma}^2+(\cos\tilde{k}-\imath\sin\tilde{k})b}, \end{aligned} \tag{2.20}$$

where $b = \sqrt{(1+\tilde{\gamma}^4+2\tilde{\gamma}^2\cos\tilde{k})(\cos\tilde{k}+\imath\sin\tilde{k})^2}$.

In the dispersion spectrum (Figure 2.15) for $\mathrm{Im}(\tilde{s}) \in [1.414, 2.828]$ there are no corresponding real-valued wavenumber and the harmonic waves do not propagate. The range of $\mathrm{Im}(\tilde{s})$ where this phenomenon occurs is called *stop band*, or *band gap* (red band in the Figure 2.16). For the other values of the *wave frequency* in which there is corrisponding real-valued wavenumber the harmonic waves

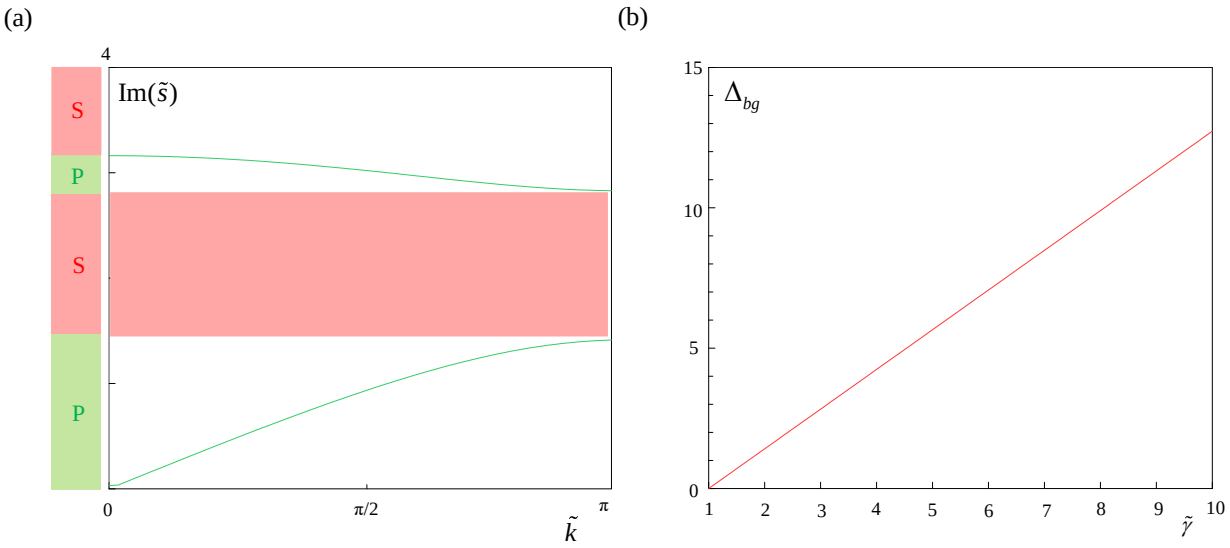

Figure 2.16 (a) Band gap in the dispersion diagram of undamped biatomic lattice material ($\tilde{\gamma} = 2$), (b) Band gap amplitude.

propagate and the ranges of $\mathrm{Im}(\tilde{s})$ are called *pass band* (green band in the Figure 2.16). The band gap amplitude $\Delta_{bg} = \min_{0\le\tilde{k}\le\pi} \tilde{s}_3 - \max_{0\le\tilde{k}\le\pi} \tilde{s}_1$ is conditioned by the parameter $\tilde{\gamma}$ (Figure 2.16). When $\tilde{\gamma} = 1$ the masses m_1 and m_2 are equal and the amplitude is zero. By increasing $\tilde{\gamma}$ the band gap amplitude increases linearly. Fixing the value of the wavenumber $\tilde{k}$ equal to 2, to which the values $\tilde{s} = 2.94914\imath$ and $\tilde{s} = 1.14131\imath$ (points P_1 and P_2 in Figure 2.15) with $\mathrm{Im}(\tilde{s}) > 0$ correspond, the displacement $\tilde{u}_i$ of *i*-th mass is computed (Figure 2.17). The *forward* propagating waves are characterized by two different speeds of propagation (Figure 2.18). In this regard, the phase velocity, defined by the relation (2.7), associated to the higher-frequency dispersion curve tends to infinity for $\tilde{k} \to 0$ and decreases by increasing the wavenumber (Figure 2.18). Different is the trend of the phase velocity associated to the lower-frequency dispersion curve that is $\tilde{v}_{ph} = 0.632454$ for $\tilde{k} = 0$ and slowly decreases by increasing the wavenumber (Hussein, 2009). By evaluating the phase velocity associated to the points P_1 and P_2, the values are $\tilde{v}_{ph} = 1.47457$ and $\tilde{v}_{ph} = 0.570656$, respectively, and this confirms the different speed of propagation of the waves.

The group velocity can be obtained deriving the relations (2.20) with respect to $\tilde{k}$

$$\begin{aligned} \tilde{v}_{g1,2} &= \pm(\tilde{\gamma}^2 \sin\tilde{k}(\cos\tilde{k} + \imath\sin\tilde{k})) / \sqrt{2b(-1-\tilde{\gamma}^2 - (\cos\tilde{k} - \imath\sin\tilde{k})b} \\ \tilde{v}_{g3,4} &= \pm(\tilde{\gamma}^2 \sin\tilde{k}(\cos\tilde{k} + \imath\sin\tilde{k})) / \sqrt{2b(-1-\tilde{\gamma}^2 + (\cos\tilde{k} - \imath\sin\tilde{k})b}, \end{aligned} \tag{2.21}$$

where $b = \sqrt{(1+\tilde{\gamma}^4 + 2\tilde{\gamma}^2\cos\tilde{k})(\cos\tilde{k} + \imath\sin\tilde{k})^2}$.

Given the symmetry about $\tilde{k} = 0$ of the dispersion diagram the group velocity, like the phase velocity, are evaluated in the Irreducible Brillouin zone and for positive *wave frequency* (Figure 2.18). The group velocity associated to the lower-frequency dispersion curve for $\tilde{k} = 0$ is $\mathrm{Im}(\tilde{v}_g) = 0.632451$ and decreases by increasing the wavenumber assuming $\tilde{v}_g = 0$ at $\tilde{k} = \pi$. Different is the trend of the group velocity $\tilde{v}_g$ associated to the higher-frequency dispersion curve that is equal to zero for $\tilde{k} = 0$ and $\tilde{k} = \pi$ and assumes a maximum value in the interval $\tilde{k} \in [\pi/2, 3\pi/4]$.

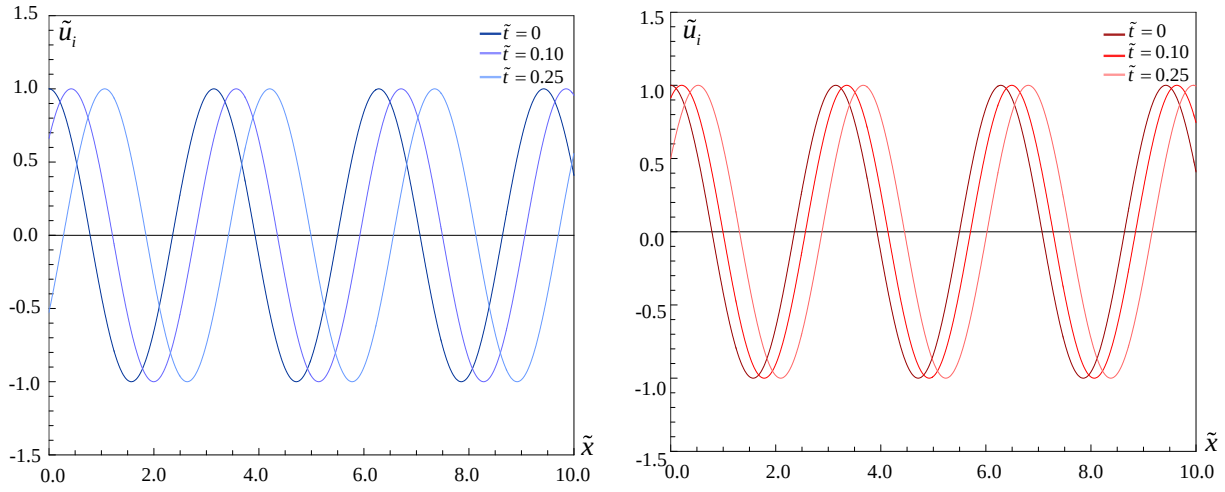

Figure 2.17 Displacement of the i-th mass of the undamped biatomic lattice material ($\tilde{k} = 2$).

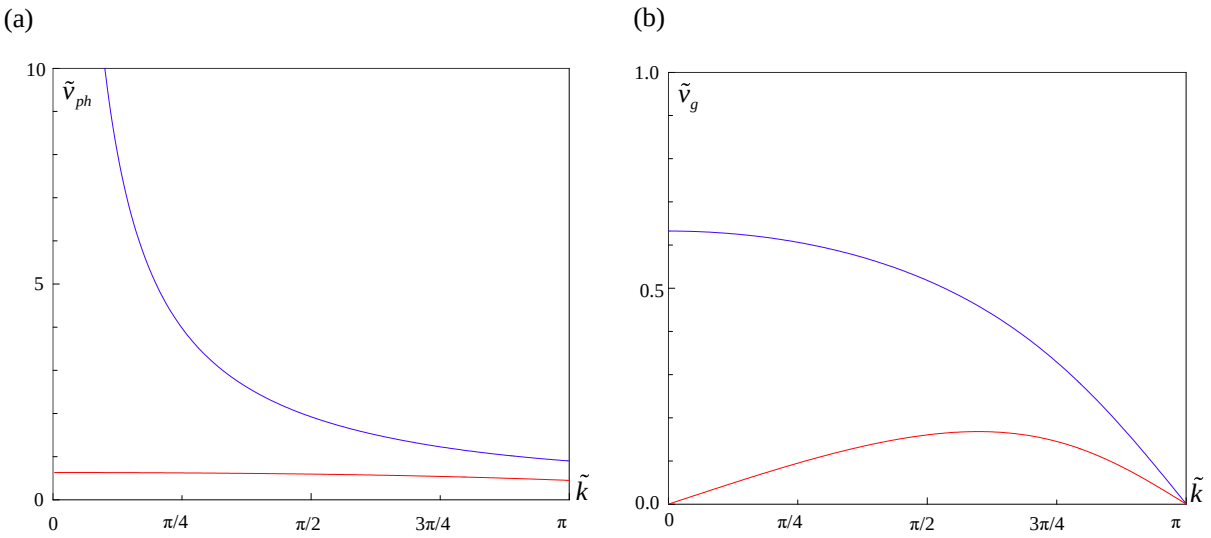

Figure 2.18 (a) Phase velocity, (b) Group velocity in the undamped biatomic lattice material.

2.4. Damped biatomic lattice material

The model of the biatomic lattice material can be enriched by adding a viscoelastic device, characterized by a translational relaxation function k_d and a stiffness k_m that simulates the linear interaction between tha atoms of the adjacent cells (Figure 2.19). The free damped vibrations of the discrete model are governed by integral-differential equations of motion

$$\begin{cases} m_1\ddot{u}_i + 2k_m u_i - k_m u_{i-1} - k_m u_{i+1} + \int_{-\infty}^{t} k_d(t-\tau)\frac{d}{d\tau}(u_i - u_{i-1})d\tau + \int_{-\infty}^{t} k_d(t-\tau)\frac{d}{d\tau}(u_i - u_{i+1})d\tau = 0 \\ m_2\ddot{u}_{i+1} + 2k_r u_{i+1} - k_r u_i - k_r u_{i+2} + \int_{-\infty}^{t} k_d(t-\tau)\frac{d}{d\tau}(u_{i+1} - u_i)d\tau + \int_{-\infty}^{t} k_d(t-\tau)\frac{d}{d\tau}(u_{i+1} - u_{i+2})d\tau = 0, \end{cases} \tag{2.22}$$

where the Boltzmann's integral formulation is used for the viscoelastic terms.

By using the Prony series (2.10) for the translational relaxation function and by applying the Floquet-Bloch conditions (2.16) and the bilateral Laplace transform to the equations (2.22) it can be obtained

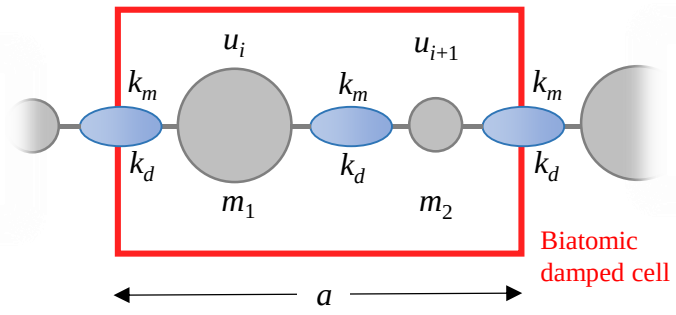

Figure 2.19 Damped biatomic lattice material.

$$\begin{cases}\left(m_1 s^2+2\dfrac{k_{d1}t_r s}{1+st_r}+2k_m\right)\hat{u}_i-k_m(1+e^{-\imath ka})\hat{u}_{i+1}-\dfrac{k_{d1}t_r s}{1+st_r}(1+e^{-\imath ka})\hat{u}_{i+1}=0\\ \left(m_2 s^2+2\dfrac{k_{d1}t_r s}{1+st_r}+2k_m\right)\hat{u}_{i+1}-k_m(1+e^{\imath ka})\hat{u}_i-\dfrac{k_{d1}t_r s}{1+st_r}(1+e^{\imath ka})\hat{u}_i=0,\end{cases} \tag{2.23}$$

where the bilateral Laplace transform can be approximated with its first order Taylor polynomials centered at $s=0$ (2.12), modeled by a viscoelastic device constituted by a spring connected in parallel to a dashpot (Figure 2.20).

By dividing the first and the second equation (2.23) by m_1 and m_2, respectively, the equations can be written in matrix form as

$$\begin{bmatrix} s^2+2\xi_{d1}s+2\omega_{m1}^2 & -\omega_{m1}^2(1+e^{-\imath ka})-\xi_{d1}s(1+e^{-\imath ka}) \\ -\omega_{m2}^2(1+e^{\imath ka})-\xi_{d2}s(1+e^{\imath ka}) & s^2+2\xi_{d2}s+2\omega_{m2}^2 \end{bmatrix}\begin{pmatrix}\hat{u}_i\\ \hat{u}_{i+1}\end{pmatrix}=\begin{pmatrix}0\\0\end{pmatrix}, \tag{2.24}$$

where $\xi_{d1}=k_{d1}t_r/m_1$, $\xi_{d2}=k_{d1}t_r/m_2$ in the following sections are called *damping parameters*.

By introducing the non-dimensional variable $\tilde{s}=s/s_0$, the non-dimensional wavenumber $\tilde{k}=ka$ and non-dimensional parameters $\tilde{\gamma}=\omega_{m2}/\omega_{m1}$, $\tilde{\xi}_{d1}=\xi_{d1}/s_0$ and $\tilde{\xi}_{d2}=\xi_{d2}/s_0$, where s_0 is a real-valued circular frequency that can be arranged equal to ω_m, the complex-valued dispersion relations are obtained by equating to zero the characteristic polynomial

$$\tilde{s}^4+b_3\tilde{s}^3+b_2\tilde{s}^2+b_1\tilde{s}+b_0=0, \tag{2.25}$$

where the coefficients b_3, b_2, b_1, b_0 are

$$\begin{aligned} b_3&=2\tilde{\xi}_{d1}+2\tilde{\xi}_{d2}, \quad b_2=2+2\tilde{\gamma}^2+2\tilde{\xi}_{d1}\tilde{\xi}_{d2}-\tilde{\xi}_{d1}\tilde{\xi}_{d2}\cos\tilde{k}\\ b_1&=2\tilde{\gamma}^2\tilde{\xi}_{d1}+2\tilde{\xi}_{d2}-2\tilde{\gamma}^2\tilde{\xi}_{d1}\cos\tilde{k}-2\tilde{\xi}_{d2}\cos\tilde{k}\\ b_0&=2\tilde{\gamma}^2-2\tilde{\gamma}^2\cos\tilde{k}. \end{aligned} \tag{2.26}$$

The solutions of the equation (2.25) are (Figure 2.21)

$$\tilde{s}_{1,2}=-\frac{b_3}{4}-Q\pm\frac{1}{2}\sqrt{-4Q^2-2p+\frac{C}{Q}}, \quad \tilde{s}_{3,4}=-\frac{b_3}{4}-Q\pm\frac{1}{2}\sqrt{-4Q^2-2p-\frac{C}{Q}}, \tag{2.27}$$

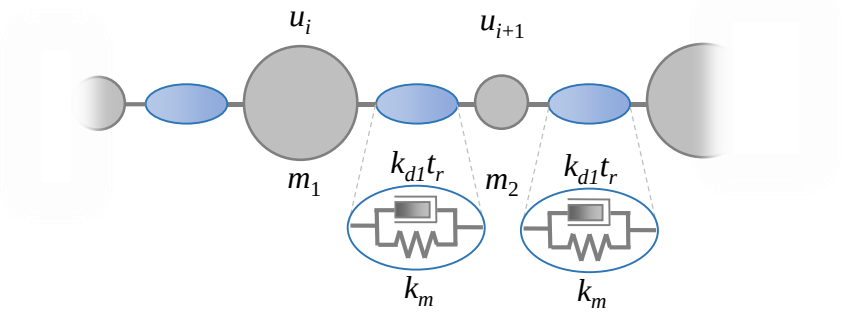

Figure 2.20 Damped biatomic lattice material with springs and dashpots.

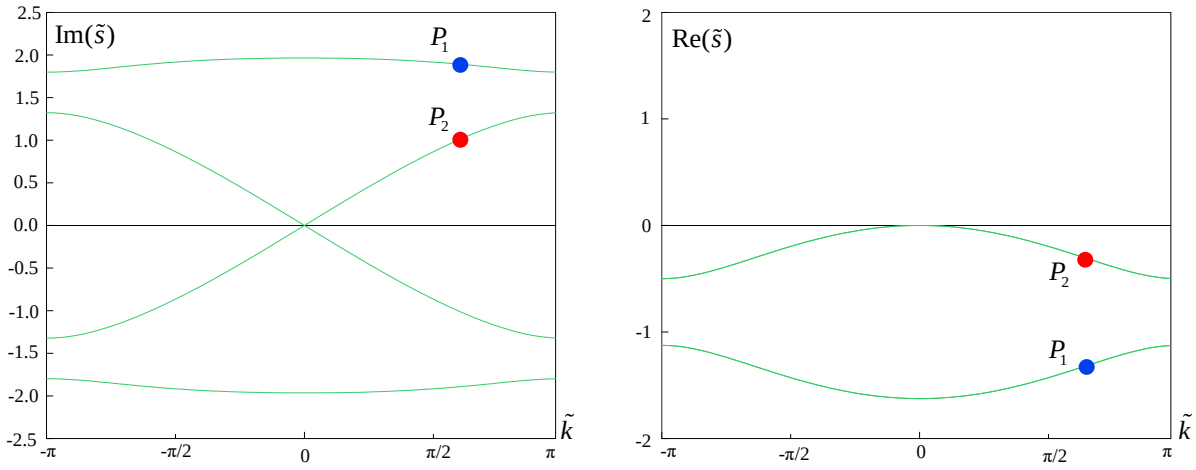

Figure 2.21 Dispersion curves of damped biatomic lattice material ($\tilde{\gamma}=1.5$, $\tilde{\xi}_{d1}=0.5$, $\tilde{\xi}_{d2}=2.25$).

in which

$$
\begin{aligned}
Q &= \frac{1}{2}\sqrt{-\frac{2}{3}p+\frac{1}{3}\left(d+\frac{q}{d}\right)}, \\
p &= \frac{8b_2-3b_3^2}{8}, \\
C &= \frac{8b_1-4b_3b_2+b_3}{8}, \\
d &= \sqrt[3]{\frac{c+\sqrt{c^2-4q^3}}{2}}, \\
q &= 12b_0-3b_3b_1+b_2^2, \\
c &= 27b_1^2-72b_2b_0+27b_3^2b_0-9b_3b_2b_1+2b_2^3.
\end{aligned}
\tag{2.28}
$$

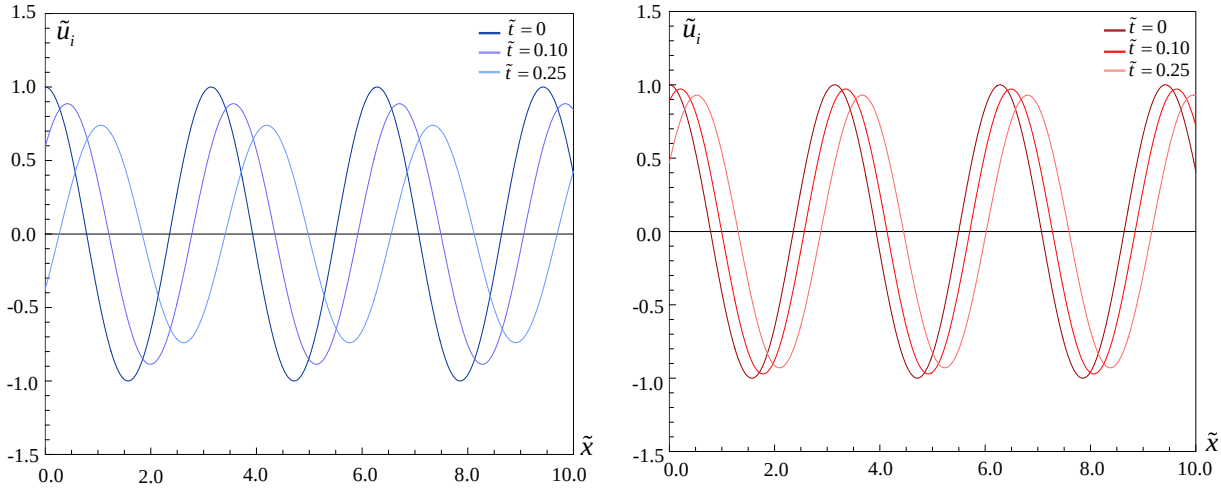

Figure 2.22 Displacement of the *i*-th mass of the damped biatomic lattice material ($\tilde{k}=2$).

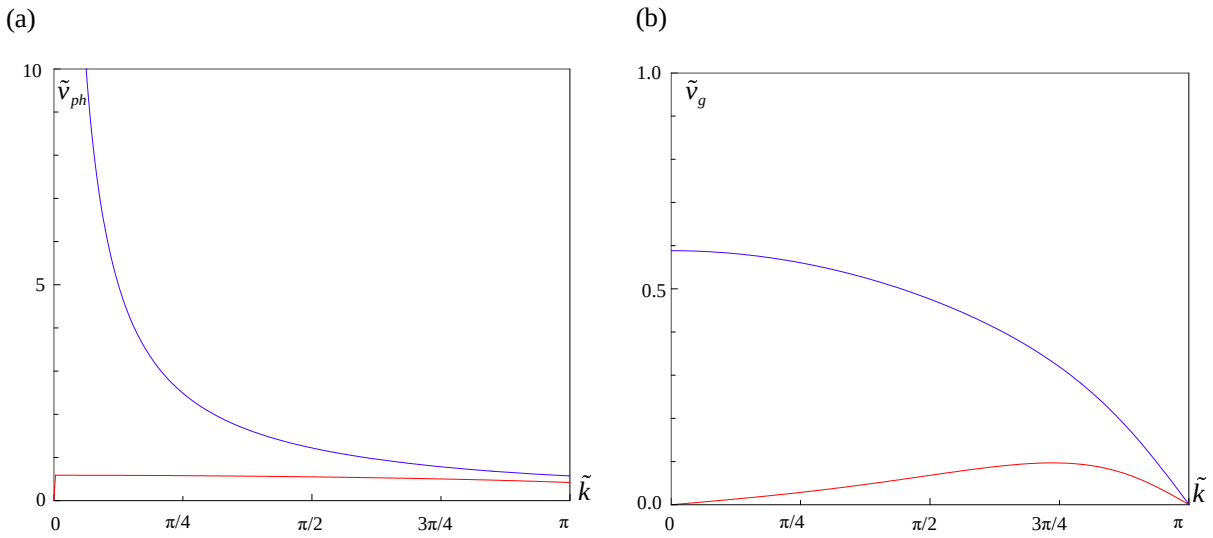

Figure 2.23 (a) Phase velocity, (b) Group velocity in the damped biatomic lattice material.

Chosen the value of the wavenumber equal to 2, from the dispersion relation the values of the variable $\tilde{s}$ are obtained ($\tilde{s} = -1.32423 + 1.88237\imath$ corresponding to point P_1 and $\tilde{s} = -0.300773 + 1.05481\imath$ corresponding to point P_2 in Figure 2.21), and the displacement $\tilde{u}_i$ of *i*-th mass is achieved (Figure 2.22). A difference between the dissipation of the displacement associated to the points P_1 and P_2 is observed and this is in relation with the different value of the *damping ratio* in the points. Furthermore, also the velocity of propagation are different and effectively the phase velocity, defined by the relation (2.7), associated to the points P_1 and P_2, assumes the values $\tilde{v}_{ph} = 0.941187$ and $\tilde{v}_{ph} = 0.527405$, respectively.

The group velocity can be obtained differentiating with respect to $\tilde{k}$ the relations (2.27)

$$\tilde{v}_{g1,2} = -\frac{1}{4}b_3^{'} - Q' \pm \frac{\frac{C'}{Q} - \frac{CQ'}{Q^2} - 2p' - 8QQ'}{4\sqrt{-4Q^2 - 2p + \frac{C}{Q}}}$$
$$\tilde{v}_{g3,4} = -\frac{1}{4}b_3^{'} - Q' \pm \frac{-\frac{C'}{Q} + \frac{CQ'}{Q^2} - 2p' - 8QQ'}{4\sqrt{-4Q^2 - 2p - \frac{C}{Q}}}, \quad (2.29)$$

where the derivative with respect $\tilde{k}$ is expressed with the Lagrange's notation as $f' = df / d\tilde{k}$, where f is a generic $\tilde{k}$-dependent function.

Given the symmetry about $\tilde{k} = 0$ of the dispersion diagram the phase velocity and the group velocity are evaluated in the Irreducible Brillouin zone and for positive *wave frequency* (Figure 2.23) and their trends are qualitatively the same as observed for undamped biatomic lattice.

2.5. Undamped biatomic lattice metamaterial

An alternative of a monodimensional biatomic lattice is represented by the mass-in-mass lattice where a circular inclusion (*secondary atom*) is introduced inside each ring (*principal atom*) of the infinite chain. In the small-amplitude range of oscillations, the circular inclusions play the role of inertial resonators, if their linear frequencies are properly tuned with certain wave frequencies of the ring. From the mechanical viewpoint, the free dynamics of this metamaterial can be described by a low-dimensional discrete model (Figure 2.24). The massive and stiff ring is modeled as a rigid body with translational mass m_1 and the unique degree of freedom of the principal atom can be related to the displacement $u_i(t)$ of the configurational node located at the ring centroid. The internal inclusion is modeled as a point body with mass m_2 which configuration is described by the displacement $v_i(t)$. The linear interaction with the *principal atoms* of the adjacent cells is simulated by linear elastic spring with stiffness k_{m1}. The linear interaction between the *principal atom* and the *secondary atom* is simulated by linear elastic spring with stiffness k_{m2}. Furthermore, the lattice is ideally supposed to be perfectly non-dissipative. The free undamped dynamics of the elementary cell is governed by an ordinary differential equations of motion

$$\begin{cases} m_1\ddot{u}_i + 2k_{m1}u_i - k_{m1}u_{i-1} - k_{m1}u_{i+1} + k_{m2}(u_i - v_i) = 0 \\ m_2\ddot{v}_i + k_{m2}(v_i - u_i) = 0. \end{cases} \tag{2.30}$$

Given the periodicity of the system, the displacements of two adjacent cells are related by the Floquet-Bloch conditions

$$u_i = u_{i-1}e^{\imath ka} \qquad u_{i+1} = u_i e^{\imath ka}. \tag{2.31}$$

By applying the Floquet-Bloch conditions (2.31) and the bilateral Laplace transform to the equations (2.30) it can be obtained

$$\begin{cases} m_1 s^2\hat{u}_i + 2k_m\hat{u}_i - k_m(e^{\imath ka} + e^{-\imath ka})\hat{u}_i + k_m\hat{u}_i - k_m\hat{v}_i = 0 \\ (m_2 s^2 + k_m)\hat{v}_i - k_m\hat{u}_i = 0, \end{cases} \tag{2.32}$$

where it is assumed $k_{m1} = k_{m2} = k_m$.

Dividing the first and the second equation (2.32) by m_1 and m_2, respectively, the equations (2.32) are rewritten in the matrix form as

$$\begin{bmatrix} s^2 + \omega_{m1}^2(2 - e^{-\imath ka} - e^{\imath ka}) + \omega_{m1}^2 & -\omega_{m1}^2 \\ -\omega_{m2}^2 & s^2 + \omega_{m2}^2 \end{bmatrix} \begin{pmatrix} \hat{u}_i \\ \hat{v}_i \end{pmatrix} = \begin{pmatrix} 0 \\ 0 \end{pmatrix}, \tag{2.33}$$

where $\omega_{m1}^2 = k_m / m_1, \omega_{m2}^2 = k_m / m_2$ are the square of the *circular frequencies* of the harmonic oscillators with mass m_1 and m_2, respectively, and stiffness k_m.

By introducing the non-dimensional parameter $\tilde{\gamma} = \omega_{m2} / \omega_{m1}$, the wavenumber $\tilde{k} = ka$ and the variable $\tilde{s} = s / s_0$, where s_0 is a real-valued circular frequency that can be arranged equal to ω_{m1}, the dispersion relations are found by solving the eigenvalues problem associated to (2.33). By equating to zero the characteristic polynomial, the equation to be solved is

$$\tilde{s}^4 + 3\tilde{s}^2 + \tilde{s}^2\tilde{\gamma}^2 - e^{-\imath\tilde{k}}\tilde{s}^2\tilde{\gamma}^2 - e^{\imath\tilde{k}}\tilde{s}^2\tilde{\gamma}^2 + 2\tilde{\gamma}^2 - e^{-\imath\tilde{k}}\tilde{\gamma}^2 - e^{\imath\tilde{k}}\tilde{\gamma}^2 = 0, \tag{2.34}$$

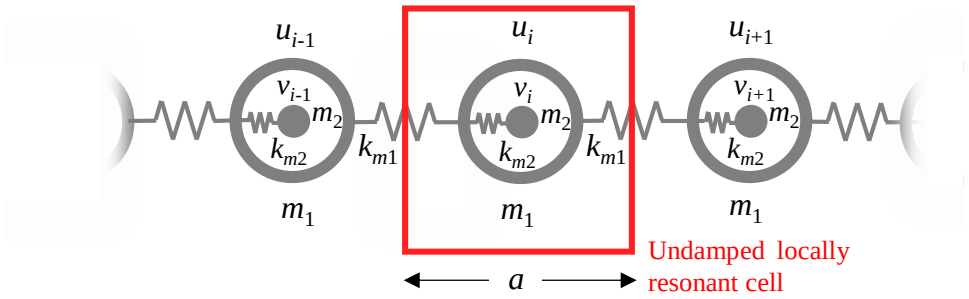

Figure 2.24 Undamped biatomic lattice metamaterial.

The relations between the variable $\tilde{s}$ and the wavenumber $\tilde{k}$ in trigonometric form are (Figure 2.25)

$$\tilde{s}_{1,2} = \pm\sqrt{\frac{b-\sqrt{b^2-4\left(2\tilde{\gamma}^2-2\tilde{\gamma}^2\cos\tilde{k}\right)}}{2}}$$
$$\tilde{s}_{3,4} = \pm\sqrt{\frac{b+\sqrt{b^2-4\left(2\tilde{\gamma}^2-2\tilde{\gamma}^2\cos\tilde{k}\right)}}{2}}, \tag{2.35}$$

where $b=-3-\tilde{\gamma}^2+2\cos\tilde{k}$.

Two *band gaps* can be observed in the dispersion diagram and their amplitude are conditioned by the parameter $\tilde{\gamma}$ (Figure 2.26). When the ratio $\tilde{\gamma}$ increases the band amplitude decrease for $0\le\tilde{\gamma}\le1$ and it increases for $1\le\tilde{\gamma}\le10$ but it doesn't vanish. Futhermore, the center frequency of the *band gap* is in the vicinity of resonat frequency of the internal inclusion and it is not related to the wavelength. This allows to state that can be produce a *band gap* at arbitrarily low-frequencies/long wavelengths.

Fixing the value of the wavenumber $\tilde{k}$ equal to 2, to which the positive values $\tilde{s}=2.43267\imath$ and $\tilde{s}=1.38361\imath$ (points P_1 and P_2 in Figure 2.25) obtained through the dispersion relations (2.35) correspond, the displacement $\tilde{u}_i$ of *i*-th mass is achieved (Figure 2.27). Different velocities of propagation associated to the points P_1 and P_2 are observed and, effectively, the phase velocity, defined

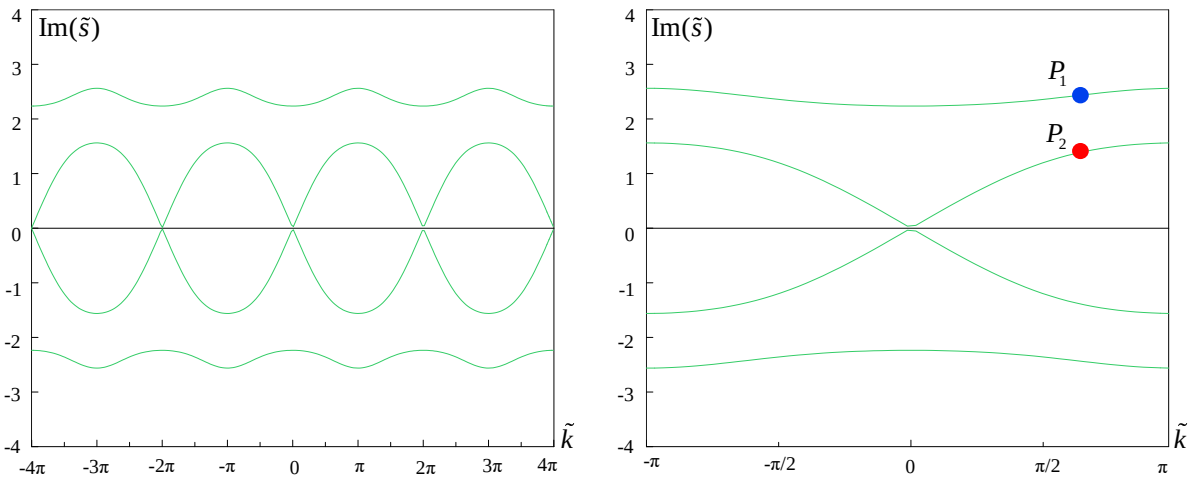

Figure 2.25 Dispersion curves of undamped biatomic lattice metamaterial ($\tilde{\gamma}=2$).

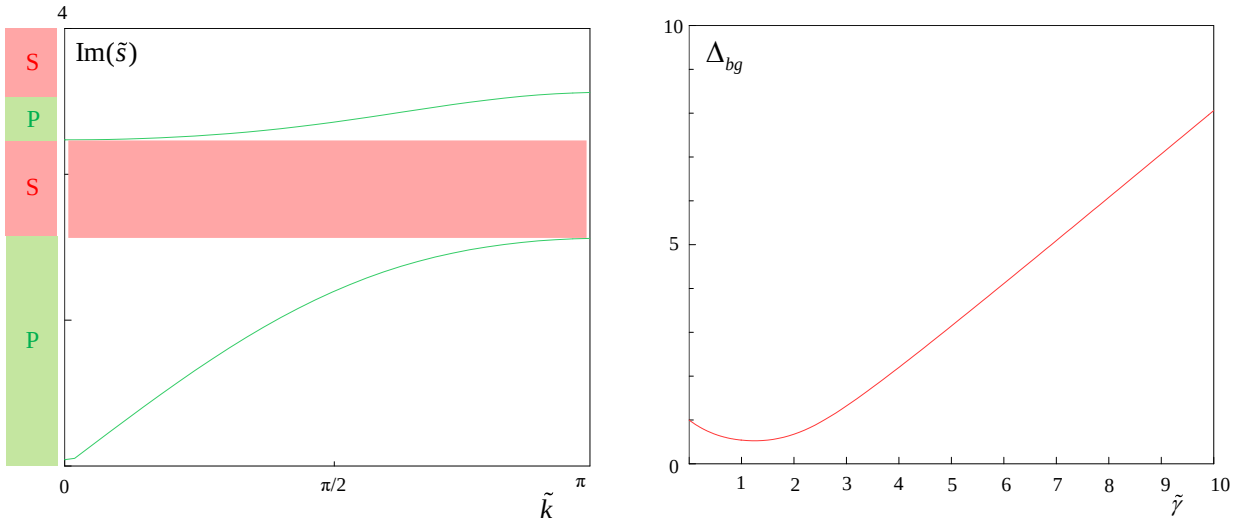

Figure 2.26 (a) Band gap in the dispersion diagram of undamped biatomic lattice metamaterial ($\tilde{\gamma} = 2$), (b) Band gap amplitude.

by the relation (2.7), associated to the points P_1 and P_2, assumes the values $\tilde{v}_{ph} = 1.21634$ and $\tilde{v}_{ph} = 0.681807$, respectively.

The group velocity can be obtained deriving with respect to $\tilde{k}$ the relations (2.35)

$$\tilde{v}_{g1,2} = \pm\left(b' - \frac{-8\tilde{\gamma}^2 \sin\tilde{k} + 2bb'}{4c\sqrt{2(b-c)}} \right)$$
$$\tilde{v}_{g3,4} = \pm\left(b' + \frac{-8\tilde{\gamma}^2 \sin\tilde{k} + 2bb'}{4c\sqrt{2(b+c)}} \right), \tag{2.36}$$

where $b = -3 - \tilde{\gamma}^2 + 2\cos\tilde{k}$ and $c = \sqrt{b^2 - 4(2\tilde{\gamma}^2 - 2\tilde{\gamma}^2\cos\tilde{k})}$.

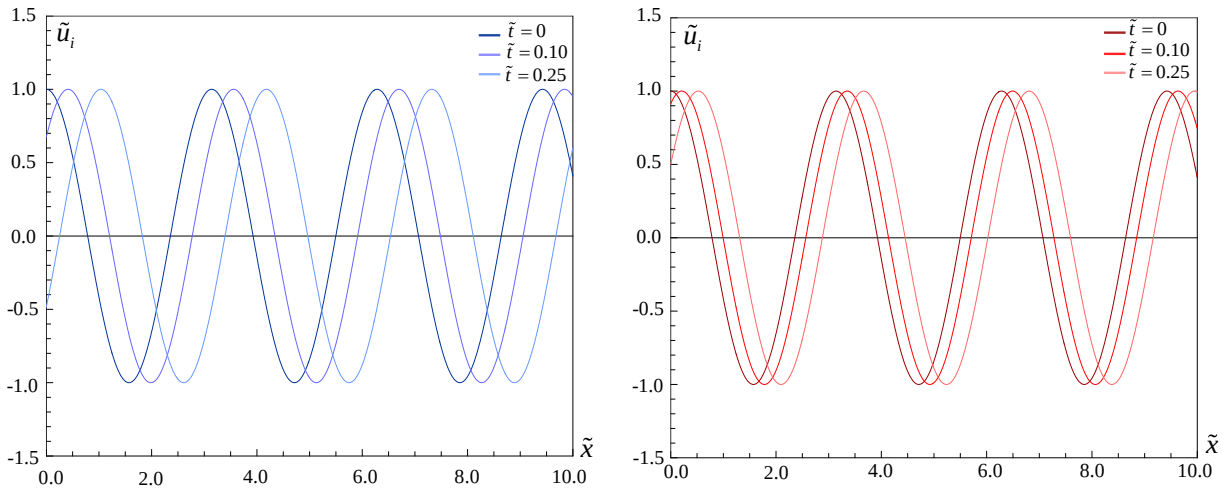

Figure 2.27 Displacement of the *i*-th mass of the undamped biatomic lattice metamaterial ($\tilde{k} = 2$).

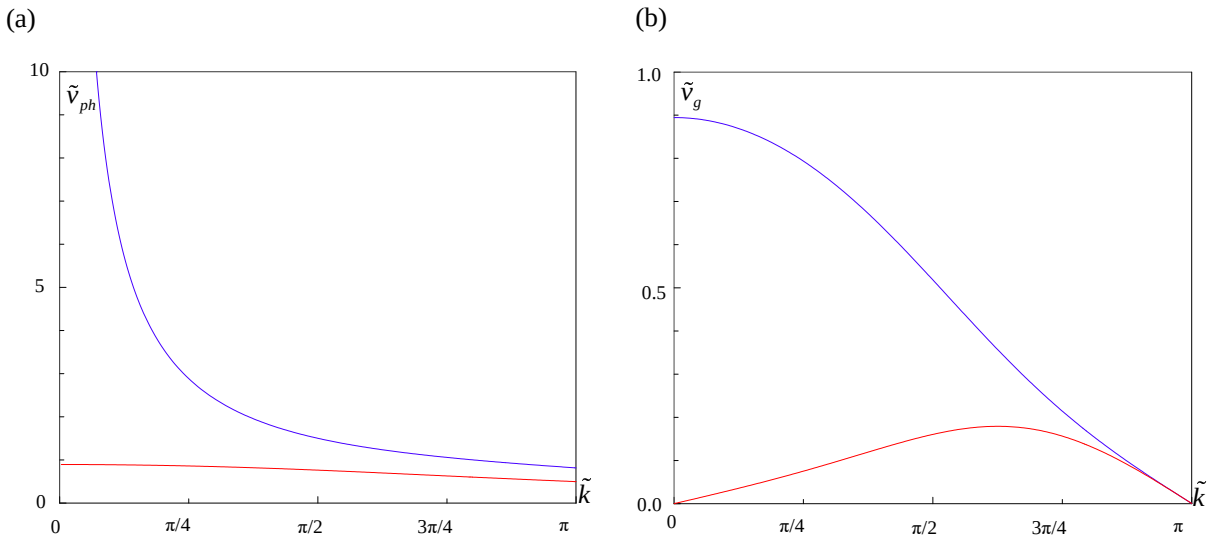

Figure 2.28 (a) Phase velocity, (b) Group velocity in the undamped biatomic lattice metamaterial.

Given the symmetry about $\tilde{k}=0$ of the dispersion diagram the phase velocity and the group velocity are evaluated in the Irreducible Brillouin zone and for positive *wave frequency* (Figure 2.28) and their trends are qualitatively the same observed for undamped biatomic lattice.

2.6. Damped biatomic lattice metamaterial

The model of the biatomic lattice material can be enriched by adding a viscoelastic device, characterized by a translational relaxation function k_d and a stiffness k_m that simulates the linear interaction between tha atoms of the adjacent cells (Figure 2.29). The free damped vibrations of the discrete model are governed by integral-differential equation of motion

$$\begin{cases} m_1\ddot{u}_i + 2k_{m1}u_i - k_{m1}u_{i-1} - k_{m1}u_{i+1} + k_{m2}(u_i - v_i) + \int_{-\infty}^{t} k_d(t-\tau)\dfrac{d}{d\tau}(u_i - v_i)d\tau = 0 \\ m_2\ddot{v}_i + k_{m2}(v_i - u_i) + \int_{-\infty}^{t} k_d(t-\tau)\dfrac{d}{d\tau}(v_i - u_i) = 0, \end{cases} \tag{2.37}$$

where the Boltzmann's integral formulation is used for the viscoelastic terms.

By using the Prony series for the translational relaxation function (2.10) and applying the Floquet-Bloch conditions (2.31) and the bilateral Laplace transform to the equations (2.37) it can be obtained

$$\begin{cases} m_1 s^2\hat{u}_i + 2k_m\hat{u}_i - k_m(e^{\imath ka} + e^{-\imath ka})\hat{u}_i + \left(k_m + \dfrac{k_{d1}t_r s}{1+st_r}\right)(\hat{u}_i - \hat{v}_i) = 0 \\ \left(m_2 s^2 + k_m + \dfrac{k_{d1}t_r s}{1+st_r}\right)\hat{v}_i - \left(k_m + \dfrac{k_{d1}t_r s}{1+st_r}\right)\hat{u}_i = 0, \end{cases} \tag{2.38}$$

where it is assumed $k_{m1} = k_{m2} = k_m$. The bilateral Laplace transform $\mathcal{L}[k_d] = \int_{-\infty}^{\infty} k_d e^{-st}dt = k_{d1}t_r/(1+st_r)$ can be approximated with their first order Taylor polynomials centered at $s=0$ (2.12), modeled by a

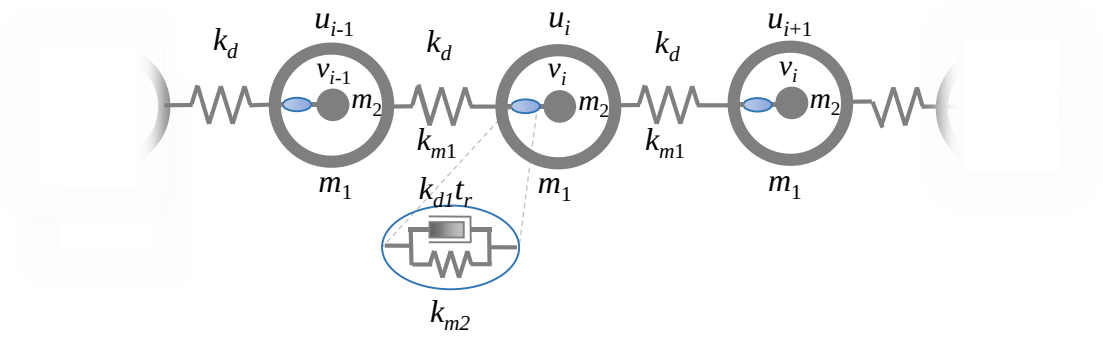

Figure 2.29 Damped biatomic lattice metamaterial.

viscoelastic device constituted by a spring connected in parallel to a dashpot as in the Figure 2.30.

By dividing the first and the second equation (2.38) by m_1 and m_2, respectively, the equations can be written in matrix form as

$$\begin{bmatrix} s^2+\omega_{m1}^2(2-e^{-\imath ka}-e^{\imath ka})+\omega_{m1}^2+\xi_{d1}s & -\omega_{m1}^2-\xi_{d1}s \\ -\omega_{m2}^2-\xi_{d2}s & s^2+\omega_{m2}^2+\xi_{d2}s \end{bmatrix}\begin{pmatrix}\hat{u}_i\\ \hat{v}_i\end{pmatrix}=\begin{pmatrix}0\\0\end{pmatrix}, \tag{2.39}$$

where $\xi_{d1}=k_{d1}t_r/m_1$, $\xi_{d2}=k_{d1}t_r/m_2$ in the following sections are called *damping parameters*.

By introducing the non-dimensional variable $\tilde{s}=s/s_0$, the non-dimensional wavenumber $\tilde{k}=ka$ and non-dimensional parameters $\tilde{\gamma}=\omega_{m2}/\omega_{m1}$, $\tilde{\xi}_{d1}=\xi_{d1}/s_0$ and $\tilde{\xi}_{d2}=\xi_{d2}/s_0$, where s_0 is a real-valued circular frequency that can be arranged equal to ω_m, the complex-valued dispersion relations are obtained by equating to zero the characteristic polynomial

$$\tilde{s}^4+b_3\tilde{s}^3+b_2\tilde{s}^2+b_1\tilde{s}+b_0=0, \tag{2.40}$$

where the coefficients b_3,b_2,b_1,b_0 are

$$\begin{aligned} b_3&=\tilde{\xi}_{d1}+\tilde{\xi}_{d2}\\ b_2&=3+\tilde{\gamma}^2-2\cos\tilde{k}\\ b_1&=2\tilde{\xi}_{d2}-2\tilde{\xi}_{d2}\cos\tilde{k}\\ b_0&=2\tilde{\gamma}^2-2\tilde{\gamma}^2\cos\tilde{k}. \end{aligned} \tag{2.41}$$

The solutions of the equation (2.40) are expressed by the relations (2.27) by substituting the coefficients (2.41) (Figure 2.31).

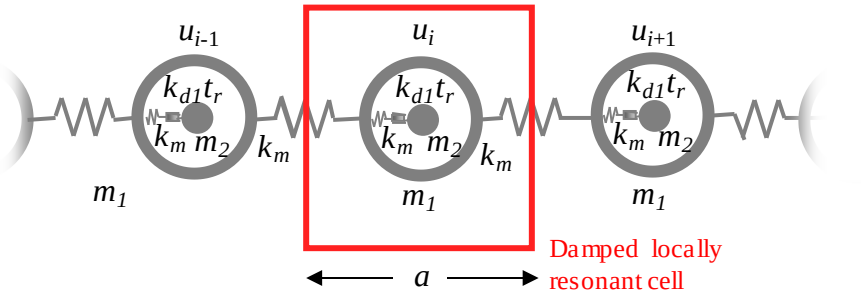

Figure 2.30 Damped biatomic lattice metamaterial with springs and dashpots.

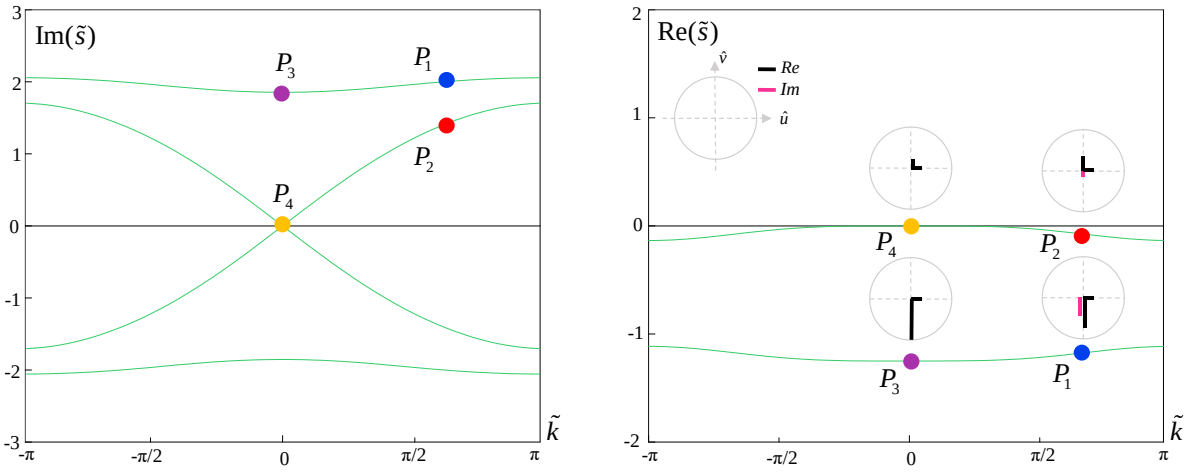

Figure 2.31 Dispersion curves and eigenvectors of damped biatomic lattice metamaterial and selected samples of the self-normalized waveforms φ in the unitary circle of the Lagrangian coordinate space ($\tilde{\gamma}=2$, $\tilde{\xi}_{d1}=0.5$, $\tilde{\xi}_{d2}=2$).

Solved the eigenvalues problem, fixeing the $\tilde{k}$ -value and by achieving the values of the variable $\tilde{s}$ from the dispersion spectrum, it is possible obtain the associated eigenvector. For $\tilde{k}=0$, the eigencomponents $\hat{u}$ and $\hat{v}$ are real-valued. In particular, fixing a mass-othonormalization for the eigenvectors, for $\tilde{s}=0$ (point P_4 in the Figure 2.31) the eigencomponents are positive and identical (no local wave dynamics of the resonator), while for $\tilde{s}=-1.25+1.854\imath$ (point P_3 in the Figure 2.31) the eigencomponent $\hat{u}$ is positive and the eigencomponent $\hat{v}$ is negative (local wave dynamics of the resonator). For $\tilde{k}=0$, the dispersion curve with same-sign eigencomponents is called *acoustic* curve (the centroid of all the cell masses moves as in sound propagation) and the curve with opposite-sign eigencomponents is called *optical* curve. The eigenvectors are complex for different values of the wavenumber $\tilde{k}$ as it can be observed for the values associated to the points P_1 and P_2 ($\tilde{k}=2$, $\tilde{s}=-1.18307+2.00734\imath$ for the point P_1 and $\tilde{s}=-0.0669253+1.44307\imath$ for the point P_2 in Figure 2.31).

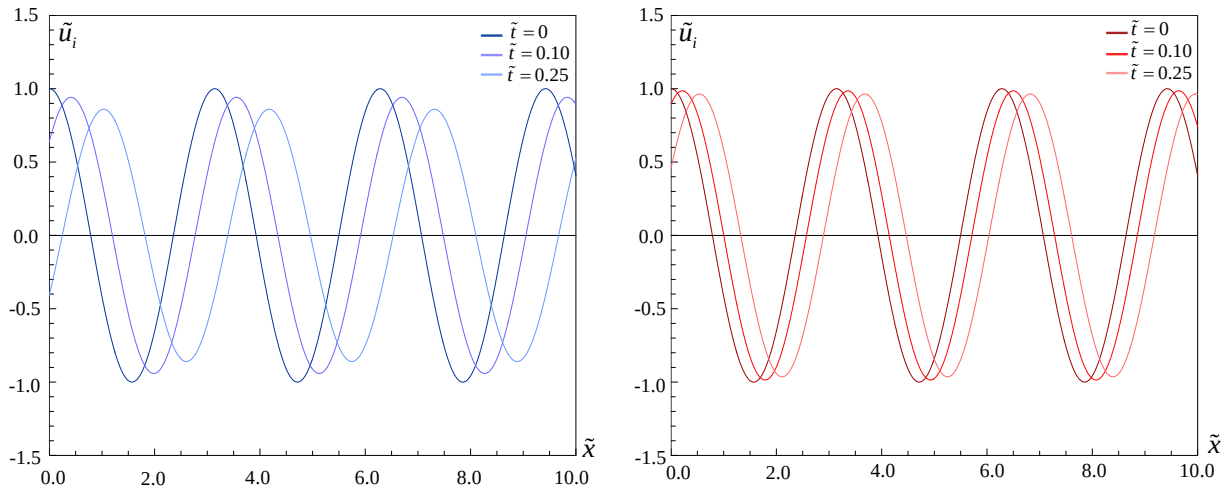

Figure 2.32 Displacement of the *i*-th mass of the damped biatomic lattice metamaterial ($\tilde{k}=2$).

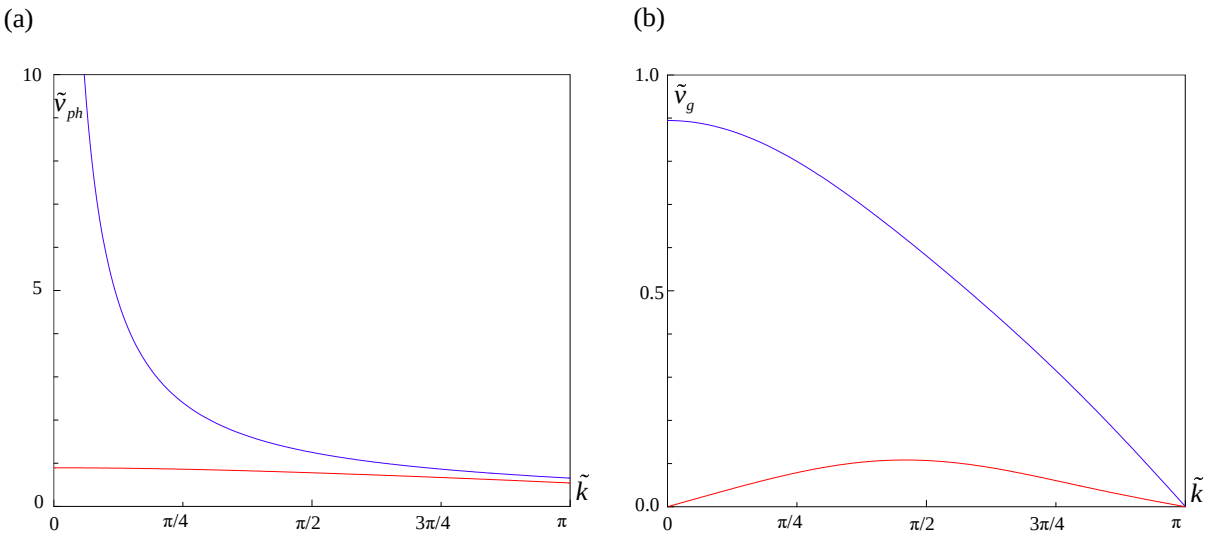

Figure 2.33 (a) Phase velocity, (b) Group velocity in the damped biatomic lattice metamaterial.

Chosen the value of the wavenumber $\tilde{k}$ equal to 2, from the dispersion spectrum the values of the variable $\tilde{s}$ is obtained and the displacement $\tilde{u}_i$ of *i*-th mass is achieved (Figure 2.32). A difference between the dissipation of the displacement associated to the points P_1 and P_2 is observed and this is in relation with the different value of the *damping ratio* in the points. Furthermore, also the velocity of propagation is different and effectively the phase velocity, defined by the relation (2.7), associated to the points P_1 and P_2, assumes the values $\tilde{v}_{ph} = 1.00362$ and $\tilde{v}_{ph} = 0.721533$, respectively.

The group velocity can be obtained with the (2.29) where the coefficients b_3, b_2, b_1, b_0 are expressed by the relations (2.41). Given the symmetry about $\tilde{k} = 0$ of the dispersion diagram the phase velocity and the group velocity are evaluated in the Irreducible Brillouin zone and for positive *wave frequency* (Figure 2.33) and their trends are qualitatively the same observed for undamped biatomic lattice.

CHAPTER 3

ELASTIC BEAM LATTICE

Beam lattice materials are characterized by a periodic microstructure realizing a geometrically regular pattern of elementary cells. Unlike the crystal lattices, in which the reciprocal interactions between pairs of atoms are purely attractive and repulsive, in the beam lattices the elastic coupling between close pairs of atomic nodes can be described through the definition of axial-bending interactions.

The current research interest is focused on the assessment and customization of the dispersion properties associated to the propagation of Bloch waves across the material, either in its original periodic microstructured form or in equivalent homogenized forms. In this respect, the periodic materials with a chiral or anti-chiral microstructure of the elementary cell, consisting of stiff disks or rings, tangentially connected by a variable number of flexible ligaments (Figure 3.1), are particularly attractive for their potential as acoustic waveguides or phononic filters. In the current literature dealing with this material class, the pass and stop bands characterizing the band spectrum have been determined by solving the dispersion problem related to low-dimensional discrete models, high-fidelity micromechanical formulations accounting for the material heterogeneity at the microscale and, finally, equivalent local and non-local homogenized continua.

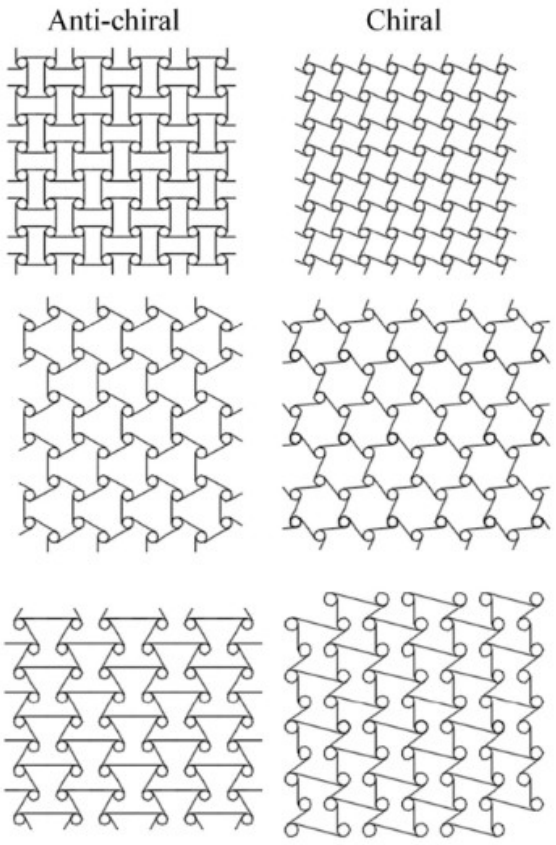

Figure 3.1 Anti-chiral and chiral microstructured materials (Wu et al., 2019).

The leading idea is that, within certain physically admissible ranges, the geometric and mechanical parameters can be intended as freely tunable variables for properly customizing the acoustic dispersion properties of the material. Common customization criteria are the presence of selected harmonics in the band structure at a certain wavenumber, the opening or shifting of maximum-amplitude band gaps in the lowest possible frequency range.

Asymptotic perturbation-based techniques may allow the multiparametric approximation of the direct and inverse dispersion problem for low-dimensional discrete models. Consequently, the conditions for the existence of pass and stop bands, as well as the design of their centerfrequency and amplitude can be determined in a suited analytical – although approximate – form. Although powerful for the availability of valuable analytical solutions, the perturbation-based optimization analyses may highlight how low-dimensional discrete models possess a low-dimensional parameter space, insufficient for the search of a satisfying solution for inverse spectral problems.

This chapter is devoted to exploring the dispersion properties of the tetrachiral material in the larger parameter space obtainable by removing some of the simplifying mechanical assumption limiting the simpler discrete model. Two alternative continuous models (high-fidelity first-order heterogeneous and equivalent homogenized micropolar continuum) are derived in parallel to the Lagrangian beam lattice formulation (Section 3.1). The frequency dispersion spectra resulting from all the models are compared to each other and cross-validated (Sections 3.2). The qualitative and qualitative agreement between asymptotic perturbation-based approximations and numerical spectral solutions is discussed (Paragraph 3.2.1). Parametric analyses concerning the effects of variations in the enlarged space of geometric and mechanical parameters on the acoustic and optical surfaces are carried out (Section 3.3). Consequently, a tuning of the micromechanical properties is employed to verify the filtering functionality of the material in the forced wave propagation under harmonic boundary excitation (Paragraph 3.3.1, 3.3.2). Finally, a parametric optimization for the search of full and partial band gaps with the largest amplitude and lower center frequency is carried out (Section 3.4).

3.1. Tetrachiral material

3.1.1.Beam lattice model

The class of chiral and antichiral cellular materials is characterized by a periodic tessellation of the bidimensional plane. The elementary cell is strongly characterized by a microstructure composed by stiff circular rings connected by flexible straight ligaments, arranged according to different planar geometries including the trichiral, hexachiral, tetrachiral, anti-trichiral, antitetrachiral topologies. Among the others, the tetrachiral material is featured by a monoatomic centrosymmetric cell in which the central stiff and massive ring (or disk) is connected to four tangent flexible and light ligaments (Figure 3.2a). The periodic square cell has side length H. Each ring is mechanically modeled as a rigid annular body with mass M_r, rotational inertia J_r, mean radius R and transversal width t_r, (Figure 3.2b). Each ligament is modeled as

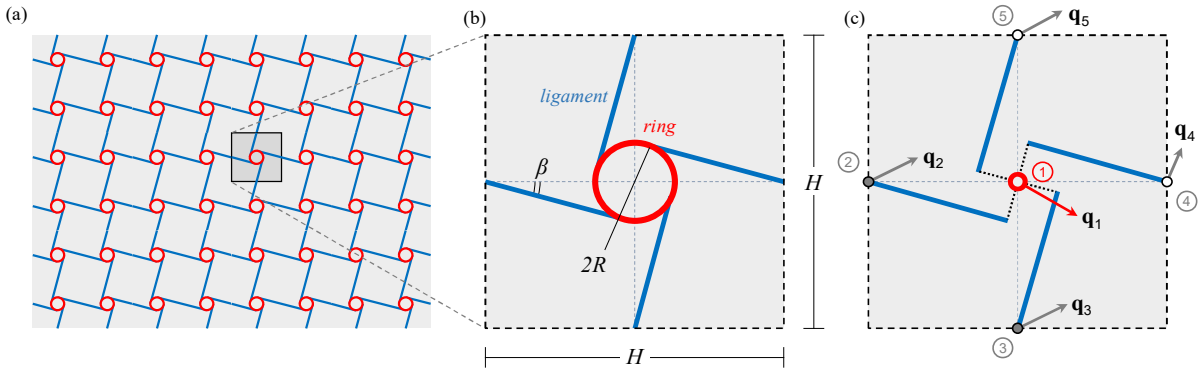

Figure 3.2 Tetrachiral metamaterial (a) repetitive planar pattern, (b) periodic cell, (c) beam lattice model.

a linear unshearable beam, with material density ρ_b, transversal width t_b and natural length $L_b = H\cos\beta$, where the *chirality angle* $\beta = \arcsin(2R/H)$ is the ligament inclination angle with respect to the ideal line connecting the centers of adjacent rings. A linear elastic material, with Young's modulus E_b is assumed for all beams.

The rigid body configuration is fully described by three planar *active* degrees-of-freedom, collected in the generalized displacement vector $\mathbf{q}_a = \mathbf{q}_1$ (Figure 3.2c), referred to the internal node located at the ring barycenter. Due to the geometric periodicity, the cell boundary crosses the midspan of all the four ligaments. Consequently four external nodes are located at the midpoint of all the cell sides, each one possessing three planar *passive* degrees-of-freedom collected in the displacement vector $\mathbf{q}_p = (\mathbf{q}_2,...,\mathbf{q}_5)$.

Assuming the ligaments rigidly connected to the ring, a discrete beam lattice model can be formulated. The free undamped vibrations of the discrete model are governed by a linear equation, defined in the full configuration vector $\mathbf{q} = (\mathbf{q}_a, \mathbf{q}_p)$

$$\begin{bmatrix} \mathbf{M} & \mathbf{O} \\ \mathbf{O} & \mathbf{O} \end{bmatrix} \begin{pmatrix} \ddot{\mathbf{q}}_a \\ \ddot{\mathbf{q}}_p \end{pmatrix} + \begin{bmatrix} \mathbf{K}_{aa} & \mathbf{K}_{ap} \\ \mathbf{K}_{pa} & \mathbf{K}_{pp} \end{bmatrix} \begin{pmatrix} \mathbf{q}_a \\ \mathbf{q}_p \end{pmatrix} = \begin{pmatrix} \mathbf{0} \\ \mathbf{f}_p \end{pmatrix}, \tag{3.1}$$

where dot indicates differentiation with respect to time and $\mathbf{O}$ stands for different-size empty matrices. Adopting a lumped mass description, the non-null mass submatrix $\mathbf{M}$ is diagonal. The symmetric submatrices $\mathbf{K}_{aa}$ and $\mathbf{K}_{pp}$ describe the stiffness of the active and passive nodes, respectively. The rectangular submatrix $\mathbf{K}_{ap} = \mathbf{K}_{pa}^T$ account for the elastic coupling among the active and passive nodes. The non-null coefficients M_{ii} $(i = 1,2,3)$ of the mass submatrix $\mathbf{M}$ in the equation (3.1) are

$$M_{11} = M_{22} = M_r \qquad M_{33} = J_r \tag{3.2}$$

The non-null coefficients K_{ij}^{aa} $(i,j = 1,2,3)$ and K_{hs}^{pp} $(h,s = 1,...,12)$ of the symmetric submatrices $\mathbf{K}_{aa}$ and $\mathbf{K}_{pp}$ in the equation (3.1) are

$$K_{11}^{aa} = K_{22}^{aa} = 4E_b t_b (d^2 H^2 + 4t_b^2) d^{-3} H^{-3} \tag{3.3}$$

$$K_{33}^{aa} = \frac{8}{3} E_b t_b (3R^2 + t_b^2) d^{-1} H^{-1}$$

$$K_{11}^{pp} = K_{55}^{pp} = K_{77}^{pp} = K_{1111}^{pp} = 2E_b t_b (d^4 H^4 + 16R^2 t_b^2) d^{-3} H^{-5}$$

$$K_{12}^{pp} = K_{78}^{pp} = -4E_b t_b R\left(H^2 - 4t_b^2\right) d^{-2} H^{-4}$$

$$K_{45}^{pp} = K_{1011}^{pp} = 4E_b t_b R\left(H^2 - 4t_b^2\right) d^{-2} H^{-4}$$

$$K_{13}^{pp} = K_{56}^{pp} = 4E_b t_b^3 R d^{-2} H^{-3}$$

$$K_{79}^{pp} = K_{1112}^{pp} = -4E_b t_b^3 R d^{-2} H^{-3}$$

$$K_{22}^{pp} = K_{44}^{pp} = K_{88}^{pp} = K_{1010}^{pp} = 8E_b t_b (R^2 + t_b^2) d^{-1} H^{-3}$$

$$K_{23}^{pp} = K_{1012}^{pp} = 2E_b t_b^3 d^{-1} H^{-2}$$

$$K_{46}^{pp} = K_{89}^{pp} = -2E_b t_b^3 d^{-1} H^{-2}$$

$$K_{33}^{pp} = K_{66}^{pp} = K_{99}^{pp} = K_{1212}^{pp} = \frac{2}{3} E_b t_b^3 d^{-1} H^{-1},$$

where $d = \left(1 - 4R^2 / H^2\right)^{1/2}$.

The coefficients K_{ij}^{ap} $(i = 1,2,3; j = 1,...,12)$ of the rectangular submatrix $\mathbf{K}_{ap} = \mathbf{K}_{pa}^T$ in the equation (3.1) are

$$K_{11}^{ap} = K_{17}^{ap} = K_{25}^{ap} = K_{211}^{ap} = -2E_b t_b (d^4 H^4 + 16R^2 t_b^2) d^{-3} H^{-5} \tag{3.4}$$

$$K_{12}^{ap} = K_{21}^{ap} = K_{18}^{ap} = K_{27}^{ap} = 4E_b t_b R\left(H^2 - 4\left(R^2 + t_b^2\right)\right) d^{-2} H^{-4}$$

$$K_{15}^{ap} = K_{111}^{ap} = K_{24}^{ap} = K_{210}^{ap} = -4E_b t_b R\left(H^2 - 4\left(R^2 + t_b^2\right)\right) d^{-2} H^{-4}$$

$$K_{13}^{ap} = K_{26}^{ap} = -4E_b t_b^3 R d^{-2} H^{-3}$$

$$K_{19}^{ap} = K_{212}^{ap} = 4E_b t_b^3 R d^{-2} H^{-3}$$

$$K_{14}^{ap} = K_{110}^{ap} = K_{22}^{ap} = K_{28}^{ap} = -8E_b t_b (R^2 + t_b^2) d^{-1} H^{-3}$$

$$K_{16}^{ap} = K_{29}^{ap} = 2E_b t_b^3 d^{-1} H^{-2}$$

$$K_{112}^{ap} = K_{23}^{ap} = -2E_b t_b^3 d^{-1} H^{-2}$$

$$K_{31}^{ap} = K_{35}^{ap} = -2E_b t_b R\left(H^2 - 2\left(2R^2 + t_b^2\right)\right) d^{-2} H^{-3}$$

$$K_{37}^{ap} = K_{311}^{ap} = 2E_b t_b R\left(H^2 - 2\left(2R^2 + t_b^2\right)\right) d^{-2} H^{-3}$$

$$K_{32}^{ap} = K_{310}^{ap} = 2E_b t_b (2R^2 + t_b^2) d^{-1} H^{-2}$$

$$K_{34}^{ap} = K_{38}^{ap} = -2E_b t_b (2R^2 + t_b^2) d^{-1} H^{-2}$$

$$K_{33}^{ap} = K_{36}^{ap} = K_{39}^{ap} = K_{312}^{ap} = \frac{1}{3} E_b t_b^3 d^{-1} H^{-1}.$$

The vector $\mathbf{f}_p$ collects the reactive forces exerted by the adjacent cells on the passive nodes. The passive displacement and force vectors can be ordered and partitioned as $\mathbf{q}_p = (\mathbf{q}_p^-, \mathbf{q}_p^+)$, $\mathbf{f}_p = (\mathbf{f}_p^-, \mathbf{f}_p^+)$ to separate the variables $(\mathbf{q}_p^-, \mathbf{f}_p^-)$, related to the left/bottom sides of the cell boundary (composed by the external nodes 2, 3 shown in Figure 3.2c), from the variables $(\mathbf{q}_p^+, \mathbf{f}_p^+)$ related to the right/top sides (composed by the external nodes 4, 5). According to this decomposition, the dynamic (upper) part of the equation (3.1) can be written

$$\mathbf{M}\ddot{\mathbf{q}}_a + \mathbf{K}_{aa}\mathbf{q}_a + \mathbf{K}_{ap}^+ \mathbf{q}_p^+ + \mathbf{K}_{ap}^- \mathbf{q}_p^- = \mathbf{0}, \tag{3.5}$$

whereas the quasi-static (lower) part can be written

$$\begin{bmatrix} \mathbf{K}_{pa}^- \\ \mathbf{K}_{pa}^+ \end{bmatrix} \mathbf{q}_a + \begin{bmatrix} \mathbf{K}_{pp}^= & \mathbf{K}_{pp}^\mp \\ \mathbf{K}_{pp}^\pm & \mathbf{K}_{pp}^\# \end{bmatrix} \begin{pmatrix} \mathbf{q}_p^- \\ \mathbf{q}_p^+ \end{pmatrix} = \begin{pmatrix} \mathbf{f}_p^- \\ \mathbf{f}_p^+ \end{pmatrix}. \tag{3.6}$$

According to the Floquet-Bloch theory for bidimensional discrete model, the quasi-periodic conditions governing the propagation of planar wave can be imposed on the passive displacement/forces at the cell boundary, requiring

$$\mathbf{q}_p^+ = \mathbf{L}_k \mathbf{q}_p^-, \qquad \mathbf{f}_p^+ = -\mathbf{L}_k \mathbf{f}_p^-, \tag{3.7}$$

where $\mathbf{L}_k$ is a square *transfer* matrix that can be expressed in the diagonal block form

$$\mathbf{L}_k = \mathrm{diag}\left(e^{\imath k_1 H}\mathbf{I}, e^{\imath k_2 H}\mathbf{I}\right), \tag{3.8}$$

where $\mathbf{I}$ is the 3-by-3 identity matrix, while k_1 and k_2 are the two components of the wavevector $\mathbf{k} = (k_1, k_2)$, that is, the wavenumbers of the horizontally and vertically propagating waves, respectively.

The conditions (3.7) can be introduced in the quasi-static equation (3.6) to reduce the number of independent passive displacements. Therefore, the linear quasi-static laws

$$\mathbf{q}_p^- = \mathbf{R}_k \left(\mathbf{K}_{pa}^+ + \mathbf{L}_k \mathbf{K}_{pa}^-\right)\mathbf{q}_a, \qquad \mathbf{f}_p^- = \mathbf{K}_{pa}^- + \left(\mathbf{K}_{pp}^= + \mathbf{K}_{pa}^\mp \mathbf{L}_k\right)\mathbf{R}_k \left(\mathbf{K}_{pa}^+ + \mathbf{L}_k \mathbf{K}_{pa}^-\right)\mathbf{q}_a \tag{3.9}$$

govern the relations between the passive displacements or forces and the active degrees-of-freedom. The auxiliary block diagonal matrix $\mathbf{R}_k = -\left(\mathbf{L}_k \mathbf{K}_{pp}^\mp \mathbf{L}_k + \mathbf{L}_k \mathbf{K}_{pp}^= + \mathbf{K}_{pp}^\# \mathbf{L}_k + \mathbf{K}_{pp}^\pm\right)^{-1}$ is determined by the inversion of the non-singular sum between brackets.

Forcing the quasi-static relations (3.9) into the equation (3.5), the wave propagation through the material is fully governed in the configuration space of the active displacements by the equation of motion

$$\mathbf{M}\ddot{\mathbf{q}}_a + \mathbf{K}\mathbf{q}_a = \mathbf{0}, \tag{3.10}$$

where the $\mathbf{k}$-dependent Hermitian matrix $\mathbf{K} = \mathbf{K}_{aa} + \left(\mathbf{K}_{ap}^+ \mathbf{L}_k + \mathbf{K}_{ap}^-\right)\mathbf{R}_k \left(\mathbf{K}_{pa}^+ + \mathbf{L}_k \mathbf{K}_{pa}^-\right)$.

Denoting Ω the unknown circular frequency, the oscillatory solution $\mathbf{q}_a = \boldsymbol{\psi}_a \exp(\imath\Omega t)$ can be imposed. Therefore, eliminating the dependence on time, the in-plane wave propagation is governed by the linear eigenproblem

$$\left(\mathbf{K} - \Lambda\mathbf{M}\right)\boldsymbol{\psi}_a = \mathbf{0} \tag{3.11}$$

in the unknown eigenvalues $\Lambda = \Omega^2$ and eigenvectors $\boldsymbol{\psi}_a$. The eigensolution is composed by three eigenpairs, each made of a real-valued eigenvalue Λ_h and a complex-valued eigenvector $\boldsymbol{\psi}_h$ ($h = 1,2,3$). The eigenproblem (3.11) can be reformulated in the standard form

$$\left(\mathbf{H} - \Lambda\mathbf{I}\right)\boldsymbol{\varphi}_a = \mathbf{0}, \tag{3.12}$$

where the matrix $\mathbf{H} = \mathbf{Q}^{-T}\mathbf{K}\mathbf{Q}^{-1}$ and the auxiliary eigenvector $\boldsymbol{\varphi}_a = \mathbf{Q}\boldsymbol{\psi}_a$ are obtained by decomposing the mass matrix in the form $\mathbf{M} = \mathbf{Q}^T\mathbf{Q}$. The beam lattice model will be also referred to as *coarse* model in the following.

3.1.2. Microscopic first order continuum model

As alternative to the beam lattice model, the ring and the ligaments can be modeled at the microscopic scale in the framework of solid mechanics. Both the ring and the ligament bodies are modeled as first order continuum subject to Cauchy stresses induced by body forces $\mathbf{b}(\mathbf{x})$. A planar stress state is considered. Each material point is characterized by the displacement field $\mathbf{u}(\mathbf{x},t)$ and the partial differential equation governing the dynamic balance of a material point is

$$\nabla\cdot\boldsymbol{\sigma}(\mathbf{x}) + \mathbf{b}(\mathbf{x}) = \rho(\mathbf{x})\ddot{\mathbf{u}}(\mathbf{x},t), \tag{3.13}$$

where $\rho(\mathbf{x})$ is the mass density, $\ddot{\mathbf{u}}(\mathbf{x},t)$ is the acceleration of the material point. The stress tensor $\boldsymbol{\sigma}(\mathbf{x})$ can be related to the strain tensor $\boldsymbol{\varepsilon}(\mathbf{x})$ through the constitutive equation for linear elastic materials is

$$\boldsymbol{\sigma}(\mathbf{x}) = \mathbb{C}^m(\mathbf{x})\boldsymbol{\varepsilon}(\mathbf{x}), \tag{3.14}$$

where $\boldsymbol{\varepsilon}(\mathbf{x}) = \mathrm{sym}\nabla\mathbf{u}(\mathbf{x},t) = \frac{1}{2}[\nabla\mathbf{u}(\mathbf{x},t) + \nabla^T\mathbf{u}(\mathbf{x},t)]$ and $\mathbb{C}^m(\mathbf{x})$ is the fourth order elasticity tensor. Consistently with the beam lattice model, a locally isotropic material is assumed. By employing the constitutive equation (3.14), the dynamic equation (3.13) becomes

$$\nabla\cdot(\mathbb{C}^m(\mathbf{x})\mathrm{sym}\nabla\mathbf{u}(\mathbf{x},t)) + \mathbf{b}(\mathbf{x}) = \rho(\mathbf{x})\ddot{\mathbf{u}}(\mathbf{x},t), \tag{3.15}$$

where the $\mathbf{x}-$dependence of the elastic tensor and the mass density accounts for the material heterogeneities.

Transforming the equation (3.15) by applying the Fourier transform with respect to the time variable t, that is $\mathcal{F}[\mathbf{u}(\mathbf{x},\mathrm{t})] = \int_{-\infty}^{\infty}\mathbf{u}(\mathbf{x},\mathrm{t})\exp(-\imath\Omega t)dt = \hat{\mathbf{u}}(\mathbf{x})$, the governing equation in the transformed space (Christoffel equation) is

$$\nabla\cdot(\mathbb{C}^m(\mathbf{x})\mathrm{sym}\nabla\hat{\mathbf{u}}(\mathbf{x})) + \Omega^2\rho(\mathbf{x})\hat{\mathbf{u}}(\mathbf{x}) = \mathbf{0}, \tag{3.16}$$

which is identical to the equation of motion (3.15) if a time harmonic dependence $\mathbf{u}(\mathbf{x},t)=\hat{\mathbf{u}}(\mathbf{x})\exp(-\imath\Omega t)$ is assumed. According to the Floquet-Bloch theory for a bidimensional continuous model, the quasi-periodic conditions

$$\hat{\mathbf{u}}^{+}=e^{\imath\mathbf{k}\cdot H}\hat{\mathbf{u}}^{-}, \qquad \hat{\boldsymbol{\sigma}}^{+}\mathbf{n}^{+}=-e^{\imath\mathbf{k}\cdot H}\hat{\boldsymbol{\sigma}}^{-}\mathbf{n}^{-}, \tag{3.17}$$

where $\mathbf{k}$ is the wavevector and $\mathbf{n}$ is the outward normal unit vector ($\mathbf{n}^{+}$ and $\mathbf{n}^{-}$ are defined, analogously to beam lattice model, on the right/top and on the left/bottom edges, respectively). The Floquet–Bloch problem arising from the equation (3.16) and the boundary conditions (3.17) is solved numerically via a Finite Element model (COMSOL Multiphysics). Bidimensional triangular elements (with quadratic Lagrangian interpolation functions) are adopted to discretize the domain. The MUltifrontal Massively Parallel sparse direct Solver (MUMPS), based on the LU decomposition method, is used. A proper mesh refinement has been required to satisfy convergence criteria focused on the highest frequency branches of interest in the dispersion spectrum. The microscopic first order continuum model will be also referred to as *fine* model in the following.

3.1.3. Homogenized micropolar continuum model

The continuous displacement fields of a micropolar continuum model (Bacigalupo and Gambarotta, 2016, 2017a, 2017b) are $\mathbf{v}(\mathbf{x},t)$ and $\theta(\mathbf{x},t)$ that represent, respectively, the macro-displacement and the micropolar rotation of the reference cell located at $\mathbf{x}$ at the time t. The partial differential equations of motion are

$$\begin{aligned} &\nabla\cdot\mathbf{T}=\rho\ddot{\mathbf{v}}\\ &\nabla\cdot\mathbf{m}-\in_{3jh}\left(\mathbf{e}_j\otimes\mathbf{e}_h\right):\mathbf{T}=\eta\ddot{\theta}, \qquad j,h=1,2 \end{aligned} \tag{3.18}$$

where ρ is the mass density of the equivalent homogeneous continuum, η is the density of rotational inertia, $\mathbf{T}$ is the asymmetric macro-stress tensor, $\mathbf{m}$ is the couple-stress vector of the equivalent continuum and $\in_{3jh}$ is the Levi Civita symbol.

By introducing the curvature $\boldsymbol{\chi}=\nabla\theta$ and the micropolar asymmetric strain tensor $\boldsymbol{\Gamma}=\nabla\mathbf{v}-\mathbf{W}(\theta)$, where $\nabla\mathbf{v}$ is the displacement gradient and the macro-rotation micropolar tensor $\mathbf{W}$ is defined as $\mathbf{W}=w_{jh}\mathbf{e}_j\otimes\mathbf{e}_h=-\in_{3jh}\theta\mathbf{e}_j\otimes\mathbf{e}_h$, the constitutive relations of micropolar elastic continuum are

$$\begin{aligned} \mathbf{T}&=\mathbb{E}_s\boldsymbol{\Gamma}+\mathbb{Y}_s\boldsymbol{\chi}\\ \mathbf{m}&=\mathbb{Y}_s^{T}\boldsymbol{\Gamma}+\mathbf{E}_s\boldsymbol{\chi}, \end{aligned} \tag{3.19}$$

where $\mathbb{E}_s$, $\mathbb{Y}_s$ and $\mathbf{E}_s$ are, respectively, the fourth, third and second order elasticity tensors of the equivalent homogeneous continuum. By employing the constitutive equations (3.19), the equations of motion become

$$\begin{aligned} &\nabla\cdot(\mathbb{E}_s\boldsymbol{\Gamma}+\mathbb{Y}_s\boldsymbol{\chi})=\rho\ddot{\mathbf{v}}\\ &\nabla\cdot(\mathbb{Y}_s^{T}\boldsymbol{\Gamma}+\mathbf{E}_s\boldsymbol{\chi})-\in_{3jh}\left(\mathbf{e}_j\otimes\mathbf{e}_h\right):(\mathbb{E}_s\boldsymbol{\Gamma}+\mathbb{Y}_s\boldsymbol{\chi})=\eta\ddot{\theta}, \qquad j,h=1,2 \end{aligned} \tag{3.20}$$

In case of centrosymmetric lattices, the third order elasticity tensor $\mathbb{Y}_s$ is identically null and the equations (3.20) can be written in the index form

$$\begin{aligned} &\left[E_{ijhk}\left(v_{h,k}+\in_{3hk}\theta\right)\right]_{,j}=\rho\ddot{v}_i \\ &\left(E_{ij}\theta_{,j}\right)_{,i}-\in_{3jh}E_{jhrs}\left(v_{r,s}+\in_{3rs}\theta\right)=\eta\ddot{\theta}, \qquad i,j,h,k,r,s=1,2 \end{aligned} \tag{3.21}$$

where the elastic constants E_{ijhk} and E_{ij} can be obtained through a high frequency dynamic homogenization similar to that proposed in (Reda et al., 2017).

By applying to the equation (3.20) the Fourier transform with respect to the time variable t or by considering the harmonic motion $\mathbf{v}=\hat{\mathbf{v}}\exp[\imath(\mathbf{k}\cdot\mathbf{x}-\Omega t)]$ and $\theta=\hat{\theta}\exp[\imath(\mathbf{k}\cdot\mathbf{x}-\Omega t)]$, the governing equation in the transformed space (Christoffel equation) is

$$\mathbf{C}_{Hom}(\mathbf{k},\Omega)\hat{\mathbf{V}}=\mathbf{0}, \tag{3.22}$$

where $\hat{\mathbf{V}}=[\hat{\mathbf{v}}^T,\hat{\theta}]$ is the polarization vector collecting $\hat{\mathbf{v}}$ and $\hat{\theta}$. In case of centrosymmetric lattices, the equation (3.22) can be written in the index form

$$\begin{aligned} &E_{ijhk}\left(k_jk_k\hat{v}_h-\in_{3hk}\mathrm{i}k_j\hat{\theta}\right)-\rho\,\Omega^2\hat{v}_i=0 \\ &E_{ij}k_ik_j\hat{\theta}+\in_{3jh}E_{jhrs}\left(\mathrm{i}k_s\hat{v}_r+\in_{3rs}\hat{\theta}\right)-\eta\,\Omega^2\hat{\theta}=0, \qquad i,j,h,k,r,s=1,2 \end{aligned} \tag{3.23}$$

The second order expansion of the matrix of the micropolar model $\mathbf{C}_{Hom}(\mathbf{k},\Omega)$ in the wavevector $\mathbf{k}$ can be demonstrated to correspond to an approximation of the corresponding one from the discrete system $\mathbf{C}_{Lag}(\mathbf{k},\Omega)$ (Bacigalupo and Gambarotta, 2016, 2017a, 2017b)

$$\mathbf{C}_{Lag}(\mathbf{k},\Omega)=A_{cell}\mathbf{C}_{Hom}(\mathbf{k},\Omega)+\mathrm{O}\left(|\mathbf{k}|^3\right), \tag{3.24}$$

where, considering the eigenvalue problem of the beam lattice model (3.11), the matrix of the discrete system is $\mathbf{C}_{Lag}(\mathbf{k},\Omega)=\mathbf{K}-\Lambda\mathbf{M}$ and A_{cell} is the area of the periodic cell. The homogenized micropolar continuum model will be also referred to as *homogenized* model in the following.

These problems can be also studied through dynamic variational-asymptotic and non-local asymptotic homogenization, high contrast asymptotic homogenization and high frequency homogenization techniques (Smyshlyaev and Cherednichenko, 2000; Babych et al., 2008; Smyshlyaev, 2009; Craster at al., 2010; Amosov et al., 2013; Bacigalupo and Gambarotta 2014b; De Bellis et al., 2019; Del Toro et al., 2019).

3.2. Wave propagation

3.2.1. Dispersion spectrum

The $\mathbf{k}$-dependent solution of the eigenproblem (3.11) gives the dispersion relations $\Omega_h(\mathbf{k})$ characterizing the coarse model (h=1…3). Alternatively, $\mathbf{k}$-dependent solution of the Christoffel equation (3.16) coupled with the conditions (3.14) gives the dispersion relations $\Omega_h(\mathbf{k})$ characterizing the fine model ($h \in \mathbb{N}$). The dispersion surfaces are obtained letting the wavevector $\mathbf{k}$ vary in the entire *first Brillouin zone*, corresponding to the square domain $\mathcal{D}^H = [-\pi/H, \pi/H] \times [-\pi/H, \pi/H]$. The dispersion functions $\Omega_h(\Xi)$ can be defined by introducing a curvilinear abscissa Ξ spanning the closed boundary $\partial\mathcal{B}_1^H$ of the triangular subdomain $\mathcal{B}_1^H$. The corresponding curves obtained under variation of the abscissa Ξ over the entire range $[0, (2\pi + \sqrt{2}\pi)/H]$ characterize the dispersion spectrum of one or the other models. The numerical solution for the fine model has been based on a sufficiently fine discretization of the finite element model, selected after a proper convergence analysis. Moreover, the triangular boundary $\partial\mathcal{B}_1^H$ has been divided in one hundred equidistant Ξ-points to obtain a sufficient resolution in the dispersion curves. Furthermore, the exact solution of the eigenproblem (3.11) has been approximated with the solution of the Christoffel equation (3.22) related to the homogenized model. In particular, it can be demonstrated that the dispersion curves of the homogenized model coincide with those of the coarse model, if a second-order Taylor $\mathbf{k}$-expansion (centered in $\mathbf{k} = \mathbf{0}$) of the $\mathbf{K}$ – matrix is performed (Bacigalupo and Gambarotta, 2017a).

Introducing the non-dimensional wavevector $\tilde{\mathbf{k}} = (\tilde{k}_1, \tilde{k}_2)$ where $\tilde{k}_1 = k_1 H$ and $\tilde{k}_2 = k_2 H$, a comparison between the dispersion spectra of the fine and coarse models (Figure 3.3) and between the fine and homogenized models (Figure 3.4a) is shown. The comparison is carried out in non-dimensional form by introducing the dispersion functions $\omega_h(\xi)$ relating the non-dimensional variables

$$\omega = \frac{\Omega}{\Omega_c}, \quad \xi = \Xi H, \tag{3.25}$$

where $\Omega_c^2 = E_b (\rho_r H^2)^{-1}$ is a reference frequency that can be set to be unitary without loss of generality. The independent variable ξ varies in the range $[0, 2\pi + \sqrt{2}\pi]$ and represents the curvilinear abscissa spanning the boundary $\partial\mathcal{B}_1$ of the triangular subdomain $\mathcal{B}_1$ of the non-dimensional domain $\mathcal{D} = [-\pi, \pi] \times [-\pi, \pi]$ of the *first Brillouin zone*.

The good matching covers all the boundary $\partial\mathcal{B}_1$ in the comparison between the coarse and the fine models for different values of the non-dimensional parameter t_b / H, accounting for the ligament slenderness (Figure 3.3). In particular, a good agreement is obtained in the gray region around the red dispersion curve with the highest-frequency, corresponding to different effective lengths of the ligaments $L_e = \alpha L_b$ in the beam lattice model. The gray region is the envelope of the dispersion curves obtained for the multiplier α varying in the range $[0.78, 0.85]$ for the Figure 3.3a and in the range $[0.88, 0.95]$ for the Figure 3.3b. Differently, the homogenized model is found to well-approximate the dispersion spectrum of the fine model along the boundary of a subdomain of the triangular $\mathcal{B}_1$ zone (Figure 3.4a).

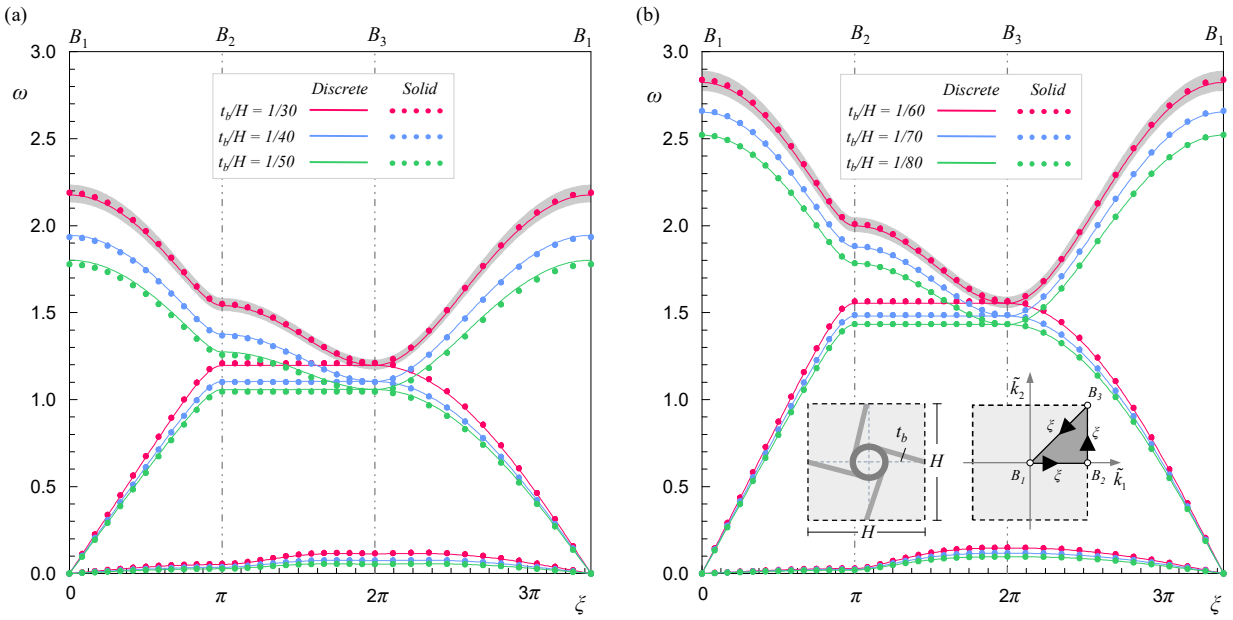

Figure 3.3 Comparison between the dispersion spectra characterizing the coarse (Discrete) and the fine (Solid) model of the tetrachiral material (with $t_r / t_b = 5$) for different values of the ligament slenderness t_b / H: (a) $R / H = 1/5$, (b) $R / H = 1/10$.

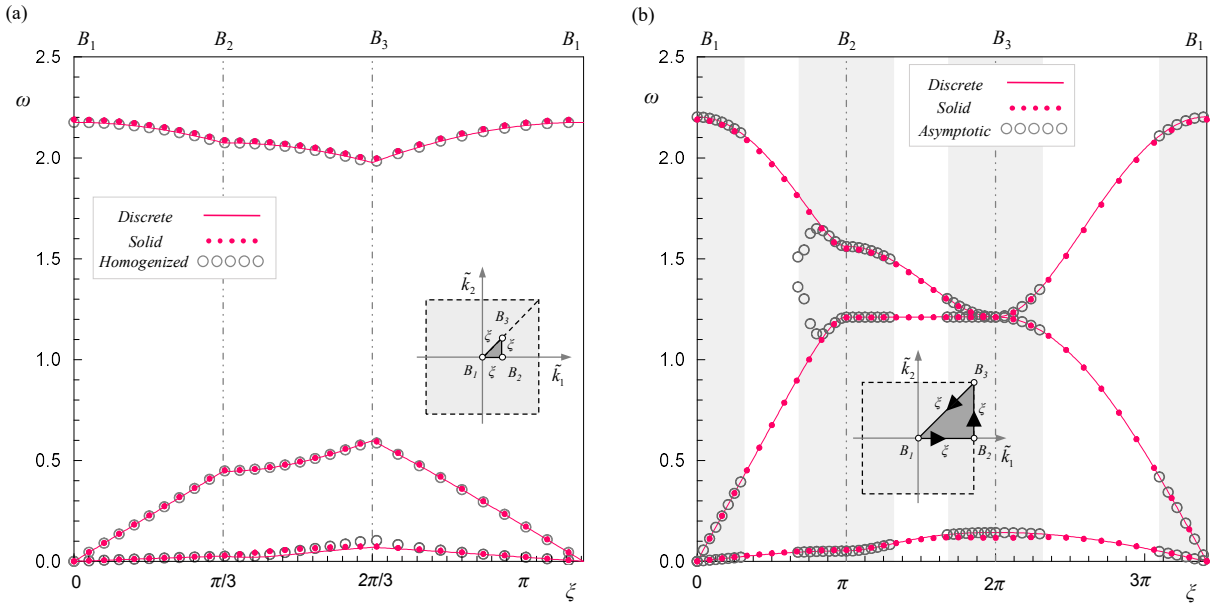

Figure 3.4 Dispersion spectra for the tetrachiral material ($t_b / H = 1/30$, $t_r / t_b = 5$, $R / H = 1/5$): (a) Comparison among the coarse (Discrete), fine (Solid) and homogenized models, (b) Comparison between the fine (Solid) model and the exact and asymptotically approximate solutions for the coarse (Discrete) model.

3.2.2. Perturbation solution

Within the framework of beam lattice models, the step-by-step construction of the dispersion surfaces $\Omega_h(\mathbf{k})$ rapidly can demand excessive computational resources as the model dimension increases and the

$\partial\mathscr{B}_1^H$-discretization becomes finer. Therefore, perturbation methods can represent an efficient alternative to the numerical solution of the eigenproblem governing the wave dispersion. Each eigenvalue $\Lambda_h(\mathbf{k}) = \Omega_h^2(\mathbf{k})$ satisfying the eigenproblem (3.12) can be regarded as one of the zeroes (with multiplicity m_h) of the characteristic function $Q(\Lambda, \mathbf{k}) = \det(\mathbf{H}(\mathbf{k}) - \Lambda\mathbf{I})$ in the domain of positive real Λ-values. Therefore, fixing the set $\mathbf{p}^*$ of the microstructural parameters describing the periodic cell, each dispersion surface can be determined by individually following a certain zero of the characteristic function, under variation of the wavevector $\mathbf{k}$ in the square Brillouin domain.

Within this mathematical context, perturbation techniques furnish analytical – although asymptotically approximate – expressions of the dispersion functions. Naturally, the availability of explicit functions $\Lambda_h(\mathbf{k})$ may reduce the algorithmic effort required by numerical continuation traditionally applied to the solutions of the characteristic equation $Q(\Lambda, \mathbf{k}) = 0$. A perturbation technique starts with the selection of a reference (unperturbed) wavevector $\mathbf{k}^*$ in the $\mathscr{B}_1^H$-domain. The corresponding reference eigenvalues Λ^* of the matrix $\mathbf{H}^* = \mathbf{H}(\mathbf{k}^*)$ are assumed to be exactly (analytically or numerically) known. Even if not mandatory, a convenient selection of the reference wavevector $\mathbf{k}^*$ could be preferable to enhance the effectiveness and the validity of the asymptotic approximation (Lepidi, 2013; Luongo and Ferretti, 2015; Bacigalupo and Lepidi, 2016). For instance, the typical choice $\mathbf{k}^* = \mathbf{0}$ often allows the analytical assessment of all the reference eigenvalues Λ^* satisfying the characteristic equation $Q(\Lambda, \mathbf{k}^*) = 0$. In the most general case, perturbation techniques can readily treat multi-variable perturbations. Indeed, small-amplitude two-parameter perturbations $\varepsilon\mathbf{k}' = \mathbf{k} - \mathbf{k}^*$ can be considered to span all the directions of the bidimensional $\mathscr{B}_1^H$-domain in the neighborhood of $\mathbf{k}^*$ (since $\varepsilon << 1$ represents an auxiliary non-dimensional parameter regulating the perturbation smallness).

Exploring the monodimensional boundary $\partial\mathscr{B}_1$, spanned by the non-dimensional abscissa ξ, may be sufficient. Consequently, the unperturbed reference point in the boundary $\partial\mathscr{B}_1$ can be identified by the particular abscissa ξ^*, and the ξ^*-neighborhood can be explored by the local coordinate $z = \xi - \xi^*$. Thus – within the limits of the boundary $\partial\mathscr{B}_1$ – the change-of-variable $\xi = \xi^* + z$ allows to express the non-dimensional characteristic function in the form $F(\lambda, z)$, where the z-variable acts as single perturbation parameter (under the assumption $z << 1$) and $\lambda = \omega^2$ is the non-dimensional eigenvalue.

Under the assumption of sufficient regularity of the dispersion functions, each exact eigenvalue can tentatively be approximated by a series function $\lambda(z)$ of integer z-powers

$$\lambda(z) = \lambda^* + \sum_n \lambda^{(n)} z^{(n)} = \lambda^* + \dot{\lambda} z + \ddot{\lambda} z^2 + ... + \lambda^{(n)} z^{(n)} + ..., \tag{3.26}$$

where the coefficient $\lambda^{(n)}$ (multiplied by the factorial *n*!) are known as the *eigensensitivities* (with respect to the perturbation z) of the eigenvalues, and can also be regarded as the *unknown n*-th z-derivative (evaluated at $z = 0$) of the exact but implicit eigenvalue function $F(\lambda, z) = 0$.

Once the series $\lambda(z)$ has been established, the characteristic function becomes a composite single-variable function $G(z) = F(\lambda(z), z)$, which admits the Taylor expansion in z-powers

$$G(z) = G^* + \sum_n \frac{G^{(n)}}{n!} z^{(n)} = G^* + \dot{G}z + \frac{\ddot{G}}{2} z^2 + ... + \frac{G^{(n)}}{n!} z^{(n)} + ..., \tag{3.27}$$

where $G^* = F(\lambda^*, 0)$ is certainly null, as far as λ^* is known through the relation $\lambda^* = \Lambda^* / \Omega_c^2$ where Λ^* belongs to the $\mathbf{H}^*$-eigenspectrum by hypothesis. The generic higher-order coefficient $G^{(n)}$ can be recognized as the *n*-th z-derivative (evaluated at $z = 0$) of the function $G(z)$. In general, these derivatives require the recursive application of the chain rule for the differentiation of single-variable composite functions.

Each series coefficient $G^{(n)}$ is a complete *n*-degree polynomial of all the unknown coefficients of the eigenvalue expansion (3.22) up to $\lambda^{(n)}$. The $G^{(n)}$-coefficients multiplying the lowest z-powers are

$$z^1: \quad \dot{G} = \dot{\lambda} F^{(1,0)} + F^{(0,1)} \tag{3.28}$$

$$z^2: \quad \ddot{G} = 2\ddot{\lambda} F^{(1,0)} + (\dot{\lambda})^2 F^{(2,0)} + 2\dot{\lambda} F^{(1,1)} + F^{(0,2)}, \tag{3.29}$$

where the synthetic notation $F^{(h,k)} = \partial_\lambda^h \partial_z^k F(\lambda, z)$ has been adopted for the partial derivatives of the characteristic function $F(\lambda, z)$, and evaluation at $(\lambda = \lambda^*, z = 0)$ is understood. A recursive form of the generic *n*-th coefficient, multiplying the z^n-power, can be found in (Bacigalupo and Lepidi, 2016; Lepidi and Bacigalupo, 2018).

The characteristic equation $G(z) = F(\lambda(z), z) = 0$ is asymptotically satisfied by zeroing each z^n-order coefficient $G^{(n)}$. Thus, a chain of *n* ordered equations (*perturbation equations*) is generated, where the eigensensitivities $\lambda^{(n)}$ are the unknowns to be determined. Starting with the zeroth-order solution, given by the known eigenvalues λ^* (*generating solution*), each perturbation equation of the chain involves a single unknown, that is, one of the higher-order coefficients. Depending on the algebraic multiplicity m^* of the generic λ^*-eigenvalue, two fundamental cases occur

- Simple eigenvalue: if λ^* is a simple root (algebraic multiplicity $m^* = 1$) for the equation $G(0) = F(\lambda^*, 0) = 0$, then the coefficient $F^{(1,0)} \neq 0$. Hence, the z^1- order equation (3.27) is linear in the unknown $\dot{\lambda}$, the z^2- order equation (3.28) is linear in the unknown $\ddot{\lambda}$, and so on. Therefore, the cascade solutions (null if the numerator vanishes) for the lowest order equations are

$$z^1: \quad \dot{\lambda} = -\frac{F^{(0,1)}}{F^{(1,0)}} \tag{3.30}$$

$$z^2: \quad \ddot{\lambda} = -\frac{(\dot{\lambda})^2 F^{(2,0)} + 2\dot{\lambda} F^{(1,1)} + F^{(0,2)}}{2F^{(1,0)}}, \tag{3.31}$$

  and, by extension, the z^n- order equation allows the determination of the *n*-th coefficient $\lambda^{(n)}$. A recursive form of the *n*-th coefficient $\lambda^{(n)}$ can be found in (Bacigalupo and Lepidi, 2016; Lepidi and Bacigalupo, 2018).

- *Double (semi-simple) eigenvalue*: if λ^* is a double root (algebraic and geometric multiplicity $m^* = 2$) for the equation $G(0) = F(\lambda^*, 0) = 0$, then the coefficient $F^{(1,0)} = 0$, but $F^{(2,0)} \neq 0$. Since λ^* must be non-defective (semi-simple), it can be proved that $F^{(0,1)} = 0$. Consequently,

the z^1-order equation (3.27) is trivially satisfied, but leaves $\dot{\lambda}$ undetermined. Such an indetermination is cleared by the z^2- order equation (3.28), which is a quadratic in the $\dot{\lambda}$-unknown only, since the null multiplier $F^{(1,0)}$ affects the other unknown $\ddot{\lambda}$. Thus, the lowest order equations give

$$z^1: \quad \dot{\lambda} \text{ is undetermined} \tag{3.32}$$

$$z^2: \quad \dot{\lambda}_{\pm} = -\frac{F^{(1,1)} \pm \sqrt{(F^{(1,1)})^2 - F^{(2,0)}F^{(0,2)}}}{F^{(2,0)}}, \tag{3.33}$$

where the pair $\dot{\lambda}_{\pm}$ splits the double root λ^* in two distinct eigenvalues $\lambda^* + z\dot{\lambda}_{\pm} + O(z^2)$. If the radical vanishes, in consequence of the particular sub-case $(F^{(1,1)})^2 = F^{(2,0)}F^{(0,2)}$, the splitting of the double root is postponed to higher-orders. In the general case, the higher unknowns $\lambda_{\pm}^{(n)}$ are determined by linear z^{n+1}-order equations, solved for one or the other of the $\dot{\lambda}_{\pm}$-values.

When the perturbation technique is applied to approximate the band structure of the tetrachiral material, the three vertices B_1 (corresponding to $\xi^* = 0$ or $\tilde{\mathbf{k}}^* = \mathbf{k}^* H = (0,0)$), B_2 (corresponding to $\xi^* = \pi$ or $\tilde{\mathbf{k}}^* = \mathbf{k}^* H = (\pi,0)$) and B_3 (corresponding to $\xi^* = 2\pi$ or $\tilde{\mathbf{k}}^* = \mathbf{k}^* H = (\pi,\pi)$) of the triangular boundary $\partial\mathscr{B}_1$ have been employed as reference points to start the perturbation analysis. The fourth-order asymptotic approximation of the dispersion curves are represented by the black circles in Figure 3.4. The comparison with the exact solutions obtained from the discrete model (red lines) and the solid model (red dots) shows a fine agreement over large extents of the boundary $\partial\mathscr{B}_1$, centered at the three reference points. Coherently with the intrinsic nature of the perturbation solutions, the approximation accuracy tends to decay with the distance from the reference point. However, a satisfying accuracy can be observed to persist up to z-values close or even greater than unity (the gray zones), that is, beyond the limits of the smallness assumption ($z << 1$).

Table 3.1 Fixed and free parametric values in the cases of the parametric analysis.

	t_b / H	t_r / t_b	R / H	ρ_i / ρ_r	ρ_b / ρ_r	E_{b1} / E_{b2}
Reference Case	[1/100, 1/10]	[1,3]	[1/10, 1/3]	0	0	1
Case 1	1/20	3	1/3	[1, 100]	0	1
Case 2	1/20	3	1/3	0	[1/10, 30]	1
Case 3	1/20	3	1/3	[1, 100]	[1/10, 30]	1
Case 4	1/20	3	1/3	[1/10, 30]	0	[1, 30]
Case 5	1/20	3	1/3	[1,10]	[1, 10]	[1, 30]

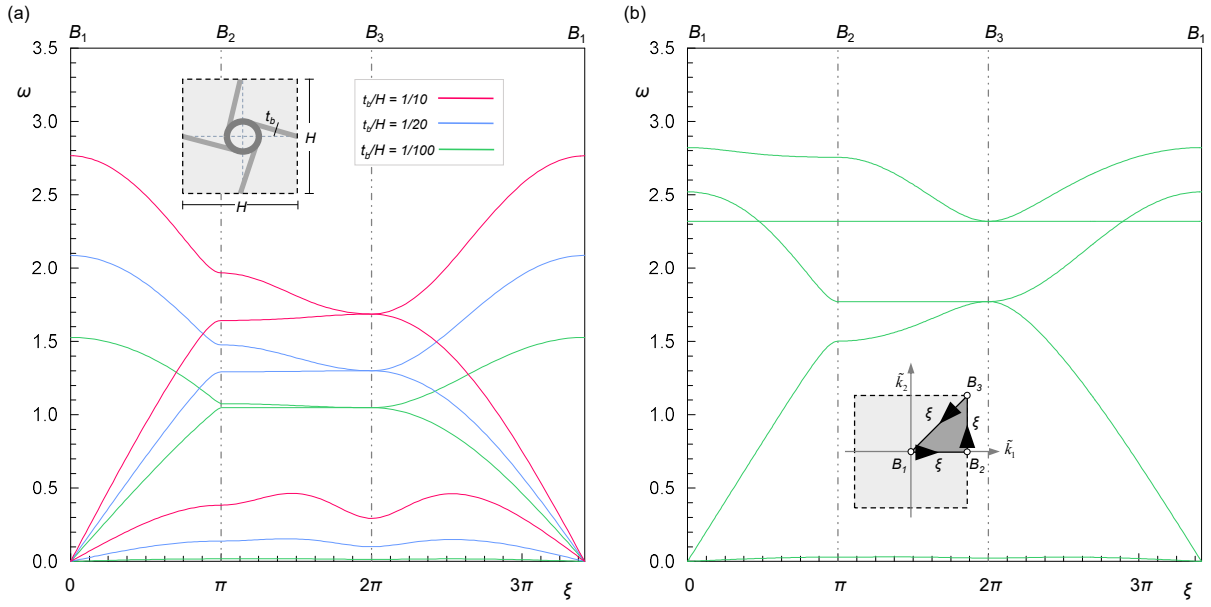

Figure 3.5 Reference Case. Dispersion spectrum with the parameters (a) $R/H = 1/3$, $t_r/t_b = 3$ and t_b/H variable, (b) $R/H = 1/3$, $t_r/t_b = 1$ and $t_b/H = 1/100$.

3.3. Parametric analysis

The parametric analyses are run to evaluate the effects of the variations in the mechanical and geometric parameters on the acoustic and optic surfaces of the Floquet-Bloch spectrum. Given the good agreement obtained by the comparison of the dispersion spectrum of the different models, the analyses are performed using the finite element solution of the fine Cauchy model that is easier to handle and suited to deal with a greater variety of cases. The tetrachiral material selected as reference for the parametric analysis is characterized by empty ring and massless ligaments with same elastic properties.

Some preliminary analyses are carried out by varying the independent non-dimensional geometric parameters

$$\frac{t_b}{H}, \quad \frac{t_r}{t_b}, \quad \frac{R}{H}, \tag{3.34}$$

that depend on the ring radius (associated to the chirality) and on the width of the ligaments and the ring.

Increasing the width of the ligaments, the frequencies grow up in all investigation range and the distance between the optic and the acoustic surfaces increases creating a partial band gap with growing amplitude in the interval $0 \le \xi \le \pi$ (Figure 3.5). Instead, increasing the radius or the width of the ring the frequencies decrease. When the width of the ring is small and therefore the ring is thin and flexible, an enrichment of the dispersion spectrum, in the low-frequency range, with new dispersion surfaces associated to ring-deforming waveforms can be observed (Figure 3.5b). In this case, the hypothesis of rigid body used in the beam lattice model loses validity (Vadalà et al., 2018).

These analyses highlight some issues in satisfying the conditions of the existence of a full band gap in the low-frequency range. These conditions are investigated numerically and determined in analytical form asymptotically as an inequality between the inertial characteristics of the ring and the slenderness of the ligaments. The physical realization of these conditions would require a technical arrangement like a material with functionally-graded elastic properties with tapered cross section or other modifications that destroy the invariant properties in the out-of-plane direction. It is possible to achieve a band gap at a target frequency using metamaterials with inertial resonators.

The possibility of obtaining the same result is analyzed either by enlarging the parameter space or by removing some simplifying hypotheses of the reference model. The frequency corresponding to the vertex B_2 of the triangular boundary $\partial\mathscr{B}_1$, where the second acoustic surface and the first optical surface collide given rise to a point with a double frequency, is chosen as target center frequency. The independent non-dimensional parameters considered for these parametric analyses are

$$\frac{\rho_i}{\rho_r},\ \frac{\rho_b}{\rho_r},\ \frac{E_{b1}}{E_{b2}}, \tag{3.35}$$

where the parameter ρ_i / ρ_r represents the mass density ratio between an intra-ring filler and the ring material, ρ_b / ρ_r is the mass density ratio between the ligament and the ring material and the parameter E_{b1} / E_{b2} is the ratio between the Young's Moduli of two ligaments made of different materials. The analysis cases and the parameter range variations are summarized in Table 3.1.

The dispersion spectrum of the reference case for parameter values of $t_b / H = 1/20$, $t_r / t_b = 3$, $R / H = 1/3$ corresponds to the light blue curves in Figure 3.5. For the subsequent cases analyzed, the values of the parameters (3.34) are fixed as in the reference case.

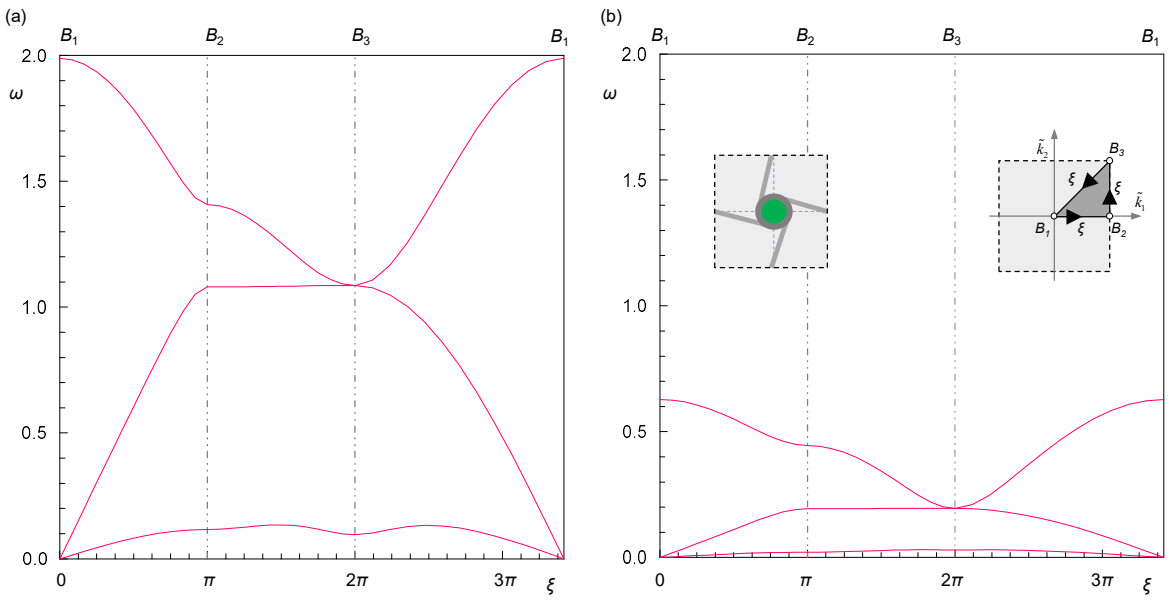

Figure 3.6 Case 1. Dispersion spectrum with the parameter (a) $\rho_i / \rho_r = 1$, (b) $\rho_i / \rho_r = 100$.

In the case 1 the ring of the tetrachiral material is filled with an intra-ring heavy filler having density ρ_i. The parameters ρ_b / ρ_r and E_{b1} / E_{b2} are fixed and the ratio ρ_i / ρ_r changes in the range reported in Table 3.1. Increasing the density ratio, the frequencies decrease and the distance between the optical and the acoustic branches is reduced, except in $\xi = 2\pi$ where the acoustic and the optical frequencies coincide. (Figure 3.6).

In the case 2 the tetrachiral material has the massive ligaments (Brun et al., 2013) and an empty ring. The parameters ρ_i / ρ_r and E_{b1} / E_{b2} are fixed and the ratio ρ_b / ρ_r changes in the range reported in Table 3.1. Increasing the mass density of the ligaments, the frequencies decrease and an enrichment of the dispersion spectrum with more dispersion optic curves in the low- frequency range is observed (Figure

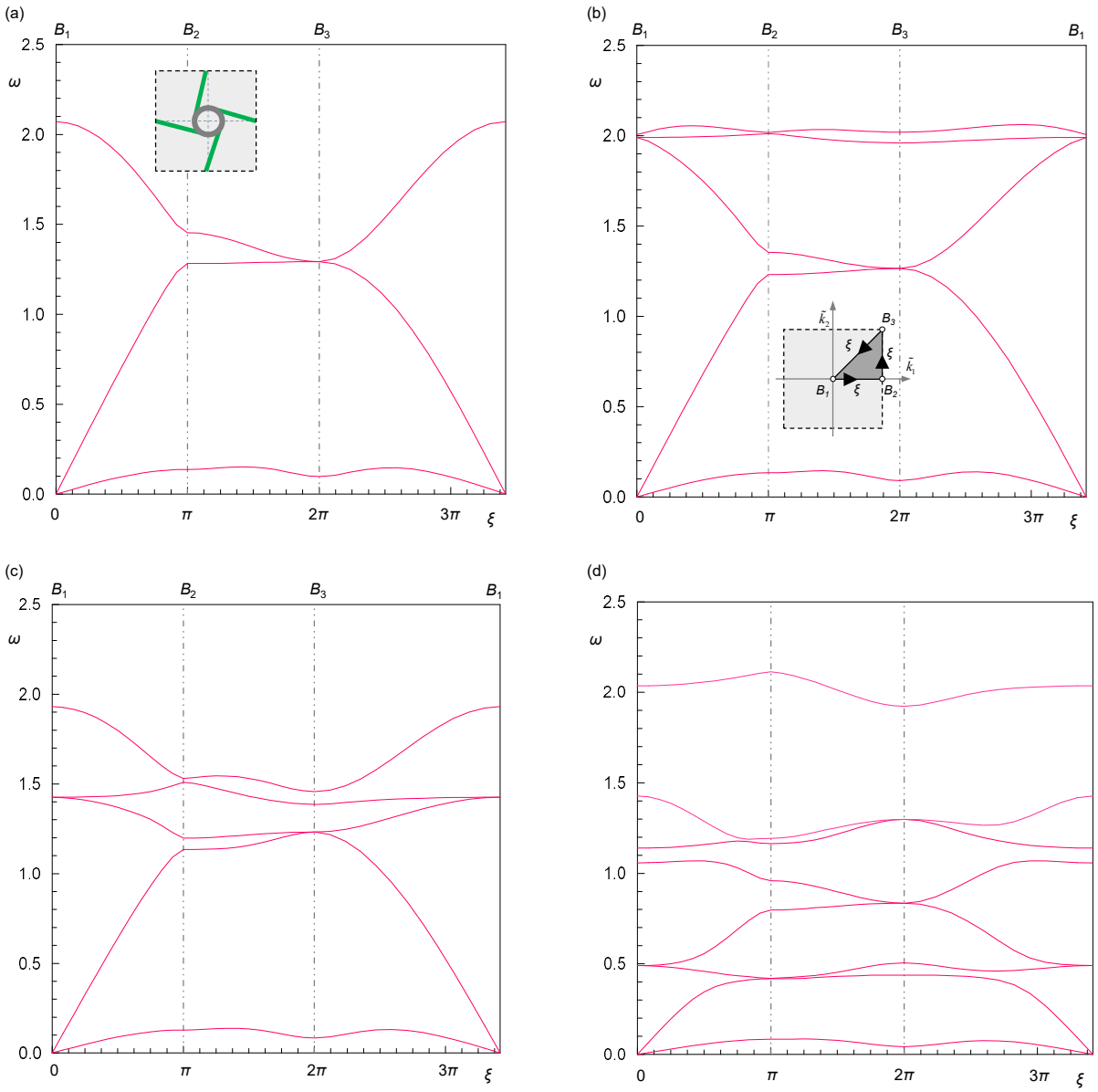

Figure 3.7 Case 2. Dispersion spectrum with the parameter (a) $\rho_b / \rho_r = 1/10$, (b) $\rho_b / \rho_r = 1/2$, (c) $\rho_b / \rho_r = 1$, d) $\rho_b / \rho_r = 10$.

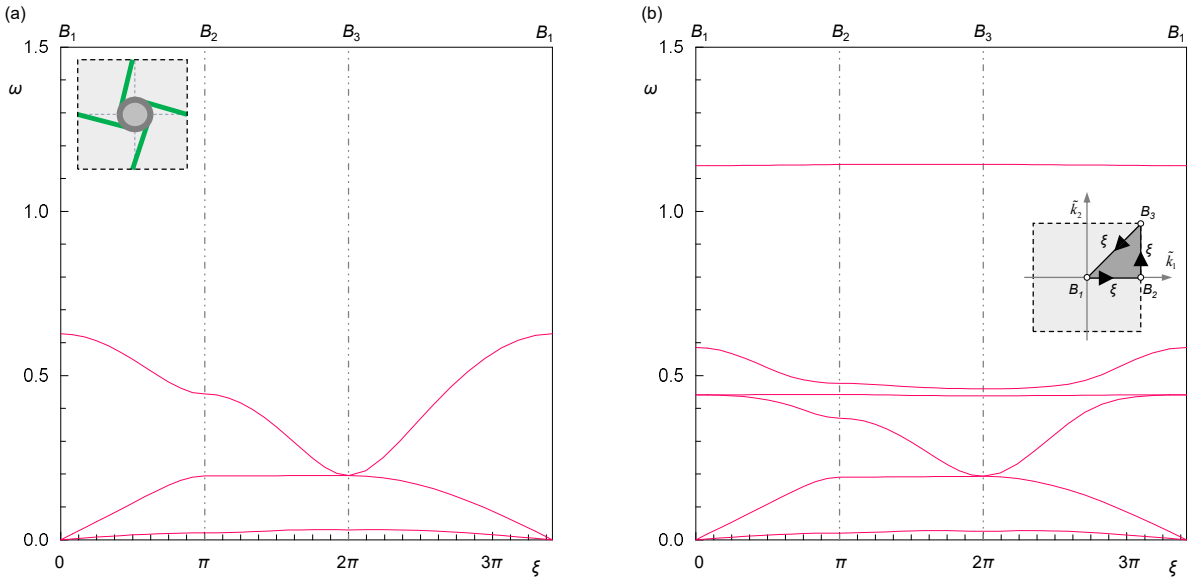

Figure 3.8 Case 3. Dispersion spectrum with the parameter (a) $\rho_b / \rho_r = 1/10$, (b) $\rho_b / \rho_r = 10$.

3.7). These new curves are related to local waveforms, essentially partecipated by the ligaments dynamics. In Figure 3.7a the local waveforms have higher frequencies and do not interact with the low-frequency branches. Increasing the ratio between the material densities, there is a stronger interaction with both acoustic and the optical branches. Furthermore, a total band gap can be observed between the curves 7 and 8 for $\rho_b / \rho_r = 10$ (Figure 3.7d).

In the case 3 the cell composed by a filled ring and the massive ligaments is analyzed. The parameter E_{b1} / E_{b2} is fixed and the ratios ρ_i / ρ_r and ρ_b / ρ_r change in the ranges reported in Table 3.1. Increasing the intra-ring filler mass density the frequencies decrease. Fixing the parameter $\rho_i / \rho_r = 100$, for small values of the density ratio ρ_b / ρ_r, the dispersion curves do not present negligible changes, as shown in Figure 3.8a. By increasing the mass density of the ligaments, the frequencies decrease and an enrichment of the dispersion spectrum with more dispersion branches related to the local waveforms in the low-frequency range is observed (Figure 3.8b). The interaction between these new curves and the other turns out to open full band gaps (Figure 3.8b).

In the case 4 the tetrachiral material has an intra-ring heavy filler, two ligaments (blue ligaments in the Figure 3.9) with Young's Modulus equal to E_{b1} and the other ligaments (grey ligaments in Figure 3.9) with Young's Modulus equal to E_{b2}. The ratio ρ_b / ρ_r is fixed and the parameters ρ_i / ρ_r and E_{b1} / E_{b2} change in the ranges reported in Table 3.1. Two different cells with inhomogeneous ligaments are analyzed and for both, increasing the parameter ρ_i / ρ_r the frequencies of the dispersion curves decrease. From the comparison between Figure 3.9a and Figure 3.6a obtaied for $\rho_i / \rho_r = 1$, the frequencies of the non-centrosymmetric cell are higher, even if the curves shape is similar. In Figure 3.9b a partial band gap can be observed. Since the $\partial\mathcal{B}_1$ boundary does not include all the *irreducible Brillouin zone*, it can be concluded that the stop band affects the wave propagating along the diagonal direction.

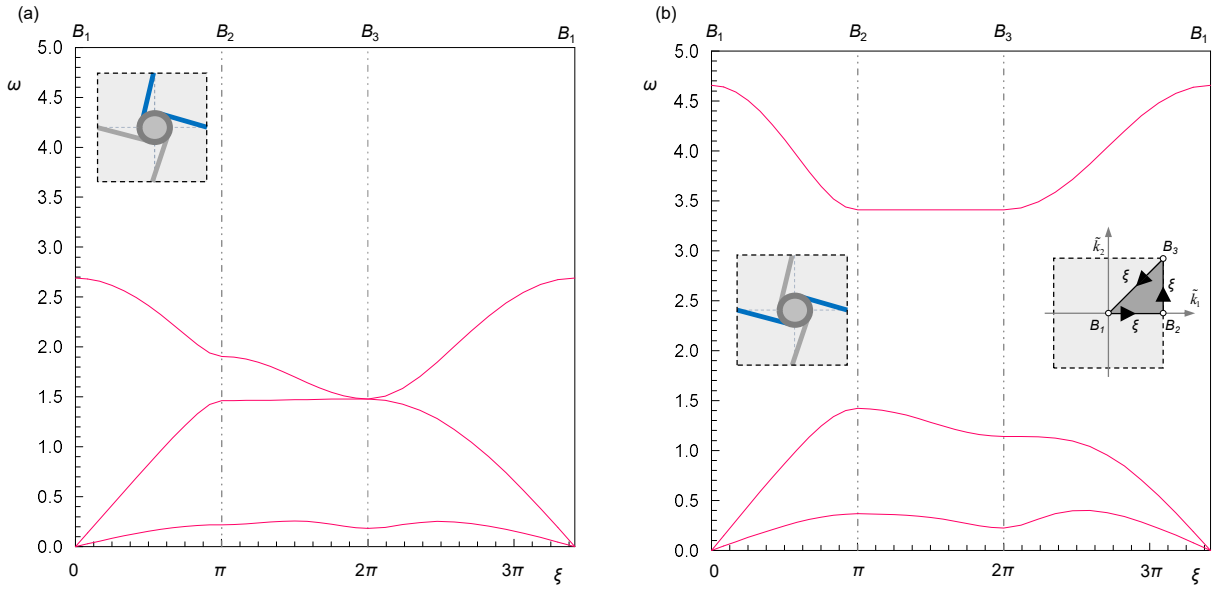

Figure 3.9 Case 4. Dispersion spectrum with inhomogeneous ligaments with $\rho_i / \rho_r = 1$ for a (a) non-centrosymmetric cell, (b) centrosymmetric cell

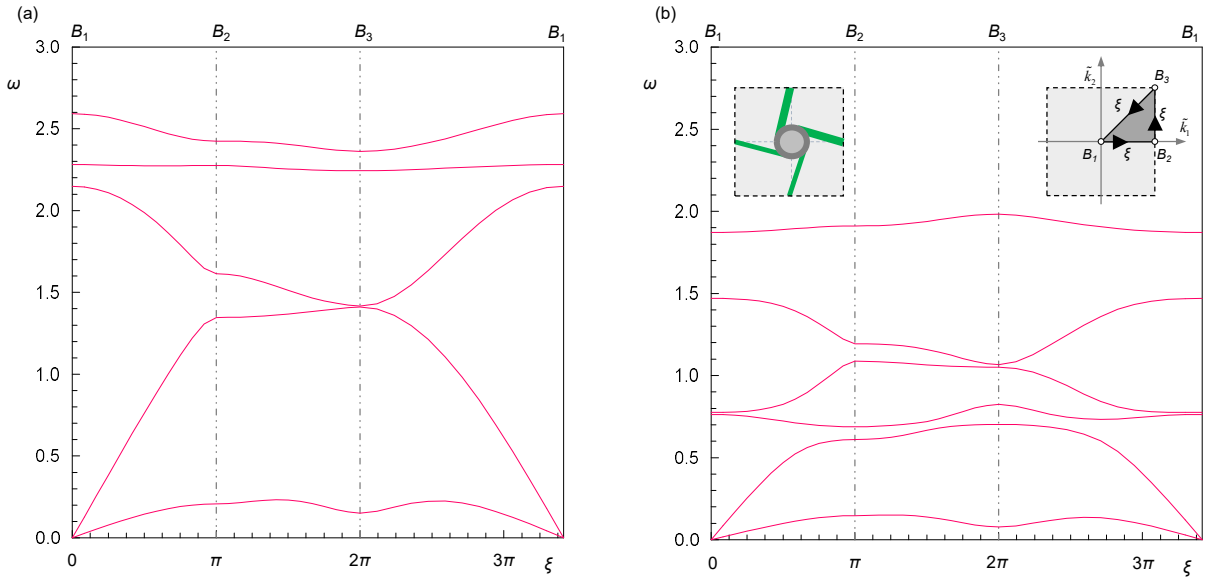

Figure 3.10 Case 5. Dispersion spectrum with the parameter (a) $\rho_b / \rho_r = 1$, (b) $\rho_b / \rho_r = 10$.

In the case 5 the dispersion spectrum is obtained for a non-centrosymmetric cell composed by a filled ring and massive ligaments. Increasing the parameter ρ_b / ρ_r, the frequencies decrease and new curves related to local waveforms occur. They can be observed a strong interaction with the other branches. In particular, in Figure 3.10b the second and the third curves do not cross each. However, this scenario does not necessarily correspond to the birth of a full band gap, because the considered boundary $\partial \mathcal{B}_1$ does not encloses the entire irreducible Brillouin zone for non-centrosymmetric cell.

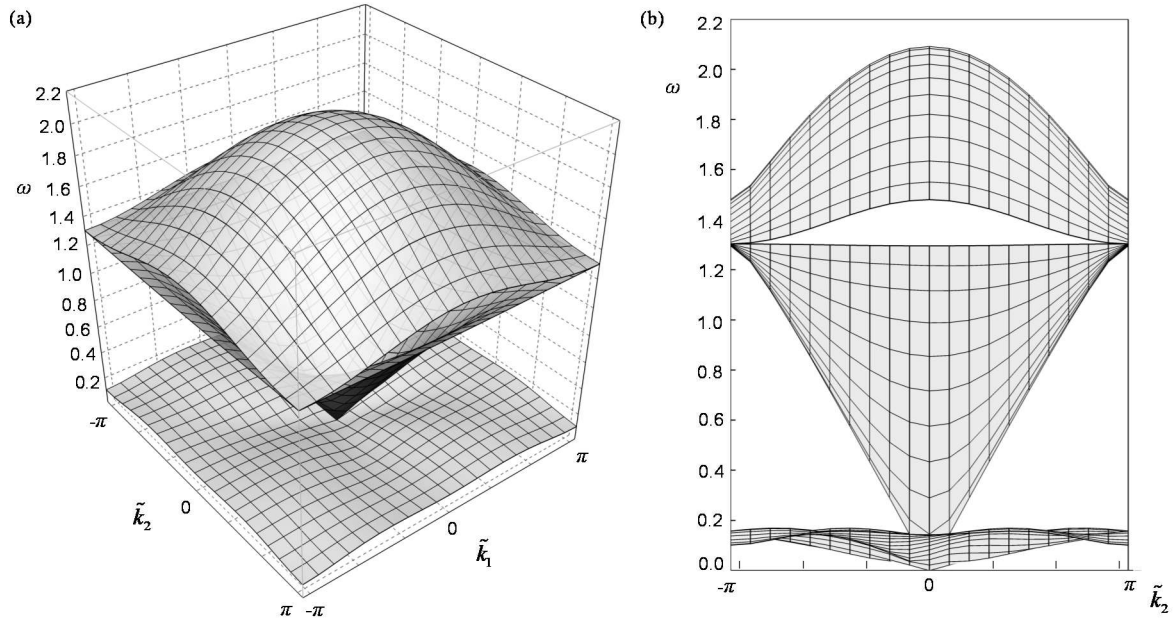

Figure 3.11 Reference case. Dispersion spectrum with the parameter $t_b / H = 1/20$, $t_r / t_b = 3$, $R / H = 1/3$.

3.3.1. Mechanical tuning

A material that stops the propagation of harmonic waves with frequencies that do not belong to the spectrum, therefore a material that has a dispersion spectrum in which there is a total band gap, behaves as an acoustic filter for elastic waves. In this regard, the variation of the non-dimensional parameters (3.35) causes changes on the band gap amplitude Δ and on the center frequency γ. Therefore, the controlled variation of these parameters can be considered a mechanical tuning of the acoustic filter realized by tetrachiral material. The dispersion spectrum of the reference case for geometric parameter values of $t_b / H = 1/20$, $t_r / t_b = 3$, $R / H = 1/3$ is shown in Figure 3.11.

In the investigated parameter region, decreasing the mass density ratio ρ_b / ρ_r between the ligaments and the ring material, the band gap amplitude Δ increases for each intra-ring filler mass density. Furthermore, increasing the mass density ratio ρ_i / ρ_r between an intra-ring filler and the ring material the band gap amplitude Δ grows up (Figure 3.12a). A similar behavior can be observed for the center frequency in Figure 3.12b, where the pink band includes the values of the frequencies that are within the band gap for $\rho_i / \rho_r = 10$. For instance, chosen the center frequency $\gamma = 1.3$, that corresponds to the double frequency in the 3D dispersion spectrum of the reference case (Figure 3.13), and $\rho_i / \rho_r = 10$, it is obtained $\rho_b / \rho_r \simeq 16$ (red dot in Figure 3.12b) and a band gap amplitude $\Delta \simeq 0.45$ (red dot i Figure 3.12a). The dispersion spectrum obtained for this parameter is shown in Figure 3.14. For the same center frequency, other solutions with different band gap amplitudes can be achieved (green, blue and orange dots in Figure 3.12). The dispersion spectrum with center frequency $\gamma = 1.3$ obtained with the parameters $\rho_i / \rho_r = 0$ (empty ring) and $\rho_b / \rho_r \simeq 18$ (orange dots in Figure 3.12) is shown in Figure 3.15.

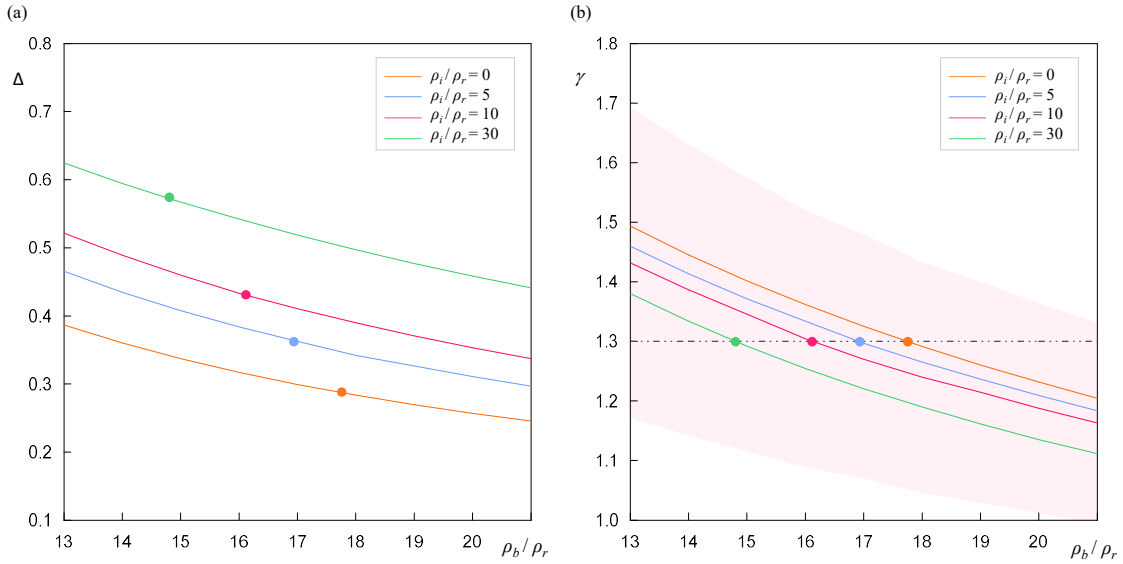

Figure 3.12 (a) Band gap amplitude, (b) Center frequency for a tetrachiral material with massive ligaments and intra-ring filler.

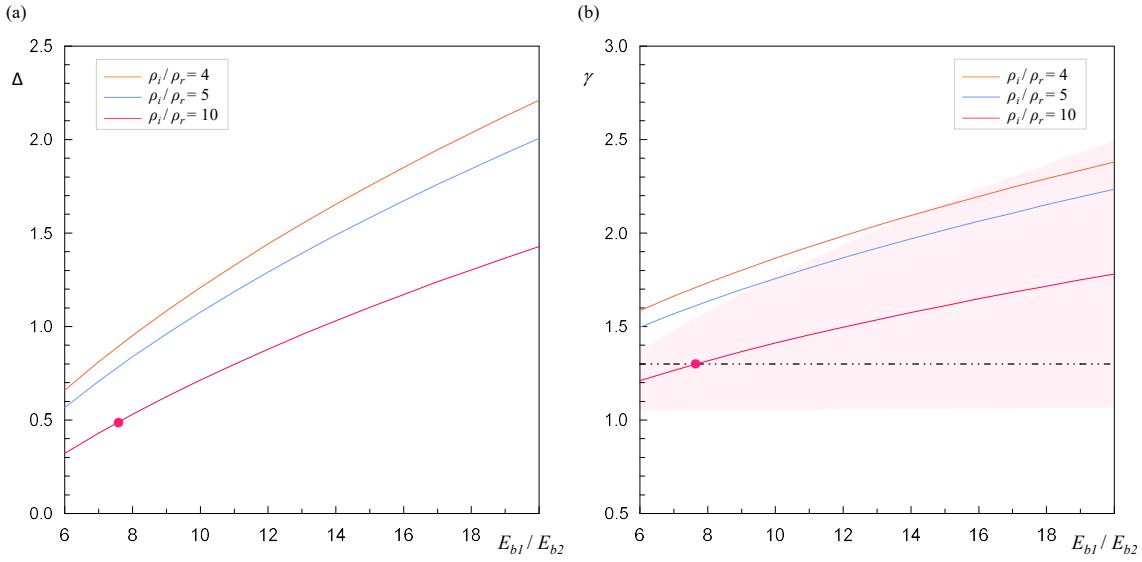

Figure 3.13 (a) Band gap amplitude, (b) Center frequency for a tetrachiral material with inhomogeneous ligaments and intra-ring filler.

Alternatively, the band gap amplitude changes by tuning the ratio E_{b1}/E_{b2} and by varying the intra-ring elastic filler mass density. Increasing the ratio E_{b1}/E_{b2} the band gap amplitude grows up for each intra-ring filler mass density (Figure 3.13a). In reverse, increasing the mass density ratio ρ_i/ρ_r between an intra-ring filler and the ring material the band gap amplitude Δ decreases. For instance, for the center frequency $\gamma = 1.3$ and $\rho_i/\rho_r = 10$, it is obtained $\rho_b/\rho_r \simeq 8$ (red dot in Figure 3.13b) and the band gap amplitude $\Delta \simeq 0.5$ (red dot in Figure 3.13a). The dispersion spectrum obtained for this parameter is shown in Figure 3.16.

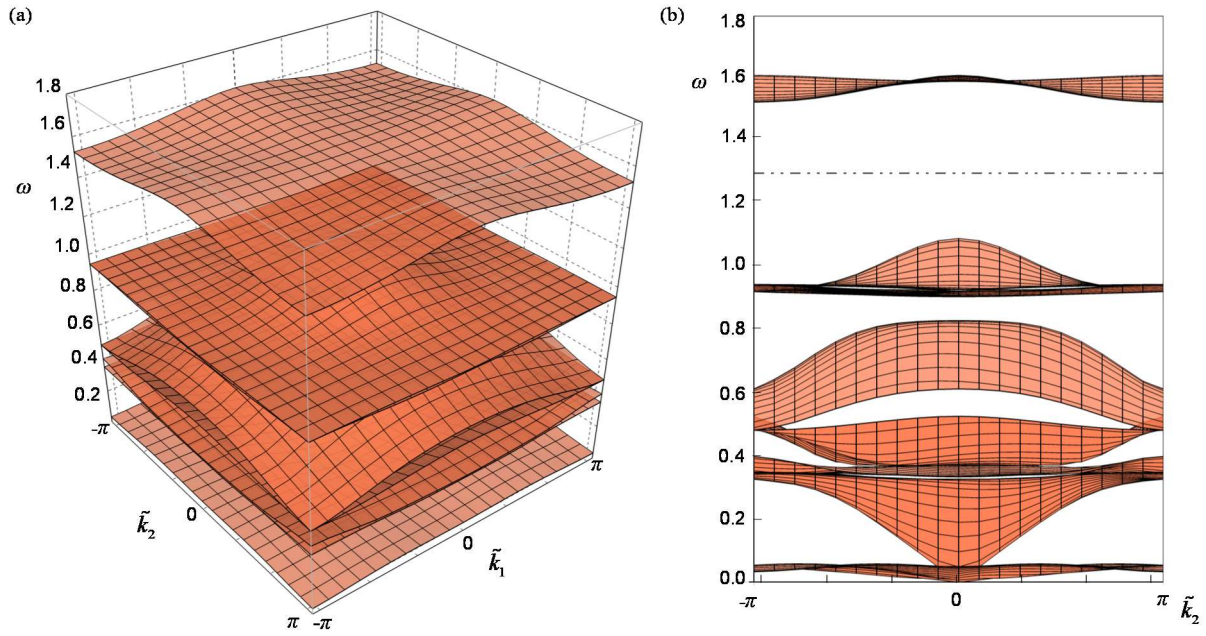

Figure 3.14. Dispersion spectrum of a tetrachiral material with massive ligaments, intra-ring heavy filler and parameters $\rho_b / \rho_r = 16$ and $\rho_t / \rho_r = 10$.

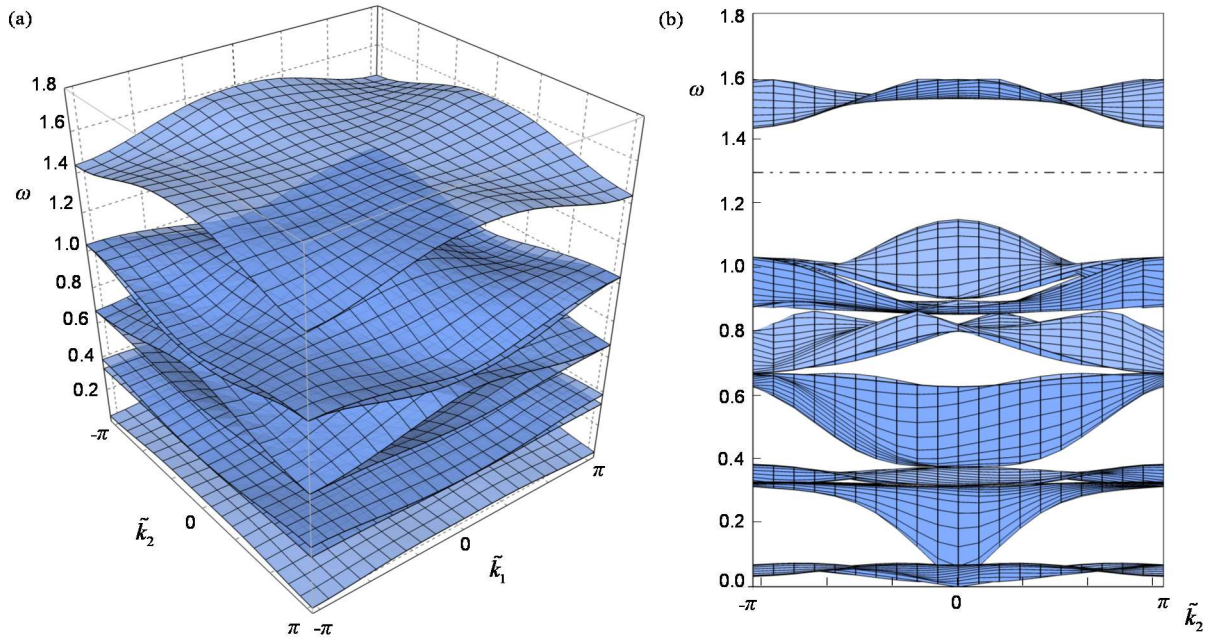

Figure 3.15 Dispersion spectrum of a tetrachiral material with massive ligaments and parameter $\rho_b / \rho_r = 18$.

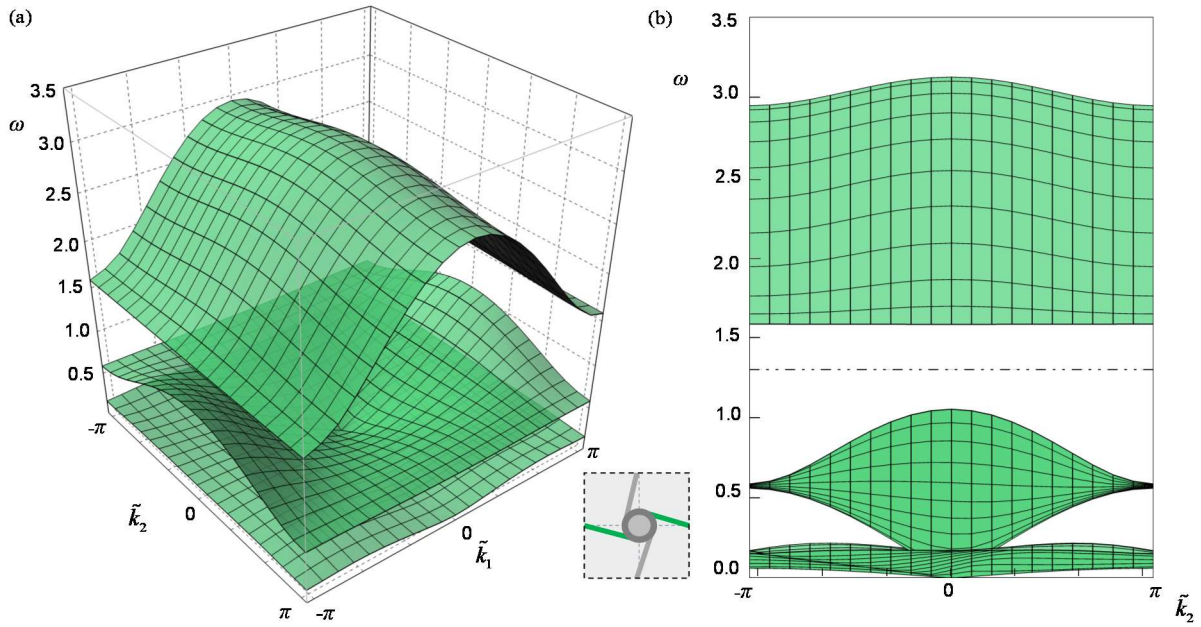

Figure 3.16 Dispersion spectrum of a tetrachiral material with intra-ring heavy filler, inhomogeneous massless ligaments and parameters $E_{b1}/E_{b2}=8$ and $\rho_i/\rho_r=10$.

The Figures 3.12 and 3.13 can be used as a design alternative of tetrachiral materials for given pairs of the band gap amplitude and the center frequency. The Table 3.2 reports two models in which the parameters (3.35) are obtained respectively from Figures 3.12 and 3.13, setting $\Delta=0.45$ and $\gamma=1.4$.

3.3.2. Performance as acoustic filters

The effects of an acoustic filter on the propagation of harmonic waves can be observed by modeling a finite dimension system and imposing a harmonic displacement, with frequency ϖ, on a boundary (Zhu et al., 2016). A numerical experimentation has been carried out by using the software COMSOL Multiphysics. The domain of the pseudo-experiment is composed by a finite dimension rectangular strip of homogeneous material, with a central core realized by a cluster of 11x11 tetrachiral cells (Figure 3.17).

Table 3.2 Parametric values in the models.

	ρ_i/ρ_r	ρ_b/ρ_r	E_{b1}/E_{b2}	Δ	γ
Model 1	10	13.5	1	0.5	1.4
Model 2	10	0	9.5	0.5	1.4
Model 3	0	10	1	0.496	1.675

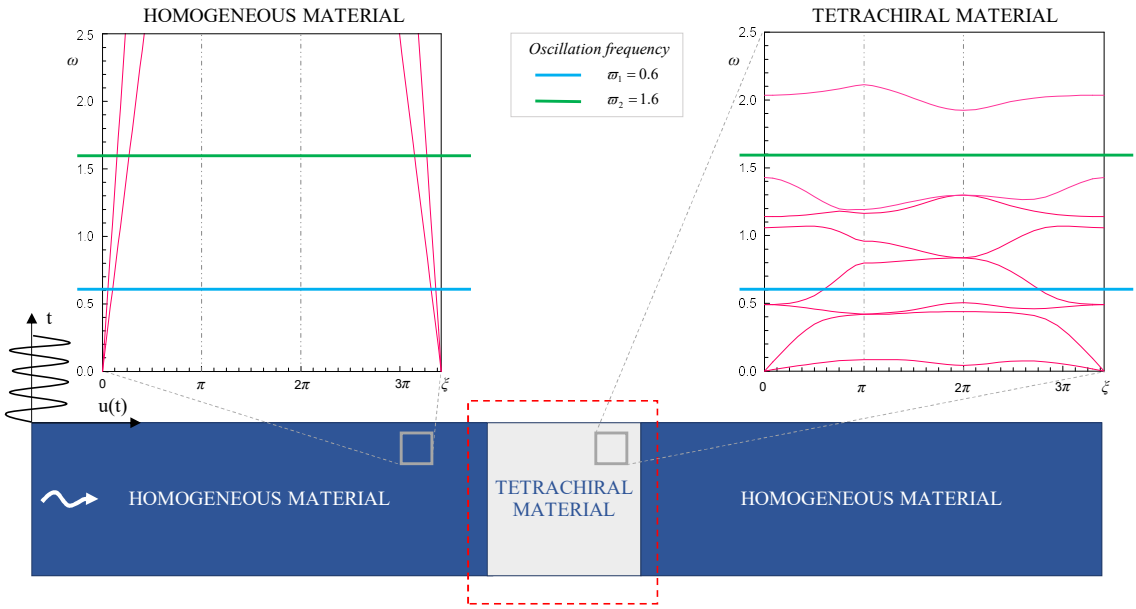

Figure 3.17 Rectangular strip of homogeneous material, with a central cluster of eleven tetrachiral cells, with the corresponding dispersion spectra.

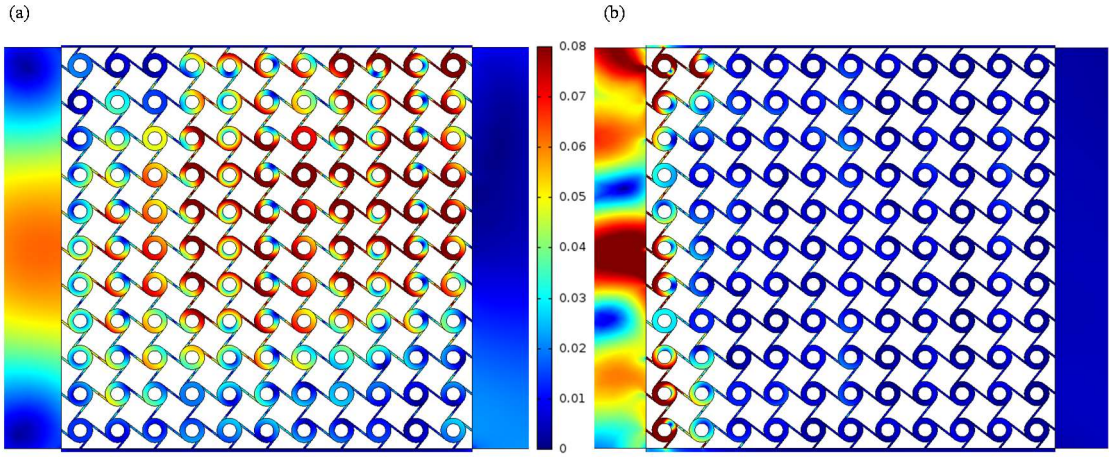

Figure 3.18 Absolute displacements D of the tetrachiral core at the time instant $t = 0.001\ s$ for an imposed harmonic displacement with frequency (a) $\varpi_1 = 0.6$, (b) $\varpi_2 = 1.6$.

For this example, the parameters (3.35) assume the values reported for the model 3 in the Table 3.2. By evaluating the dispersion spectra of the homogeneous material and the tetrachiral material, a full band gap, with amplitude $\Delta = 0.496$ and center frequency $\gamma = 1.675$, is observed in the dispersion spectrum of the tetrachiral material (Figure 3.17).

An automatic procedure has been employed to properly discretize the solid domain, with suited mesh refinements at the interface with the chiral media. Free boundary conditions have been imposed to the bottom and top sides of the domain, while the left and top sides have been fully clamped. As excitation source, an in-plane displacement has been imposed to the left side with single freqeuncy time-harmonic law. The numerical simulation of the undamped dynamic response has been achieved by means of an

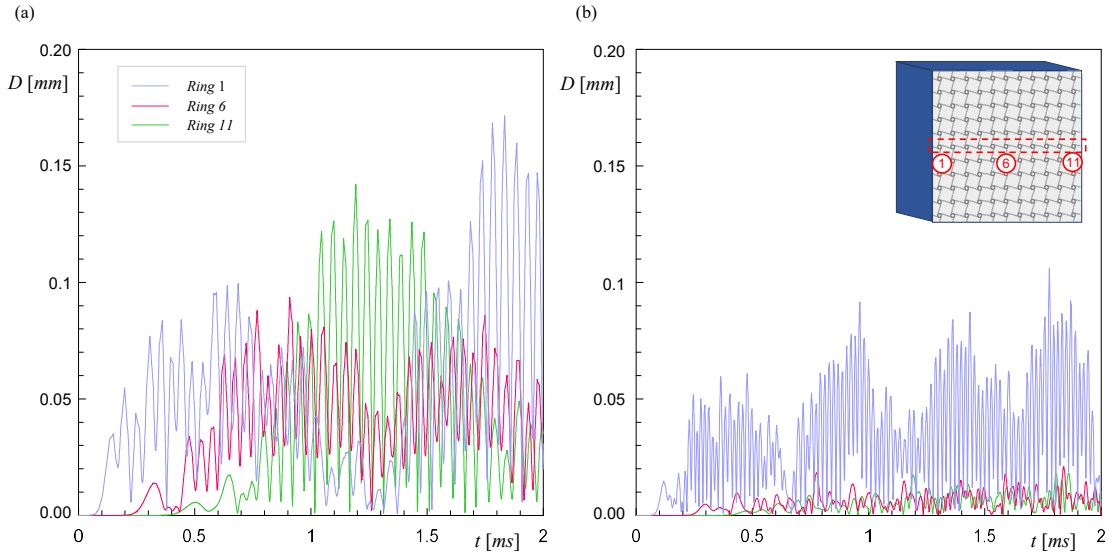

Figure 3.19 Time histories of the absolute displacements D of the rings 1, 6 and 11 of the tetrachiral core for an imposed harmonic displacement with frequency (a) $\varpi_1 = 0.6$, (b) $\varpi_2 = 1.6$.

implicit time-stepping scheme (generalized-α method). After the mesh refinements required to satisfy convergence criteria and by controlling the time step, the dynamic undamped response has been observed in the tetrachiral core and in the adjacent regions of the homogeneous material (see Figure 3.18). Looking at a certain time instant, the color map of the absolute displacement D characterizing the response to the excitation frequency $\varpi_1 = 0.6$ shows a marked propagation of elastic waves through the tetrachiral core (Figure 3.18a). The wave propagation is also confirmed by the time histories of the absolute displacements of the core rings (Figure 3.19a). Indeed, the peak displacement values of the ring 1 (the closest to the excited side) are quantitatively comparable with those of the ring 11 (the farthest from the excited side). On the contrary, the wave propagation is stopped by the tetrachiral core for a different excitation frequency $\varpi_2 = 1.6$ (Figure 3.19b). Indeed, the time histories of the core rings show that the peaks of the absolute displacements decrease with the distance from the excited side (Figure 3.19b). These dynamic phenomena of wave passing or stopping are related to the different excitation frequencies, which falls within the pass and stop bands of the tetrachiral material spectrum, respectively (Figure 3.17).

3.4. Parametric optimization

A parametric optimization for the search of full and partial band gaps with the largest amplitude and lower center frequency is carried out.

Defining the vector $\boldsymbol{\mu}$ that collects n parameters and plays the role of multi-dimensional variable, the bandwidth maximization of low-frequency band gaps can be based on the definition of a suited $\boldsymbol{\mu}$-dependent objective function, which simultaneously accounts for the gap amplitude and the band

center-frequency, hence qualifying in this respect as a multi-objective function. To this purpose, the non-dimensional ratio can be defined as

$$\Delta\omega_{kh}(\boldsymbol{\mu}) = \frac{\min\limits_{\tilde{\mathbf{k}}\in B_1}\left(\omega_k(\tilde{\mathbf{k}},\boldsymbol{\mu})\right) - \max\limits_{\tilde{\mathbf{k}}\in B_1}\left(\omega_h(\tilde{\mathbf{k}},\boldsymbol{\mu})\right)}{\frac{1}{2}\left[\min\limits_{\tilde{\mathbf{k}}\in B_1}\left(\omega_k(\tilde{\mathbf{k}},\boldsymbol{\mu})\right) + \max\limits_{\tilde{\mathbf{k}}\in B_1}\left(\omega_h(\tilde{\mathbf{k}},\boldsymbol{\mu})\right)\right]}, \tag{3.36}$$

where, supposing that the frequencies are sorted in ascending order, the numerator stands for the typically positive (even if possibly zero) gap amplitude between the *k*-th and *h*-th consecutive dispersion surfaces (where $k = h+1$), while the denominator stands for the band center-frequency. When the numerator is negative, no band gap is present between the two surfaces. Therefore, the optimization problem essentially consists in searching for the vector $\boldsymbol{\mu}$ that maximizes the objective function in the admissible parameter region. Consequently, the optimization issue can be mathematically formulated as a constrained maximization problem:

$$\begin{aligned} &\underset{\boldsymbol{\mu}}{\text{maximize}}\ \Delta\omega_{kh}(\boldsymbol{\mu}) \\ &\text{s.t. } \boldsymbol{\mu}_{\min} \le \boldsymbol{\mu} \le \boldsymbol{\mu}_{\max} \\ &\mathbf{g}(\boldsymbol{\mu}) \le 0, \end{aligned} \tag{3.37}$$

where $\boldsymbol{\mu}_{\min}$ and $\boldsymbol{\mu}_{\max}$ fix the boundaries of admissibility for the parameters vector, and $\mathbf{g}(\boldsymbol{\mu})$ denotes a vector function defining additional relations, introduced – if necessary - to costrain a certain slave parameter as a known function of the other master parameters (Bacigalupo et al., 2017). Altogether, the constraints define a properly bounded space for the parameters vector.

Due to its mathematical formulation, the optimization problem turns out to be a challenging task in non-linear programming. Moreover, since the multi-variable objective function is not concave in the general case, the function maximization cannot be treated as a concave maximization problem. Multiple solutions associated to local maxima can co-exist. Therefore, the global maximum is necessarily approximated by the highest among several local maxima obtained numerically.

A multi-start technique is used in conjunction with the Globally Convergent Method of Moving Asymptotes, or GCMMA. In the multi-start technique the method is applied repeatedly a number S of times, with different initializations, and the best design vector found in all the repetitions is taken as a surrogate of a globally optimal parameters vector. As for the specific choice of the multi-start technique, the following two approaches are considered in the following:

1) A Monte Carlo initialization of the variables, taken as realizations of independent uniformly distribuited random variables with supports $[\mu_i^{\min}, \mu_i^{\max}]$ for *i*-th variable μ_i ;
2) A quasi-Monte Carlo initialization, obtained at the first generating a quasi-random Sobol sequence (Niederreiter, 1992) on the n -dimensional unit cube $[0,1]^n$, then, applying to every vector belonging to such a sequence the mapping $\mathbf{h}:[0,1]^n \to \mathbb{R}^n$, with $\mathbf{h}(\mathbf{y})$ being defined as

$$\mathbf{h}(\mathbf{y}) = \begin{pmatrix} \mu_1(\mathbf{y}) \\ \mu_2(\mathbf{y}) \\ \vdots \\ \mu_n(\mathbf{y}) \end{pmatrix} = \begin{pmatrix} \mu_1^{\min} + \left(\mu_1^{\max} - \mu_1^{\min}\right) y_1 \\ \mu_2^{\min} + \left(\mu_2^{\max} - \mu_2^{\min}\right) y_2 \\ \vdots \\ \mu_n^{\min} + \left(\mu_n^{\max} - \mu_n^{\min}\right) y_n \end{pmatrix}. \tag{3.38}$$

Compared with the Monte Carlo initialization method, the quasi-Monte Carlo approach has the advantages of being exactly replicable, and of generating more uniform sequences of initial points, whereas with the Monte Carlo approach there is in principle the possibility of generating the same initial point (or very similar initial points) more than once in the sequence (Figure 3.20).

The GCMMA is an extension of the method of moving asymptotes (MMA) (Svanberg,1987) which searches for a locally optimal solution of a nonlinear programming problem by solving a sequence of simpler maximization sub-problems, at each iteration m. These are obtained by approximating the objective and constraint functions of the original optimization problem around the current vector $\boldsymbol{\mu}^{(m)}$ of the variables, and updating such variables after solving each sub-problem. From an optimization perspective, each sub-problem has the following properties (Christensen and Klarbring, 2004):

1) The approximations $\Delta\tilde{\omega}_{kh}^{(m)}(\boldsymbol{\mu})$ are first order approximations, in the sense that, when the function to be approximated is locally differentiable, there is no error in the approximation of the function value and of its gradient when evaluated at the current design variables (for the objective function, local non-differentiability may occur in case the band gap at the current variables is null, if this is due to the second and third dispersion surfaces being tangent at one point of the domain);
2) Such approximations are concave functions;
3) The approximation $\Delta\tilde{\omega}_{kh}^{(m)}(\boldsymbol{\mu})$ is separable, meaning that it is the sum of single-variable functions (one function for each variable), which makes each optimization sub-problem quite easy to solve through standard Lagrange multiplier techniques.

The MMA is based on a more flexible approximation, which is generated using a technique named of *moving asymptotes*. This means that each approximation $\Delta\tilde{\omega}_{kh}^{(m)}(\boldsymbol{\mu})$ has the form

$$\Delta\tilde{\omega}_{kh}^{(m)}(\boldsymbol{\mu}) = \Delta\omega_{kh}^{(m)}(\boldsymbol{\mu}^{(m)}) + \sum_{i=1}^{n} \frac{\Delta\tilde{\omega}_{kh}^{U_{i,(m)}}}{U_i^{(m)} - \mu_i} + \sum_{i=1}^{n} \frac{\Delta\tilde{\omega}_{kh}^{L_{i,(m)}}}{\mu_i - L_i^{(m)}}, \tag{3.39}$$

where, for each iteration, $\Delta\tilde{\omega}_{kh}^{U_{i,(m)}}$, $\Delta\tilde{\omega}_{kh}^{L_{i,(m)}}$, $U_i^{(m)}$ and $L_i^{(m)}$ are suitable constants (Svanberg,1987), and, to get a bounded approximation, the constraints

$$L_i^{(m)} < a_i^{(m)} \le \mu_i^{(m)} \le b_i^{(m)} < U_i^{(m)}, \tag{3.40}$$

are added for other suitable constants $a_i^{(m)}$ and $b_i^{(m)}$ (Svanberg, 1987). The name of the method derive from the fact that the vertical lines $\mu_i = L_i^{(m)}$ and $\mu_i = U_i^{(m)}$ are asymptotes for the approxiamtion (3.39), which move from each iteration to the successive one. It is worth remarking that MMA may not always converge to a stationary point of the original optimization problem. For this reason, its variation

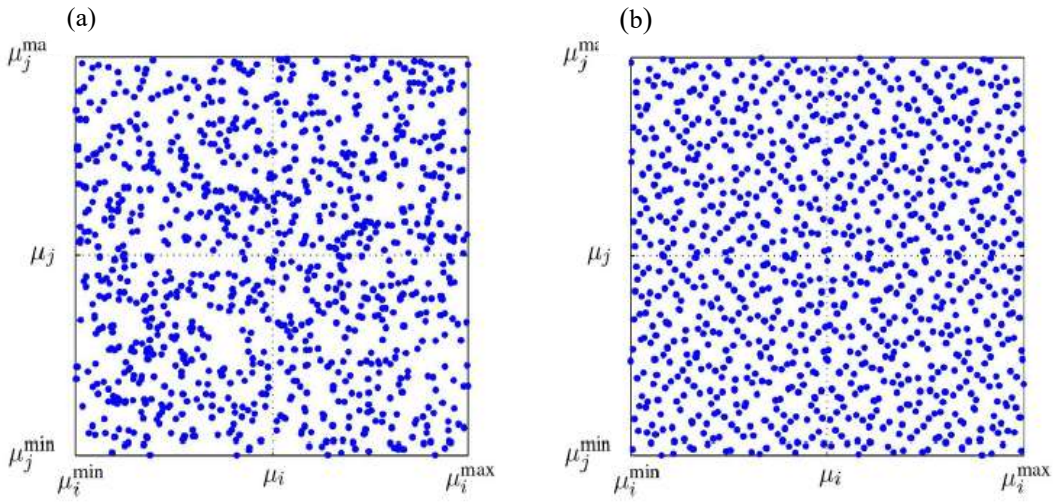

Figure 3.20 Initialization of a 2-dimensional admissible region of the parameter domain: (a) Montecarlo sampling and (b) quasi-Montecarlo sampling.

GCMMA was presented in Svanberg (2002) as a globally convergent version of MMA, in which the convergence of the modified method to a stationary point of the original problem is guaranteed. However, due to the high nonlinearity of that problem, such a point is not guaranteed to be its global minimizer. For this motivation, to improve the quality of the solution obtained by GCMMA, the method is combined with a quasi-Monte Carlo multi-start technique.

The optimization problem for the tetrachiral material can be formulated as the constrained maximization of a four variables objective function defined according to equation (3.36). Therefore, the search for the optimal solution is performed in a properly-bounded four-dimensional space of the non-dimensional mechanical parameters expressing the ligament slenderness, the ring-to-cell aspect ratio, the chirality angle and the ring-to-ligament width ratio.

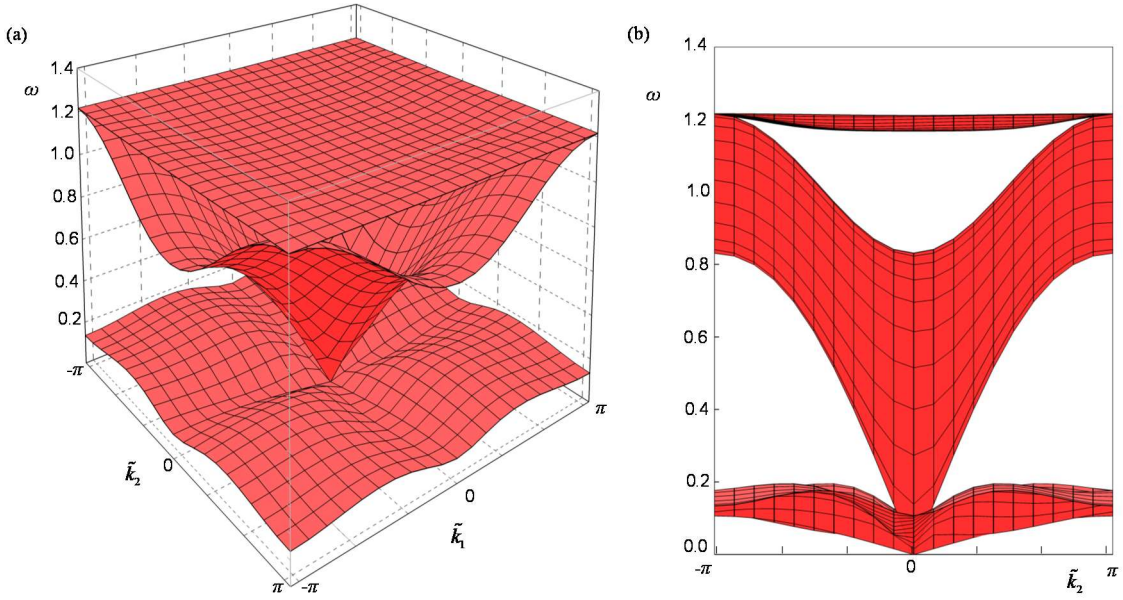

Figure 3.21 Dispersion spectrum for the optimized tetrachiral material ($t_b / H = 0.06$, $t_r / t_b = 3.19$, $R / H = 0.20$).

The optimization problem for the tetrachiral material is found not to admit solutions corresponding to full band gaps in the admissible parameter space. The problem is reformulated to search for partial band gaps and the highest amplitude stop band at the lowest center frequency is found between the second acoustic surface and the optical surface along the two orthogonal propagation directions connecting the centroids of adjacent rings (Figure 3.21).

CHAPTER 4

INERTIAL METAMATERIAL WITH VISCOELASTIC RESONATORS

Focusing on the dynamic response of periodic microstrucutured materials, a major issue of mechanical interest consists in governing the Bloch wave propagation by means of spectral design techniques and/or energy dissipation mechanisms. To this purpose, in chapter 3, the possiblity to inhibit the Bloch waves propagation around certain target center-frequencies by designing the microstructural parameters in order to open band gaps in the material dispersion spectrum is discussed.

In the spectral design of periodic microstructure materials for low-frequency wave filtering, the extent and dimensionality of the optimal solution domain can be significantly enlarged by designing *inertial* or *acoustic metamaterials*, realized by introducing auxiliary massive oscillators, mechanically coupled to the cell microstructure. Indeed, if the oscillators are properly tuned (*local resonators*), their dynamic interaction with the microstructure ends up opening a band gap in the dispersion spectrum. It can be demonstrated that the achievable band gap is nearly centered at the oscillator frequency, with a bandwidth almost directly proportional to its inertial mass.

Starting from the scientific background reported in chapter 1, the physical-mathematical formulation of advanced microstructural models for locally resonant acoustic metamaterials is an active research field in theoretical mechanics, whose continuous development is currently motivated by some open investigation issues. First, a general improvement in the elastodynamic description of the linear and nonlinear dissipation mechanisms occurring in infinite periodic phononic systems has been recognized as the theoretical key-point for the future advances in the energetically consistent modelization and spectral design of acoustic metamaterials (Hussein et al., 2014). Second, a completely new class of mechanical meta-behaviours has been postulated to be developable in the next few years, by exploiting the virtuous contrast and synergy among constituent ingredient materials featured by strongly dissimilar elastic, plastic and viscous properties (Bertoldi et al., 2017). Based on these motivations, this chapter presents a beam lattice formulation for describing the wave dynamics of a dissipative acoustic metamaterial, originated by a periodic non-dissipative microstructure, viscoelastically coupled with local resonators. The viscoelastic coupling is consistently derived by a physical-mathematical construct based on the Boltzmann superposition integral, whose kernel is properly approximated by a Prony series. Consequently, the non-conservative wave propagation is governed by a linear homogeneous system of integro-differential equations of motion. This integral description of the viscoelastic metamaterial dissipation enriches the classic formulations of viscous damping, sometimes following the rheological Rayleigh or Maxwell models, which can be recovered for particular parameter values and low-order approximations of the governing equations in the transformed Laplace space. According to the so-called *inverse method* (Hussein et al., 2014), the associated non-polynomial eigenproblem is solved in the space of complex-valued frequencies by assigning real-valued wavevectors. Subsequently, the complex spectrum can be reformulated in terms of real-valued damped frequencies and damping ratios. This solution approach

differs from the complementary *direct method* in which the governing eigenproblem is solved in the space of complex-valued wavevectors by assigning real-valued frequencies.

In order to characterize the free and forced propagation of damped waves in the acoustic metamaterials, a discrete linear model of the periodic beam lattice microstructure, visco-elastically coupled with local resonators, is formulated (Section 4.1). Therefore, the dynamic problem concerning the wave propagation of damped waves is stated according to the Floquet-Bloch theory (Section 4.2). First, the complex dispersion spectrum characterizing the free dynamics is determined for the beam lattice with quadrilateral elementary cell, and the effects of different approximations of the coupling relaxation functions are parametrically analysed, with reference to the exact dispersion curves (Section 4.3). The exact eigensolution given by numerical solvers is compared with the approximate solutions achievable by the application of asymptotic perturbation methods (Section 4.4). Second, the forced response to harmonic single-frequent external sources is investigated in the frequency and time domain for the fundamental cases of non-resonant, resonant and quasi-resonant external forces (Section 4.5).

4.1. Governing equations of the beam lattice model

The periodic metamaterials with viscoelastic resonators can be based on different planar topologies described by quadrilateral or triangular beam lattices (Figure 4.1). The periodic cell of the metamaterial, with characteristic size a and unitary out-of-plane depth d, is featured by a centrosymmetric microstructure realized by a massive rigid ring, with radius R, mass M_1 and rotational inertia J_1. Each ring is connected with the rings of adjacent cells by n identical flexible and light ligaments of length l, width w and Young's modulus E_s. The ring-ligament connection is supposed to realize a perfectly rigid joint. Each ring hosts a heavy disk with radius r, co-centered with the ring center and embedded in a soft viscoelastic annular filler. This circular massive inclusion plays the role of local resonator. The mass and rotational inertia of the local resonator are M_2 and J_2, respectively. The motion of the rigid ring is described by the in-plane displacement vector $\mathbf{u}$ and the rotation ϕ, referred to the internal point located at the ring center of mass. The motion of the resonator is described by the in-plane displacement vector $\mathbf{v}$ and the rotation θ. The integral-differential equations governing the forced response of motion of a reference cell read (Bacigalupo and Gambarotta, 2017c)

$$\begin{aligned}
&M_1\ddot{\mathbf{u}} + \int_{-\infty}^{t} k_d(t-\tau)\frac{d}{d\tau}(\mathbf{u}-\mathbf{v})\,\mathrm{d}\tau + \sum_{i=1}^{n}\left[\mathbf{K}_i\left(\mathbf{u}-\mathbf{u}_i\right)+\mathbf{k}_i\left(\phi+\phi_i\right)\right] = \mathbf{f}\\
&J_1\ddot{\phi} + \int_{-\infty}^{t} k_\theta(t-\tau)\frac{d}{d\tau}(\phi-\theta)\,\mathrm{d}\tau + \sum_{i=1}^{n}\left[\mathbf{k}_i\cdot\left(\mathbf{u}-\mathbf{u}_i\right)+K_a\left(\phi+\phi_i\right)+K_l\left(\phi-\phi_i\right)\right] = g\\
&M_2\ddot{\mathbf{v}} + \int_{-\infty}^{t} k_d(t-\tau)\frac{d}{d\tau}(\mathbf{v}-\mathbf{u})\,\mathrm{d}\tau = \mathbf{0}\\
&J_2\ddot{\theta} + \int_{-\infty}^{t} k_\theta(t-\tau)\frac{d}{d\tau}(\theta-\phi)\,\mathrm{d}\tau = 0,
\end{aligned} \tag{4.1}$$

where dot indicates derivative with respect to time t and the auxiliary stiffness parameters

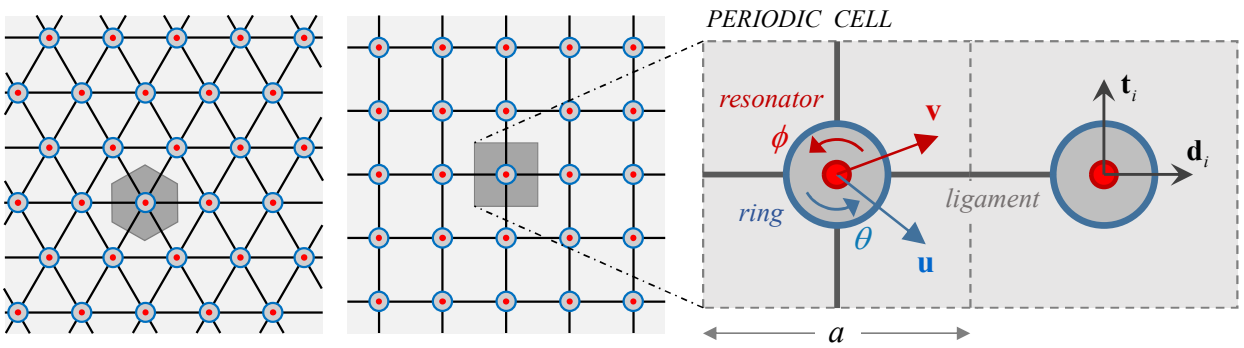

Figure 4.1 Beam lattice metamaterials and reference periodic cell.

$$\mathbf{K}_i = E_s\left(\frac{w}{l}\right)\left[(\mathbf{d}_i \otimes \mathbf{d}_i) + \left(\frac{w}{l}\right)^2 (\mathbf{t}_i \otimes \mathbf{t}_i)\right], \qquad \mathbf{k}_i = E_s \frac{a}{2}\left(\frac{w}{l}\right)^3 \mathbf{t}_i,$$
$$K_a = E_s\left(\frac{w}{l}\right)^3 \frac{a^2}{4}, \qquad K_l = E_s\left(\frac{w}{l}\right)^3 \frac{l^2}{12}, \tag{4.2}$$

while $k_d(t)$ and $k_\theta(t)$ are time-dependent relaxation functions accounting synthetically for the viscoelastic ring-resonator coupling. The in-plane displacement vector $\mathbf{u}_i$ and the rotation ϕ_i describe the motion of the n rings connected to the reference ring. The unit vector $\mathbf{d}_i$ accounts for the orientation of the i-th connection ligament, and $\mathbf{t}_i$ is the unit vector normal to $\mathbf{d}_i$, according to a counter-clockwise system. The reference ring is excited by the generalized external forces $\mathbf{f}$ and g, while the resonator is assumed unloaded. It is worth noting that assuming time-independent relaxation functions allows the recovery of the dynamic equations governing the non-dissipative beam lattice metamaterial

The soft viscoelastic filler is characterized by the translational and rotational relaxation functions $k_d(t)$ and $k_\theta(t)$ that can be modeled by using the Prony series. Considering only the first exponential term of the series, the relaxation functions read

$$k_d(t) = k_{de} + k_d \exp\left(-\frac{t}{t_r}\right) = k_{de}\left(1 + \beta_d \exp\left(-\frac{t}{t_r}\right)\right),$$
$$k_\theta(t) = k_{\theta e} + k_\theta \exp\left(-\frac{t}{t_r}\right) = k_{\theta e}\left(1 + \beta_\theta \exp\left(-\frac{t}{t_r}\right)\right), \tag{4.3}$$

where t_r is the relaxation time, k_{de}, k_d, $k_{\theta e}$, k_θ are dimensional mechanical coefficients, and $\beta_d = k_d / k_{de}$, $\beta_\theta = k_\theta / k_{\theta e}$ are the associated non-dimensional parameters, referred to as *viscosity ratios* in the following. The dependence of the non-dimensional relaxation function $\tilde{k}_d = k_d/(E_s d)$ on the non-dimensional time $\tilde{t} = t\sqrt{aE_S/M_1}$ is shown in Figure 4.2a for a fixed relaxation time and different β_d-values. The increment of the exponential decay rate for increasing viscosity ratios β_d can be

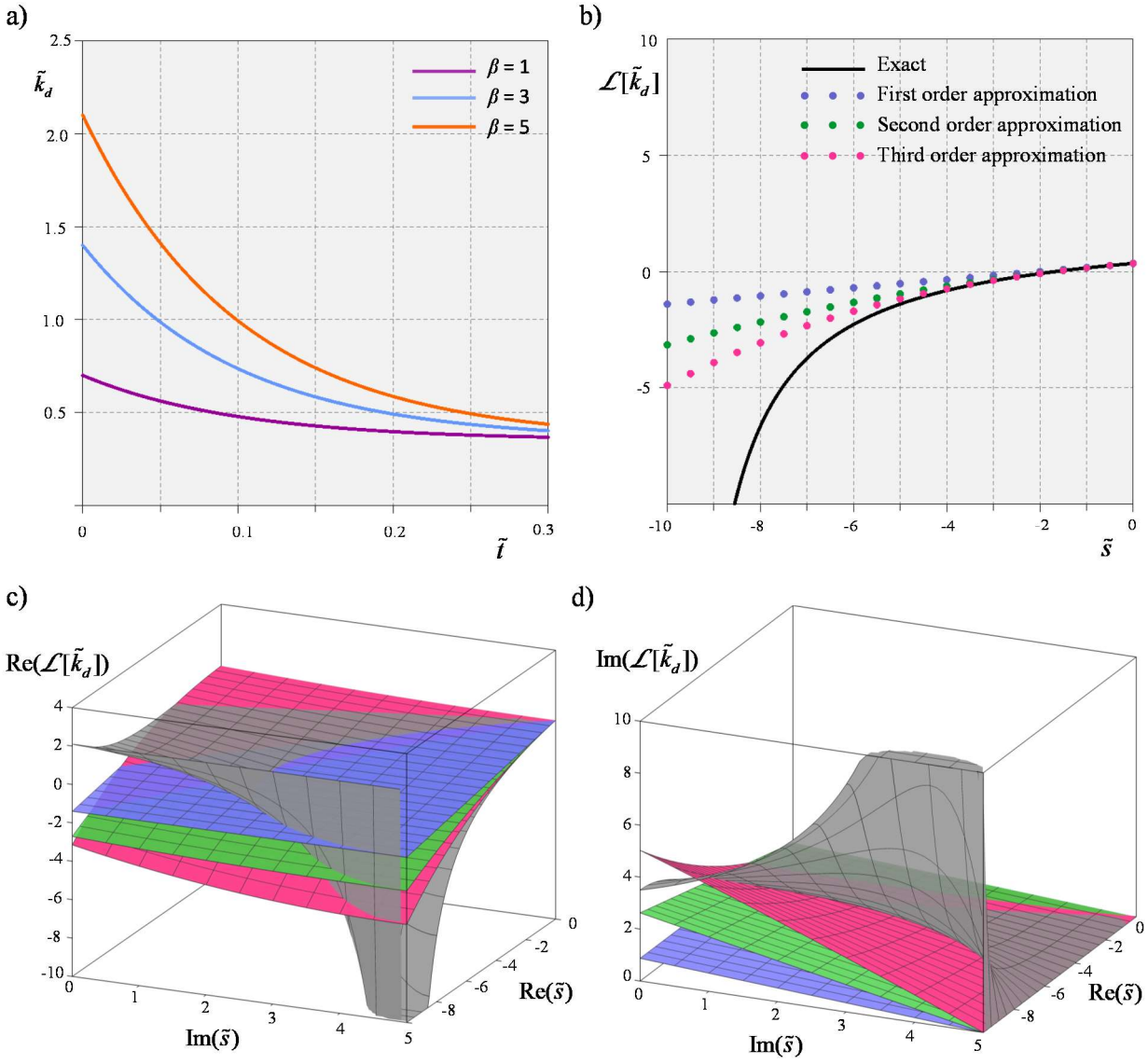

Figure 4.2 Viscoelastic kernel for $\tilde{t}_r = 1/10$, $\tilde{k}_{de} = k_{de}/(E_s d) = 35/100$: (a) Relaxation function versus time; (b) Exact and approximate Laplace transforms of the relaxation function versus the Laplace variable ($\beta_d = 5$), (c), (d) Real and imaginary parts of the Laplace transforms of the relaxation function versus the complex Laplace variable ($\beta_d = 5$).

appreciated. A similar qualitative scenario can be obtained for the time-dependence of the non-dimensional relaxation function $\tilde{k}_\theta = k_\theta/(a^2 E_s d)$.

4.2. In-plane Bloch waves

The propagation of elastic waves can be studied by applying the bilateral Laplace transform $\mathcal{L}[\bullet] = \int_{-\infty}^{\infty} (\bullet) \exp(-st)\,\mathrm{d}t$ to the equations (4.1), where s is the complex Laplace variable. According to the Floquet-Bloch theory, the quasi-periodicity conditions can be imposed on the displacements and the rotation in the Laplace space

$$\begin{aligned}\mathcal{L}[\mathbf{u}_i]-\mathcal{L}[\mathbf{u}]&=\hat{\mathbf{u}}\left(\exp(\imath\mathbf{k}\cdot\mathbf{x}_i)-1\right)\\ \mathcal{L}[\phi_i]\pm\mathcal{L}[\phi]&=\hat{\phi}\left(\exp(\imath\mathbf{k}\cdot\mathbf{x}_i)\pm1\right),\end{aligned}\tag{4.4}$$

where $\mathbf{x}_i$ is the vector pointing the i-th ring center, $\hat{\mathbf{u}}$, $\hat{\phi}$ are the displacement and rotation in the Bloch-Laplace space and $\mathbf{k}=q\mathbf{i}$ is the real-valued wavevector expressed through the polar coordinates, with q representing the wavenumber and $\mathbf{i}$ being the unit vector of the generic propagation direction. Therefore, the algebraic transformed equations of in-plane motion read

$$\begin{aligned}&M_1s^2\hat{\mathbf{u}}+R_d(s)(\hat{\mathbf{u}}-\hat{\mathbf{v}})+\sum_{i=1}^{n}\left[\mathbf{K}_i\left(1-\exp(\imath\mathbf{k}\cdot\mathbf{x}_i)\right)\hat{\mathbf{u}}+\mathbf{k}_i\left(1+\exp(\imath\mathbf{k}\cdot\mathbf{x}_i)\right)\hat{\phi}\right]=\hat{\mathbf{f}}\\ &J_1s^2\hat{\phi}+R_\theta(s)\left(\hat{\phi}-\hat{\theta}\right)+\sum_{i=1}^{n}\left[\begin{array}{l}\mathbf{k}_i\cdot\left(1-\exp(\imath\mathbf{k}\cdot\mathbf{x}_i)\right)\hat{\mathbf{u}}+\\ +K_a\left(1+\exp(\imath\mathbf{k}\cdot\mathbf{x}_i)\right)\hat{\phi}+K_l\left(1-\exp(\imath\mathbf{k}\cdot\mathbf{x}_i)\right)\hat{\phi}\end{array}\right]=\hat{g}\\ &M_2s^2\hat{\mathbf{v}}+R_d(s)(\hat{\mathbf{v}}-\hat{\mathbf{u}})=\mathbf{0}\\ &J_2s^2\hat{\theta}+R_\theta(s)(\hat{\theta}-\hat{\phi})=0,\end{aligned}\tag{4.5}$$

where $\hat{\mathbf{f}}$ and $\hat{g}$ are the generalized forces in the Bloch-Laplace space. The two auxiliary s-dependent rational functions $R_d(s)$ and $R_\theta(s)$ are the bilateral Laplace transform of the relaxation functions

$$\begin{aligned}R_d(s)&=\mathcal{L}[k_d]=\frac{k_{de}+(k_{de}+k_d)st_r}{s(1+st_r)},\\ R_\theta(s)&=\mathcal{L}[k_\theta]=\frac{k_{\theta e}+(k_{\theta e}+k_\theta)st_r}{s(1+st_r)}.\end{aligned}\tag{4.6}$$

If necessary for the sake of simplicity, the bilateral Laplace transforms (4.6) can be approximated with their h-order Taylor polynomials, centered at $s=0$, yielding

$$\begin{aligned}R_d(s)&\simeq k_{de}-k_d\sum_{j=1}^{h}(-1)^jt_r^js^j\\ R_\theta(s)&\simeq k_{\theta e}-k_\theta\sum_{j=1}^{h}(-1)^jt_r^js^j.\end{aligned}\tag{4.7}$$

It is worth noting that for $h=1$ the Taylor polynomials introduce in the equations (4.5) some linear terms in the Laplace variable, recovering the classical viscous damping originated by velocity-proportional dissipation. Specifically, the first, second and third order polynomial approximations of the Laplace transforms (4.6) are reported in Figure 4.2b considering $\mathcal{L}[\tilde{k}_d]$ as an analytical function of the non-dimensional variable $\tilde{s}=s\sqrt{M_1/(aE_s)}$, fixed a certain non-dimensional relaxation time $\tilde{t}_r$. The comparison with the exact function allows to appreciate the approximation accuracy in the closeness of the starting point $\tilde{s}=0$ up to the polar singularity at $\tilde{s}=1/\tilde{t}_r$. Furthermore, the real part $\mathrm{Re}\left(\mathcal{L}[\tilde{k}_d]\right)$ and the imaginary part $\mathrm{Im}\left(\mathcal{L}[\tilde{k}_d]\right)$ are properly compared with the respective first, second and third order approximations as a function of the complex $\tilde{s}$-variable in Figure 4c,d.

The matrix form of the linear algebraic equations (4.5) is $\mathbf{C}(\mathbf{k},s)\hat{\mathbf{U}}=\hat{\mathbf{F}}$, where $\hat{\mathbf{U}}=\left(\hat{\mathbf{u}}\quad\hat{\phi}\quad\hat{\mathbf{v}}\quad\hat{\theta}\right)^T$, $\hat{\mathbf{F}}=\left(\hat{\mathbf{f}}\quad\hat{g}\quad\mathbf{0}\quad0\right)^T$ and the matrix $\mathbf{C}(\mathbf{k},s)$ is a 6-by-6 Hermitian matrix having the explicit form

$$\mathbf{C}(\mathbf{k},s)=\begin{bmatrix}\mathbf{A}+s^2M_1\mathbf{I} & \mathbf{a}^- & -R_d(s)\mathbf{I} & \mathbf{0}\\ \mathbf{a}^+ & b+s^2J_1 & \mathbf{0} & -R_\theta(s)\\ -R_d(s)\mathbf{I} & \mathbf{0} & R_d(s)\mathbf{I}+s^2M_2\mathbf{I} & \mathbf{0}\\ \mathbf{0} & -R_\theta(s) & \mathbf{0} & R_\theta(s)+s^2J_2\end{bmatrix}, \tag{4.8}$$

where $\mathbf{I}$ is the 2-by-2 identity matrix and the submatrices $\mathbf{A}$, $\mathbf{a}^-$, $\mathbf{a}^+$ and b are

$$\begin{aligned}
\mathbf{A}&=R_d(s)\mathbf{I}+\sum_{i=1}^{n}\left[\left(1-\exp(\imath\mathbf{k}\cdot\mathbf{x}_i)\right)\mathbf{K}_i\right]=R_d(s)\mathbf{I}+\sum_{i=1}^{n}\left[\left(1-\cos(\mathbf{k}\cdot\mathbf{x}_i)\right)\mathbf{K}_i\right]\\
\mathbf{a}^-&=\sum_{i=1}^{n}\left[\left(1+\exp(\imath\mathbf{k}\cdot\mathbf{x}_i)\right)\mathbf{k}_i\right]=-\imath\sum_{i=1}^{n}\left[\sin(\mathbf{k}\cdot\mathbf{x}_i)\mathbf{k}_i\right]\\
\mathbf{a}^+&=\sum_{i=1}^{n}\left[\left(1-\exp(\imath\mathbf{k}\cdot\mathbf{x}_i)\right)\mathbf{k}_i^{\mathrm{T}}\right]=\imath\sum_{i=1}^{n}\left[\sin(\mathbf{k}\cdot\mathbf{x}_i)\mathbf{k}_i^{\mathrm{T}}\right]\\
b&=R_\theta(s)+\sum_{i=1}^{n}\left[K_a\left(1+\exp(\imath\mathbf{k}\cdot\mathbf{x}_i)\right)+K_l\left(1-\exp(\imath\mathbf{k}\cdot\mathbf{x}_i)\right)\right]=\\
&=R_\theta(s)+\sum_{i=1}^{n}\left[K_a\left(1+\cos(\mathbf{k}\cdot\mathbf{x}_i)\right)+K_l\left(1-\cos(\mathbf{k}\cdot\mathbf{x}_i)\right)\right],
\end{aligned} \tag{4.9}$$

where the equivalent exponential and trigonometric forms are reported.

4.3. Free wave propagation

For the free wave propagation, the complex-valued dispersion relations $s(\mathbf{k})$ can be determined by solving the eigenvalue problem associated to the homogeneous equations of motion $\mathbf{C}(\mathbf{k},s)\hat{\mathbf{U}}=\mathbf{0}$, obtained by setting to zero the generalized external forces ($\hat{\mathbf{f}}=\mathbf{0}$, $\hat{g}=0$). As preliminary remark, it must be highlighted that different eigenvalue problems are associated to the exact relaxation functions (4.6) and to each order of their approximations in s-power series (4.7). Specifically, the exact and approximate relaxation functions correspond to rational (non-polynomial) and polynomial eigenvalue problems in the s-unknown, respectively.

The following algebraic procedure to simplify the mathematical treatment of the eigenvalue problems (by conveniently reducing both rational and polynomial problems to higher dimension linear problems) is used:

- By considering the third eigenvalue problem in the unknown eigenvalue s as benchmark, the problem $\mathbf{C}(\mathbf{k},s)\hat{\mathbf{U}}=\mathbf{0}$ is expressed by separating the s-orders of the governing matrix $\mathbf{C}(\mathbf{k},s)$, yielding

$$\left(\mathbf{C}^{(0)}+s\mathbf{C}^{(1)}+s^2\mathbf{C}^{(2)}+s^3\mathbf{C}^{(3)}\right)\hat{\mathbf{U}}=\mathbf{0}, \tag{4.10}$$

  where the bracketed superscript of the matrices $\mathbf{C}^{(0)},\mathbf{C}^{(1)},\mathbf{C}^{(2)}$ and $\mathbf{C}^{(3)}$ denotes the s-order.
- The polynomial eigenvalue problem (4.10) is expressed in an equivalent linear form $\mathbf{L}(s)\mathbf{V}=\mathbf{0}$ where $\mathbf{V}=\left(s^2\hat{\mathbf{U}}\quad s\hat{\mathbf{U}}\quad \hat{\mathbf{U}}\right)^T$ and the matrix $\mathbf{L}(s)$ is written as

$$\mathbf{L}(s)=s\begin{bmatrix}\mathbf{C}^{(3)} & \mathbf{0} & \mathbf{0}\\ \mathbf{0} & \mathbf{I} & \mathbf{0}\\ \mathbf{0} & \mathbf{0} & \mathbf{I}\end{bmatrix}+\begin{bmatrix}\mathbf{C}^{(2)} & \mathbf{C}^{(1)} & \mathbf{C}^{(0)}\\ -\mathbf{I} & \mathbf{0} & \mathbf{0}\\ \mathbf{0} & -\mathbf{I} & \mathbf{0}\end{bmatrix}. \tag{4.11}$$

- The s -values that make the auxiliary higher-dimensional matrix $\mathbf{L}(s)$ singular coincide with the eigenvalues solving the polynomial eigenvalue problem (4.10). The corresponding eigenvectors coincide with a subvector of the vector $\mathbf{v}$.

The dispersion spectrum is composed by all the complex-valued relations $s(\mathbf{k})$ solving the eigenvalue problems for assigned real $\mathbf{k}$ -values. Precisely, the real and imaginary parts of each solution define a pair of dispersion surfaces defined in the bidimensional $\mathbf{k}$ -domain. Alternatively, the dispersion spectrum can be illustrated by representing the three-dimensional dispersion curves (or spectral branches) defined by the real and imaginary parts $\mathrm{Re}(s)$ and $\mathrm{Im}(s)$ of the complex-valued relations $s(q)$ along a particular propagation direction.

Focusing on the cellular metamaterial characterized by the quadrilateral beam lattice, the eigenvalue problem is stated for the particular periodic cell with square shape $(a=l+2R)$. For this metamaterial the submatrices (4.9) assume the particular form

$$\begin{aligned}
\mathbf{A}&=\begin{bmatrix}R_d(s)+\dfrac{2E_s wC(k_1)}{l}+\dfrac{2E_s w^3C(k_2)}{l^3} & 0\\ 0 & R_d(s)+\dfrac{2E_s w^3C(k_1)}{l^3}+\dfrac{2E_s wC(k_2)}{l}\end{bmatrix},\\
\mathbf{a}^{-}&=\begin{bmatrix}-\dfrac{\imath E_s w^3S(k_2)}{l^2} & \dfrac{\imath E_s w^3S(k_1)}{l^2}\end{bmatrix}^T,\\
\mathbf{a}^{+}&=\begin{bmatrix}\dfrac{\imath E_s w^3S(k_2)}{l^2} & -\dfrac{\imath E_s w^3S(k_1)}{l^2}\end{bmatrix},\\
b&=R_\theta(s)+\frac{E_s w^3}{3l}\left[2+C(k_1)+C(k_2)\right],
\end{aligned} \tag{4.12}$$

where the auxiliary trigonometric functions $C(k_i)=1-\cos(k_i a)$ and $S(k_i)=\sin(k_i a)$, with i = 1,2. The analysis of the dispersion spectrum can be focused on the first Brillouin zone $\mathcal{B}$ of the bidimensional $\mathbf{k}$ -domain, which is defined $\mathcal{B}=\{\mathbf{k}:k_i a=\tilde{k}_i\in[-\pi,\pi]\}$ in non-dimensional form for the quadrilateral metamaterial. Within this square zone, the complex-valued spectrum can be synthetically illustrated by determining the dispersion curves along particular propagation directions. Specifically, the real and imaginary parts of all the dispersion curves can be described over the closed boundary $\partial\mathcal{B}$ of the triangular subdomain $\mathcal{B}_1\subset\mathcal{B}$, limited by the vertices $\mathrm{B}_1,\mathrm{B}_2,\mathrm{B}_3$ (pointed by the non-dimensional wavevectors $\tilde{\mathbf{k}}_1=(0\ \ 0)^T$, $\tilde{\mathbf{k}}_2=(0\ \ \pi)^T$, $\tilde{\mathbf{k}}_3=(\pi\ \ \pi)^T$ respectively). Accordingly, the boundary $\partial\mathcal{B}$ is spanned by the non-dimensional curvilinear abscissa ξ, varying in the range $[0,2\pi+\sqrt{2}\pi]$.

4.3.1. Complex-valued dispersion spectra

Focusing first on the lowest (first) order approximation of the relaxation functions, the dispersion curves related to an ideal metamaterial $\mathcal{M}$ are reported in Figure 4. The particular mechanical parameters are ideally selected to be $\tilde{R}=R/a=1/5$, $\tilde{w}=w/a=3/50$, $\tilde{r}=r/a=1/10$, $\tilde{J}_1=J_1/(M_1a^2)=\tilde{R}-\tilde{R}\tilde{w}+\frac{1}{2}\tilde{w}^2$, $\tilde{M}_2=M_2/M_1=\tilde{\rho}\tilde{r}^2/(2\tilde{R}\tilde{w}-\tilde{w}^2)$, $\tilde{J}_2=J_2/(M_1a^2)=\frac{1}{2}\tilde{\rho}\tilde{M}_2\tilde{r}^2$ and resonator-to-ring mass density ratio $\tilde{\rho}=10$. Dispersion curves related to visco-elastically damped resonators ($\tilde{k}_{de}=35/100$, $\tilde{k}_{\theta e}=16/2500$, $\beta=\beta_d=\beta_\theta=5$, $\tilde{t}_r=1/10$) and undamped resonators ($\beta=\beta_d=\beta_\theta=0$ or $\tilde{t}_r\to\infty$) are illustrated.

The real and imaginary parts of the complex frequency $\tilde{s}$, which can be referred to as wave *damping* and wave *frequency* in the following, are related to the propagation in space and the attenuation in time of the mono-harmonic wave traveling through the metamaterial. Negative real parts of the complex frequency correspond to time exponentially decaying amplitudes of the propagating wave. As expected, the undamped metamaterial shows a dispersion diagram composed by six purely imaginary dispersion curves, corresponding to waves propagating without attenuation (Figure 4.3a). A full large-amplitude band gap separates the three low-frequency dispersion curves from the three high-frequency dispersion curves (Figure 4.3b). It can be verified that the low-frequency curves are associated to waveforms systematically localized in the ring (*ring polarization*), with quasi-static contribution of the resonator. Differently, the high-frequency curves are associated to waveforms mainly localized in the resonator (*resonator polarization*). Looking at the damped metamaterial, the dispersion spectrum possesses six complex-valued curves (Figure 4.3a). The three curves in the low frequency range can be conventionally referred to as spectral branches of *quasi-propagation*, since they are dominated by the imaginary part

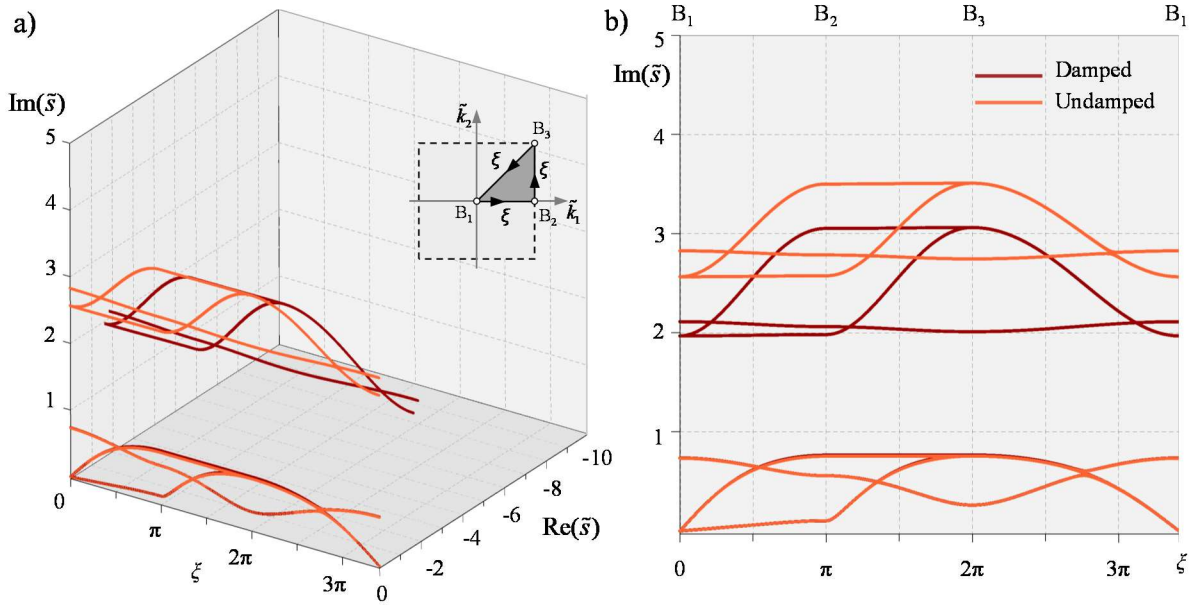

Figure 4.3 Complex-valued dispersion spectrum of the metamaterial $\mathcal{M}$ corresponding to the first-order approximation of the relaxation functions: (a) wave frequency and wave damping, (b) wave frequency.

of the complex frequency, with minimal participation of the real part. It can be verified that the slight dynamic interaction between the ring and the resonator, caused by the ring polarization, reduces the attenuation offered by the viscoelastic coupling. Consequently, no appreciable differences can be recognized in the low-frequency spectra of the damped and undamped metamaterials. The remaining three curves in the high frequency range can be conventionally referred to as spectral branches of *strong-attenuation*, since they are significantly contributed by the real part of the complex frequency. It can be verified that the strong ring-resonator interaction caused by the resonator polarization increases the attenuation offered by the viscoelastic coupling. As important remark, the strong frequency reduction caused by the viscoelastic coupling in the damped metamaterial causes a marked decrement in the band gap amplitude (Figure 4.3b).

Considering a second-order approximation of the relaxation functions, the approximating series introduce $\tilde{s}^2$-proportional contributions to the polynomial eigenvalue problem, which can modify the second $\tilde{s}$-power terms deriving from the inertia forces. The corresponding dispersion curves are shown in Figure 4.4. As first remark, the negative real part of all the dispersion curves tends to decrease, causing a small increment of the damping in the propagating waves (Figure 4.4a). As major remark, the essential difference with respect to the first-order approximation is related to the high-frequency dispersion curves, which concur to determine a pass band with significantly larger amplitude (Figure 4.4b). The amplitude enlargement also slightly reduces the band gap between the high frequency and the low frequency branches of the spectrum. As complementary remark, it can be noted that the limit of long wavelengths $(\xi = 0)$ is a triple frequency point for the high-frequency dispersion curves.

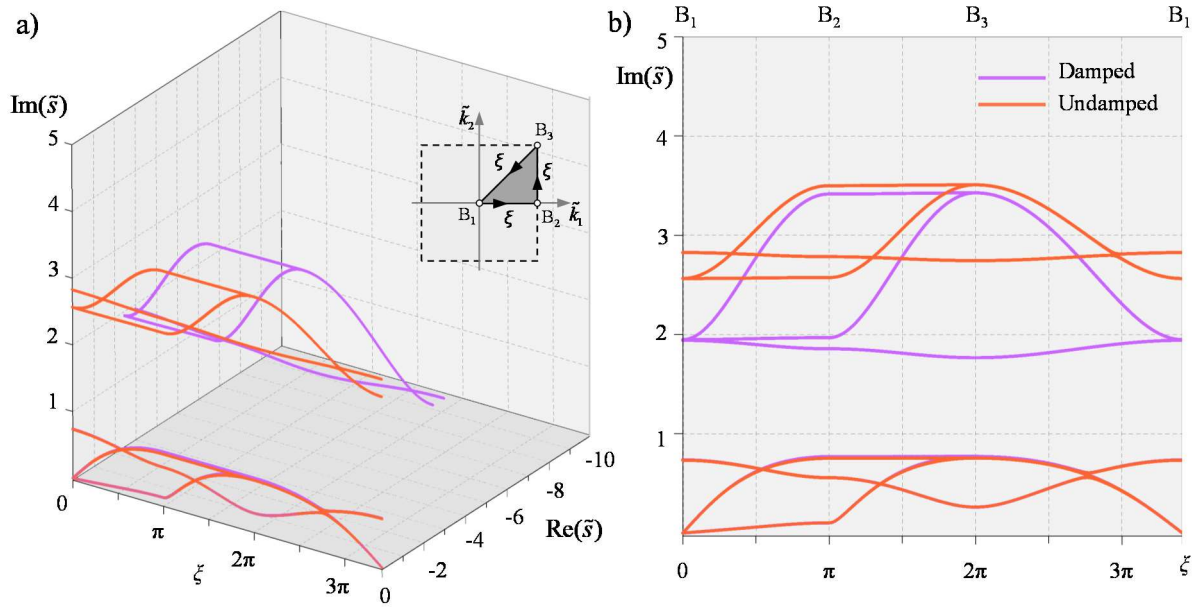

Figure 4.4 Complex-valued dispersion spectrum of the metamaterial $\mathcal{M}$ corresponding to the second-order approximation of the relaxation functions: (a) wave frequency and wave damping, (b) wave frequency.

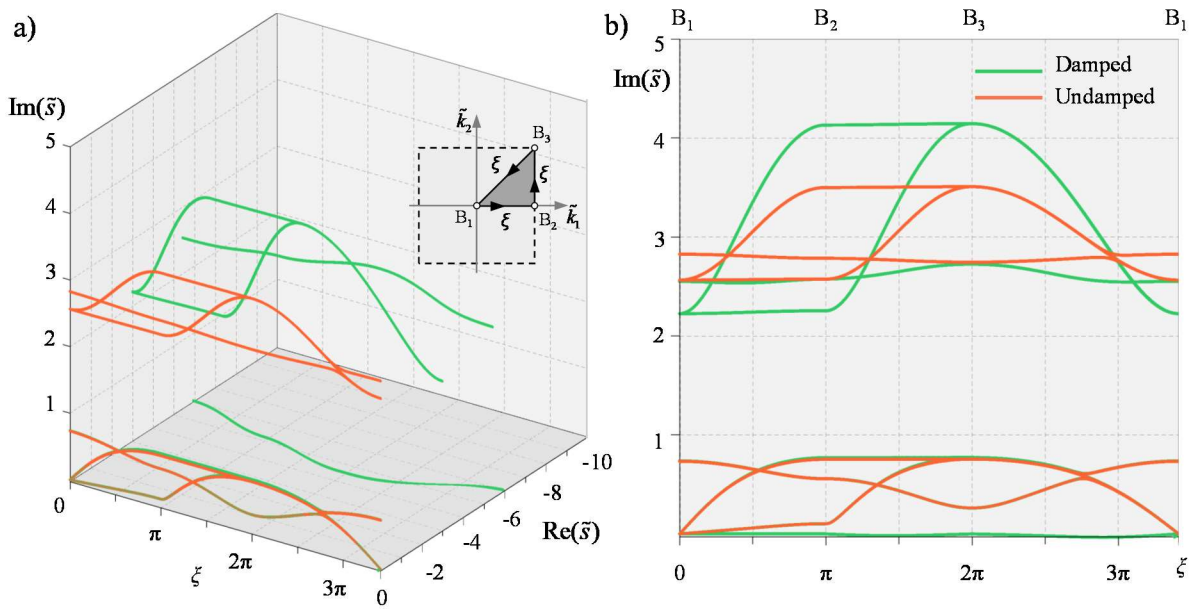

Figure 4.5 Complex-valued dispersion spectrum of the metamaterial $\mathcal{M}$ corresponding to the third-order approximation of the relaxation functions: (a) wave frequency and wave damping, (b) wave frequency.

Considering a third-order approximation of the relaxation functions, the approximating series introduce new $\tilde{s}^3$-proportional contributions to the polynomial eigenvalue problem. The corresponding dispersion curves are shown in Figure 4.5. As first remark, the real part of all the dispersion curves shows a further decrement (damping increment) with respect to the second order approximation (Figure 4.5a). As major remark, the order augment of the polynomial eigenvalue problem determines the emergence of an additional real-valued dispersion curve of the spectrum. Consequently, although the number of non-zero

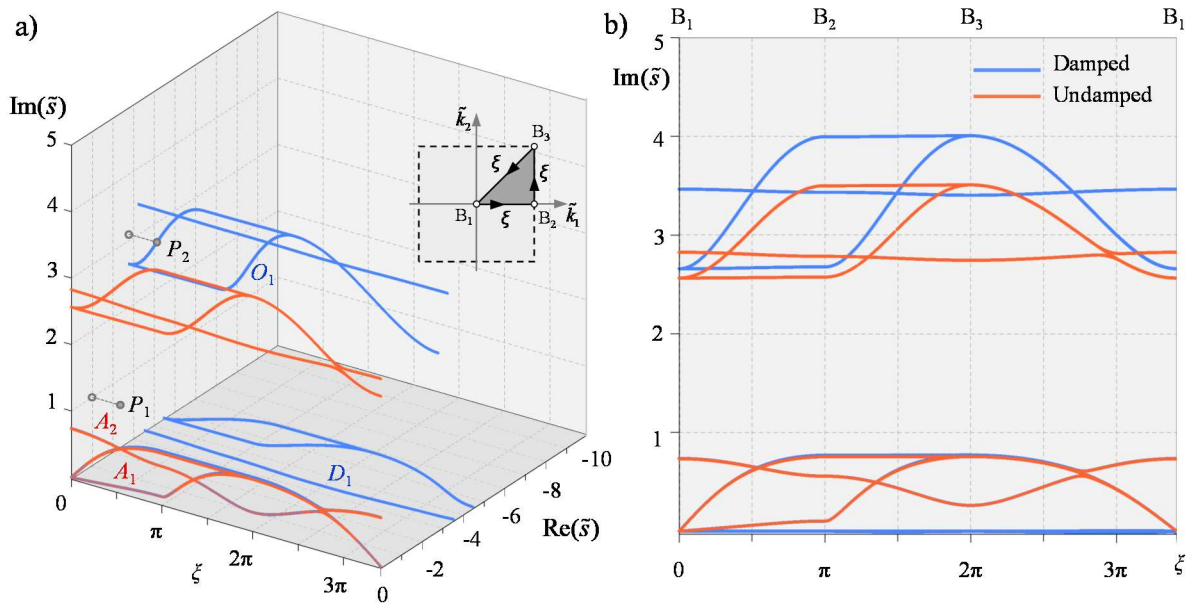

Figure 4.6 Complex-valued dispersion spectrum of the metamaterial $\mathcal{M}$ corresponding to the exact relaxation functions: (a) wave frequency and wave damping, (b) wave frequency.

wave frequencies remains unchanged, the number of branches in the complex-valued dispersion spectrum exceeds the total number of degrees-of-freedom in the periodic cell. It is worth remarking that the new real-valued dispersion curve corresponds to waves non-propagating in space but highly damped in time. As minor remark, the pass band associated to the high-frequency dispersion curves is shifted to a higher frequency range and also increases in amplitude with respect to the second order approximation (Figure 4.5b).

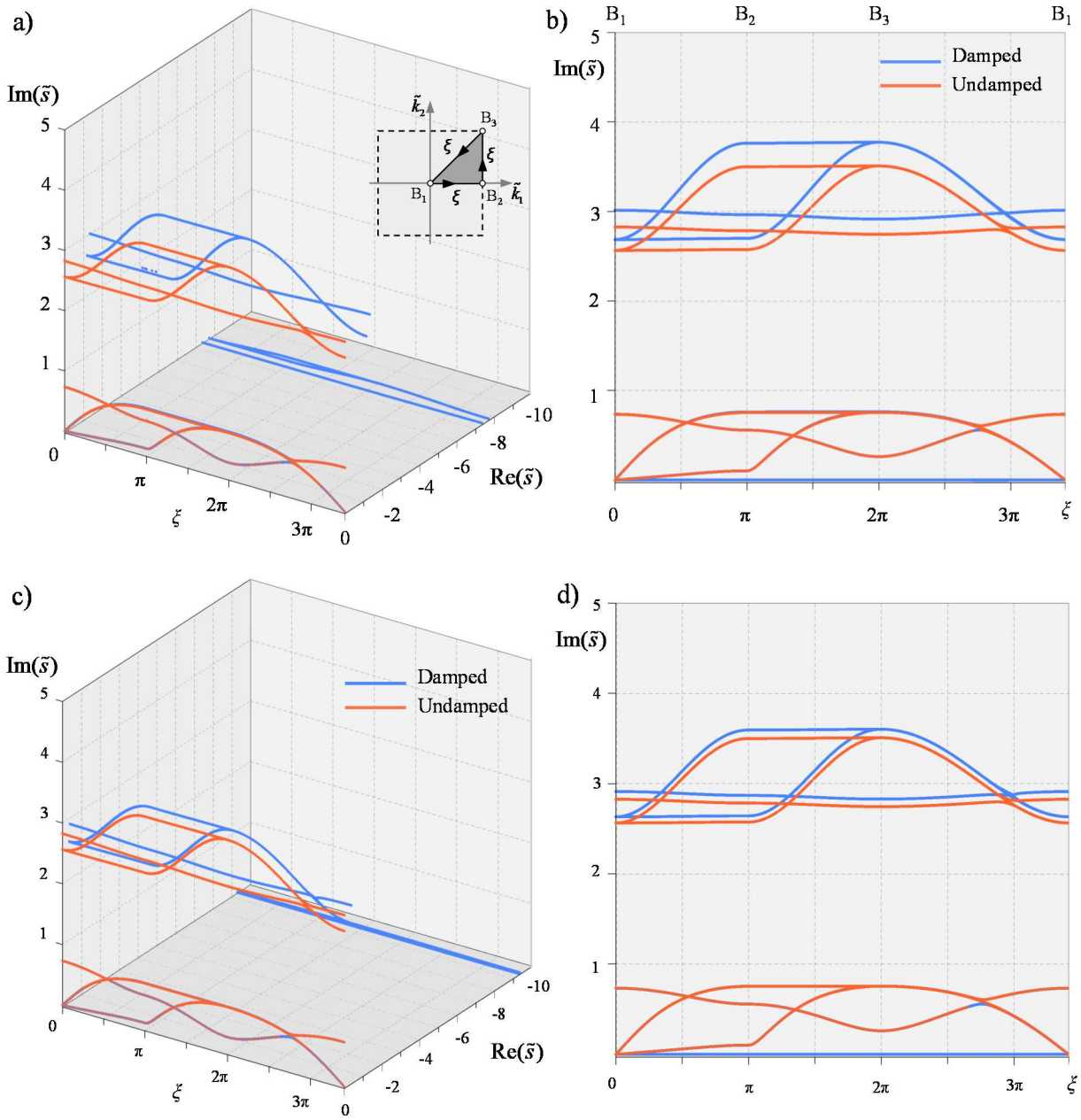

Figure 4.7 Complex-valued dispersion spectrum of the metamaterial $\mathcal{M}$ with low viscosity ratio corresponding to the exact relaxation functions: (a) wave frequency and wave damping ($\beta = 3$), (b) wave frequency ($\beta = 3$), (c) wave frequency and wave damping ($\beta = 1$), (d) wave frequency ($\beta = 1$).

Finally, considering the exact relaxation functions, the wave dispersion properties are governed by a rational eigenvalue problem. The corresponding dispersion curves are shown in Figure 4.6. As for the third-order approximation, the number of spectrum branches exceeds the total number of degrees-of-freedom in the periodic cell. Specifically, the spectrum shows three real-valued dispersion curve corresponding to non-propagating damped waves (Figure 4.6a). In the comparison with the undamped metamaterial, it can be clearly recognized that the exact treatment of the viscoelastic coupling determines a slight amplification of the band gap separating the low-frequency and the high-frequency dispersion curve (Figure 4.6b). The relevance of this key observation is principally related to the qualitative and quantitative comparison with the approximate (first-order) treatment of the viscoelastic coupling. Indeed, from the quantitative viewpoint, the classical first-order approximation is found to strongly underestimate the band gap amplitude. Furthermore, from the qualitative viewpoint, it also returns a band gap reduction with respect to the undamped metamaterial. As complementary remark, the amplitude of the high-frequency pass band is also amplified. For the sake of completeness, a wide parametric analyses has been performed to assess the effect of different viscosity ratios on the exact dispersion spectrum. To exemplify the results, the dispersion spectrum related to a smaller viscosity ratio ($\beta = 3$ and $\beta = 1$) is shown in Figure 4.7. As major remark, the lower viscosity causes a systematic augment of the negative real part (damping reduction) for all the dispersion curves associated to propagating waves. On the contrary, the lower viscosity systematically shifts the dispersion curves associated to non-propagating waves to a lower real value range (Figure 4.7a,c, Figure 4.8). Smaller viscosity ratios also tends to reduce the amplitudes of the band gap (Figure 4.7b,d).

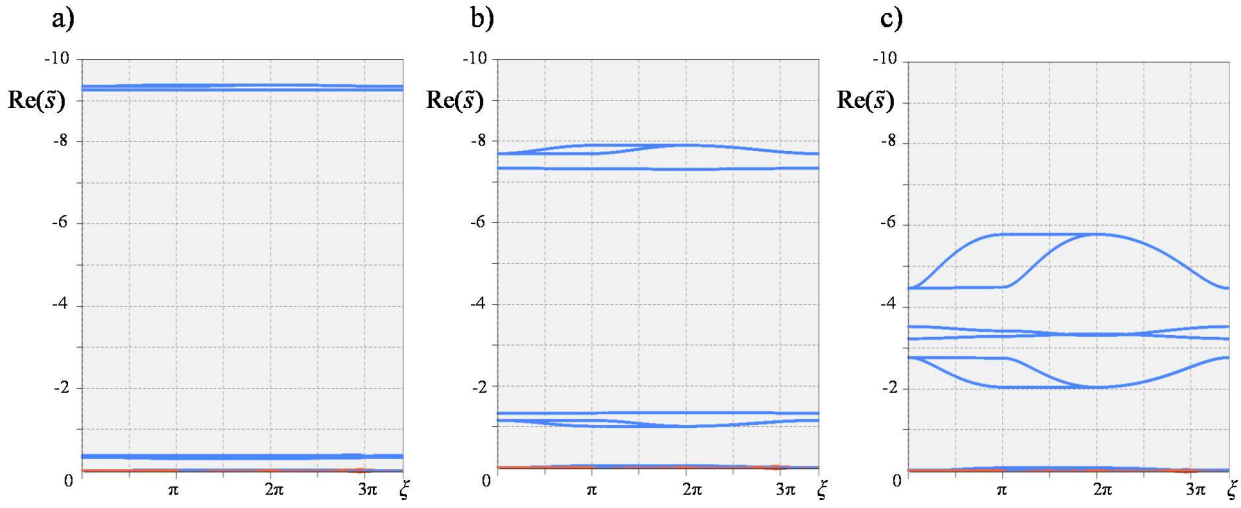

Figure 4.8 Complex-valued dispersion spectrum of the metamaterial $\mathcal{M}$ with viscosity ratio corresponding to the exact relaxation functions: (a) wave damping ($\beta = 1$), (b) wave damping ($\beta = 3$), (c) wave damping ($\beta = 5$).

4.4. Asymptotic approximation

The perturbation methods represent an efficient alternative to the numerical solution of the eigenproblem governing the wave dispersion. Each complex eigenvalue $\Lambda_h(\mathbf{k}) = s_h(\mathbf{k})$ can be regarded

as one of the zeroes (with multiplicity m_h) of the characteristic function $Q(\Lambda,\mathbf{k}) = \det(\mathbf{C}(\Lambda,\mathbf{k}))$.

The perturbation technique is described in paragraph 3.2.2 expressing the non-dimensional characteristic function in the form $F(\lambda, z)$ where $\lambda = \tilde{s}$ is the non-dimensional eigenvalue.

Table 4.1 reports the solution scheme required to achieve a fourth-order approximation (3.26) of all fifteen eigenvalues by employing the vertices B_1 (corresponding to $\xi^* = 0$) and B_2 (corresponding to $\xi^* = \pi$) as reference points to start the perturbation analysis.

Table 4.1 Solution scheme of the perturbation equations up to the fourth order.

$\xi^* = 0$									$\xi^* = \pi$					
m	λ^*	z^1	z^2	z^3	z^4	z^5	z^6	z^7	m	λ^*	z^1	z^2	z^3	z^4
4	$\lambda^*_{1,2,3,4}$	-	-	-	$\dot{\lambda}_1$	$\ddot{\lambda}_1$	$\dddot{\lambda}_1$	$\ddddot{\lambda}_1$	1	λ^*_1	$\dot{\lambda}_1$	$\ddot{\lambda}_1$	$\dddot{\lambda}_1$	$\ddddot{\lambda}_1$
					$\dot{\lambda}_2$	$\ddot{\lambda}_2$	$\dddot{\lambda}_2$	$\ddddot{\lambda}_2$	1	λ^*_2	$\dot{\lambda}_2$	$\ddot{\lambda}_2$	$\dddot{\lambda}_2$	$\ddddot{\lambda}_2$
					$\dot{\lambda}_3$	$\ddot{\lambda}_3$	$\dddot{\lambda}_3$	$\ddddot{\lambda}_3$	1	λ^*_3	$\dot{\lambda}_3$	$\ddot{\lambda}_3$	$\dddot{\lambda}_3$	$\ddddot{\lambda}_3$
					$\dot{\lambda}_4$	$\ddot{\lambda}_4$	$\dddot{\lambda}_4$	$\ddddot{\lambda}_4$	1	λ^*_4	$\dot{\lambda}_4$	$\ddot{\lambda}_4$	$\dddot{\lambda}_4$	$\ddddot{\lambda}_4$
2	$\lambda^*_{5,6}$	-	$\dot{\lambda}_{5,6}$	-	$\ddot{\lambda}_5$	$\dddot{\lambda}_5$	$\ddddot{\lambda}_5$	…	1	λ^*_5	$\dot{\lambda}_5$	$\ddot{\lambda}_5$	$\dddot{\lambda}_5$	$\ddddot{\lambda}_5$
					$\ddot{\lambda}_6$	$\dddot{\lambda}_6$	$\ddddot{\lambda}_6$	…	1	λ^*_6	$\dot{\lambda}_6$	$\ddot{\lambda}_6$	$\dddot{\lambda}_6$	$\ddddot{\lambda}_6$
2	$\lambda^*_{7,8}$	-	$\dot{\lambda}_{7,8}$	-	$\ddot{\lambda}_7$	$\dddot{\lambda}_7$	$\ddddot{\lambda}_7$	…	1	λ^*_7	$\dot{\lambda}_7$	$\ddot{\lambda}_7$	$\dddot{\lambda}_7$	$\ddddot{\lambda}_7$
					$\ddot{\lambda}_8$	$\dddot{\lambda}_8$	$\ddddot{\lambda}_8$	…	1	λ^*_8	$\dot{\lambda}_8$	$\ddot{\lambda}_8$	$\dddot{\lambda}_8$	$\ddddot{\lambda}_8$
2	$\lambda^*_{9,10}$	-	$\dot{\lambda}_{9,10}$	-	$\ddot{\lambda}_9$	$\dddot{\lambda}_9$	$\ddddot{\lambda}_9$	…	1	λ^*_9	$\dot{\lambda}_9$	$\ddot{\lambda}_9$	$\dddot{\lambda}_9$	$\ddddot{\lambda}_9$
					$\ddot{\lambda}_{10}$	$\dddot{\lambda}_{10}$	$\ddddot{\lambda}_{10}$	…	1	λ^*_{10}	$\dot{\lambda}_{10}$	$\ddot{\lambda}_{10}$	$\dddot{\lambda}_{10}$	$\ddddot{\lambda}_{10}$
1	λ^*_{11}	$\dot{\lambda}_{11}$	$\ddot{\lambda}_{11}$	$\dddot{\lambda}_{11}$	$\ddddot{\lambda}_{11}$	…	…	…	1	λ^*_{11}	$\dot{\lambda}_{11}$	$\ddot{\lambda}_{11}$	$\dddot{\lambda}_{11}$	$\ddddot{\lambda}_{11}$
1	λ^*_{12}	$\dot{\lambda}_{12}$	$\ddot{\lambda}_{12}$	$\dddot{\lambda}_{12}$	$\ddddot{\lambda}_{12}$	…	…	…	1	λ^*_{12}	$\dot{\lambda}_{12}$	$\ddot{\lambda}_{12}$	$\dddot{\lambda}_{12}$	$\ddddot{\lambda}_{12}$
1	λ^*_{13}	$\dot{\lambda}_{13}$	$\ddot{\lambda}_{13}$	$\dddot{\lambda}_{13}$	$\ddddot{\lambda}_{13}$	…	…	…	1	λ^*_{13}	$\dot{\lambda}_{13}$	$\ddot{\lambda}_{13}$	$\dddot{\lambda}_{13}$	$\ddddot{\lambda}_{13}$
1	λ^*_{14}	$\dot{\lambda}_{14}$	$\ddot{\lambda}_{14}$	$\dddot{\lambda}_{14}$	$\ddddot{\lambda}_{14}$	…	…	…	1	λ^*_{14}	$\dot{\lambda}_{14}$	$\ddot{\lambda}_{14}$	$\dddot{\lambda}_{14}$	$\ddddot{\lambda}_{14}$
1	λ^*_{15}	$\dot{\lambda}_{15}$	$\ddot{\lambda}_{15}$	$\dddot{\lambda}_{15}$	$\ddddot{\lambda}_{15}$	…	…	…	1	λ^*_{15}	$\dot{\lambda}_{15}$	$\ddot{\lambda}_{15}$	$\dddot{\lambda}_{15}$	$\ddddot{\lambda}_{15}$

Legend: "-" = undetermined, "…" = higher-order unknows

The mechanical parameters used for exact dispersion spectrum illustrated in Figure 4.5 are selected to obtain the approximate dispersion curves in the interval $\xi = [0, \pi]$. As an example, the complex *eigensensitivities* of the fourth-order approximate λ_1 and λ_2 are reported in Table 4.2 as explicit functions of the non-dimensional mechanical parameters, where $C_1 = 2\tilde{R} - 1$, $C_2 = (-\tilde{w}^2 + 2\tilde{R}\tilde{w} + \tilde{r}^2\tilde{\rho})\tilde{w}$, $C_3 = -(7/2)\tilde{w}^2 + 2\tilde{w} - \tilde{\rho}\tilde{r}^2$, $C_4 = 3\tilde{w}^3 - \tilde{w}^2 - \tilde{w} + \tilde{\rho}\tilde{r}^2$, $C_5 = -(3/4)\tilde{w}^4 + (1/2)\tilde{w} + (3/4)\tilde{\rho}\tilde{r}^2\left(\tilde{r}^2 - 2/3\right)$.

The comparison between the exact (continuous line) and approximate (dots) dispersion curves, with $\mathrm{Im}(\tilde{s}) \geq 0$, are shown in Figure 4.9 and 4.10, chosen the vertices B_1 (*left approximation* for $\xi^* = 0$) and B_2 (*right approximation* for $\xi^* = \pi$) as reference points to start the perturbation analysis, respectively. The fourth-order approximate solutions well-match the real and the imaginary part of all dispersion curves among the reference point and $\xi = \pi/2$, but some curves are not good approximations in the entire interval $\xi = [0, \pi]$.

Table 4.2 *Eigensensitivities* of the fourth-order approximate eigenvalues λ_1 and λ_2.

$\xi^* = 0$	
$\lambda(z)$	*eigensensitivities*
λ_1	$\dot{\lambda}_1 = \dfrac{\sqrt{2}}{2}\dfrac{\tilde{w}\sqrt{\pi C_1 C_2}}{\pi C_1^2 C_2}$
	$\ddot{\lambda}_1 = 0$
	$\dddot{\lambda}_1 = -\dfrac{1}{96}\dfrac{\sqrt{2}\tilde{w}^2\left\{\left[\tilde{w}\tilde{R}^3 + C_3\tilde{R}^2 + C_4\tilde{R} + C_5\right]\dfrac{C_1^3 C_2 \tilde{k}_{de} - 3\tilde{r}^4\tilde{w}^3\tilde{\rho}^2}{16}\right\}}{\tilde{k}_{de} C_1^4 C_2^2\sqrt{\pi C_1 C_2 \tilde{w}}}$
	$\ddddot{\lambda}_1 = -\dfrac{1}{8}\dfrac{\tilde{k}_d\tilde{r}^4\tilde{w}^6\tilde{t}_r\,\tilde{\rho}^2}{\pi C_1^6 C_2^3 \tilde{k}_{de}^{\ 2}}$
λ_2	$\dot{\lambda}_2 = \dfrac{\sqrt{\pi C_1 C_2 \tilde{w}}}{\pi C_1 C_2}$
	$\ddot{\lambda}_2 = 0$
	$\dddot{\lambda}_2 = -\dfrac{1}{3}\dfrac{\tilde{w}\left(\dfrac{1}{8}\tilde{k}_{de} C_1 C_2^2 - \dfrac{3}{2}\tilde{r}^4\tilde{w}\tilde{\rho}^2\right)}{\tilde{k}_{de} C_1 C_2^2\sqrt{\pi C_1 C_2 \tilde{w}}}$
	$\ddddot{\lambda}_2 = -\dfrac{1}{2}\dfrac{\tilde{k}_d\tilde{r}^4\tilde{w}^2\tilde{t}_r\,\tilde{\rho}^2}{\pi C_1^2 C_2^3 \tilde{k}_{de}}$

The mismatches can be significantly reduced by properly combining the left and right companion approximations, conventionally referred to as λ_i^- and λ_i^+ in the following. Among the others, a suited possibility is to adopt the linear and weighted combination

$$\lambda_i^{\mp} = w^- \lambda_i^- + w^+ \lambda_i^+, \qquad \text{with} \quad w^- + w^+ = 1, \tag{4.13}$$

where w^- and w^+ are ξ-dependent weighting functions that attain the boundary values $w^- = 1$, $w^+ = 0$ (at $\xi = 0$) and $w^- = 0$, $w^+ = 1$ (at $\xi = \pi$). Therefore the weight of each approximation function attains a maximum at its own reference point, while it monotocally decreases up to a minimum at the reference point of the companion function. Each combination $\lambda_i^{\mp}$ (for $i = 1...15$) is built by adopting the highly-adaptable pair of trascendental weighting functions

$$\begin{aligned} w^- &= \frac{1}{2} - \frac{\tanh(\gamma(2\xi - \pi))}{2\tanh(\gamma\pi)} \\ w^+ &= \frac{1}{2} + \frac{\tanh(\gamma(2\xi - \pi))}{2\tanh(\gamma\pi)}, \end{aligned} \tag{4.14}$$

where the parameter γ governs the higher (small γ - values) or lower (larger γ -values) smoothness of the transition from unity to zero across the range $\xi = [0, \pi]$.

The weighted combination is reported in Figure 4.11 for $\gamma = 2$. A good agreement among the exact and the approximate solutions can be observed except around $\xi = \pi / 2$. For more satisfying result, the perturbation technique can be also applied by using $\xi = \pi / 2$ as reference point to start the perturbation analysis.

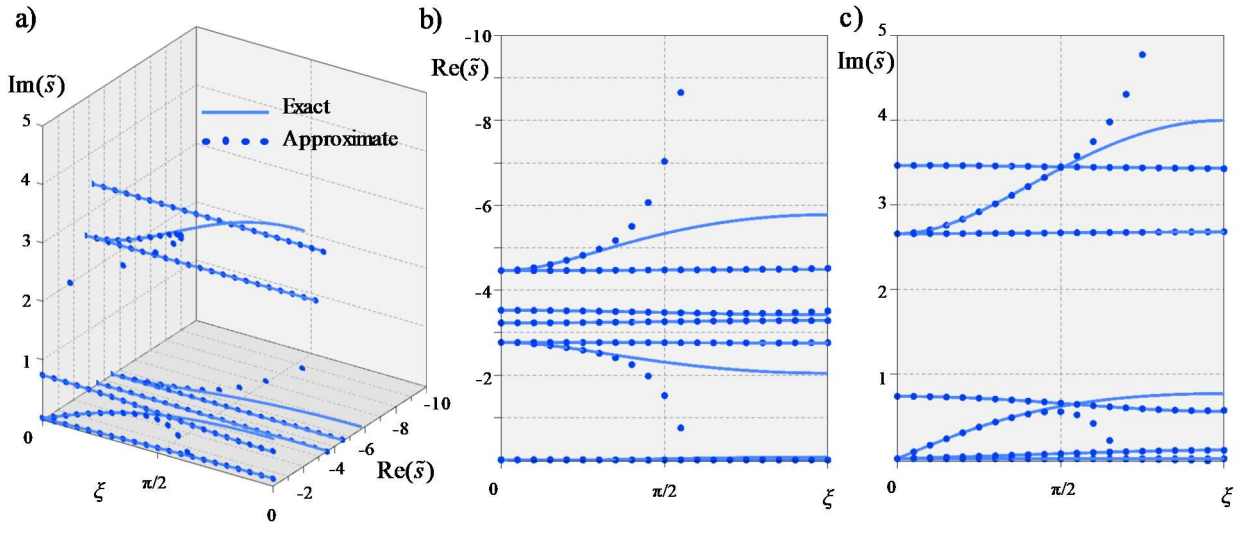

Figure 4.9 Complex-valued dispersion spectrum of the metamaterial $\mathcal{M}$: exact and approximate solutions for reference point $\xi^* = 0$: (a) wave frequency and wave damping, (b) wave damping (c) wave frequency.

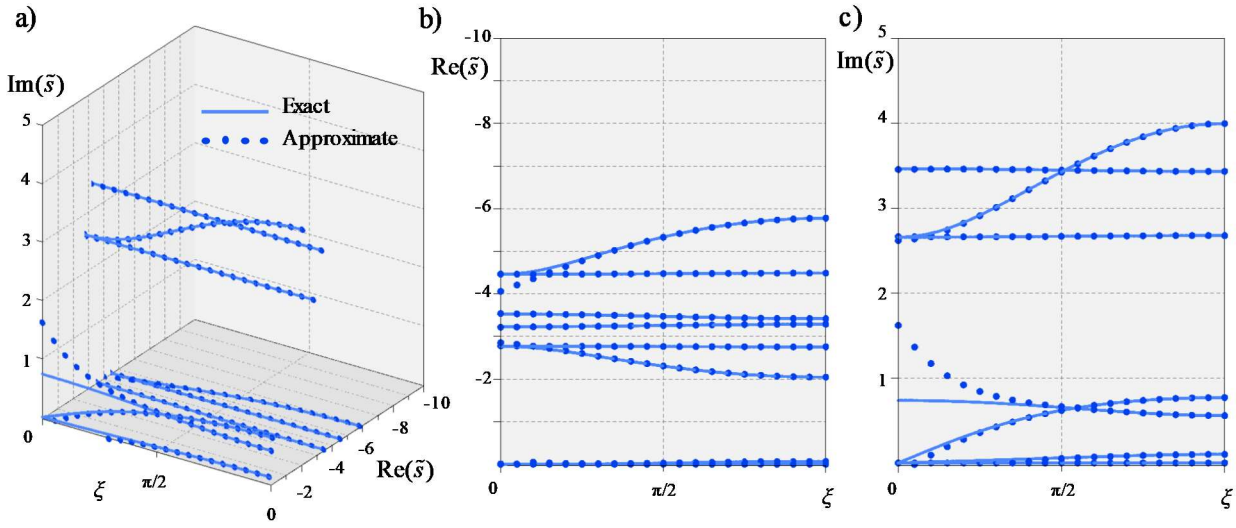

Figure 4.10 Complex-valued dispersion spectrum of the metamaterial $\mathcal{M}$: exact and approximate solutions for reference point $\xi^* = \pi$: (a) wave frequency and wave damping, (b) wave damping (c) wave frequency.

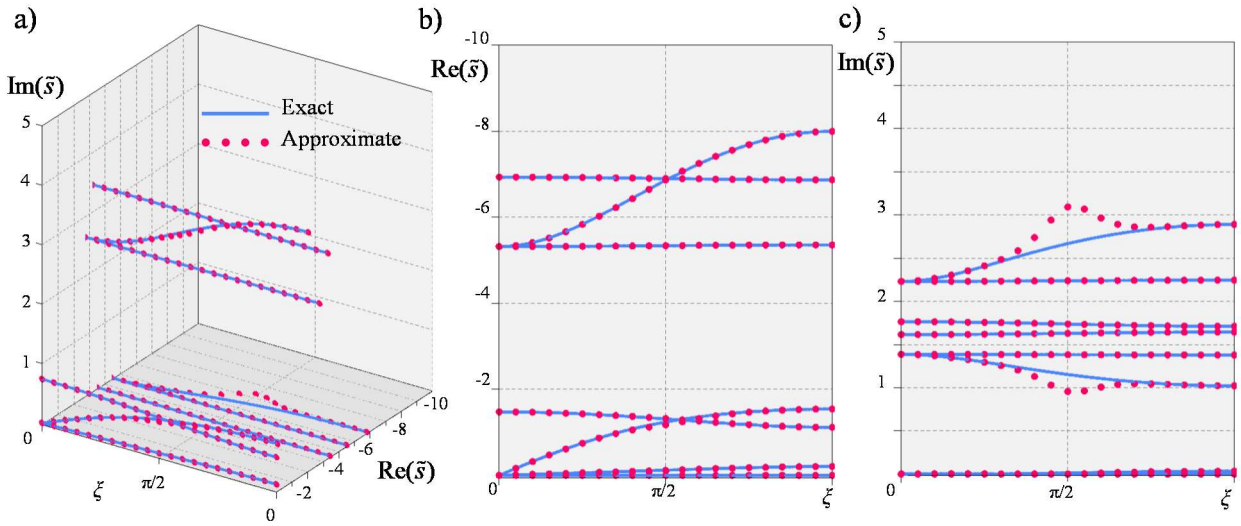

Figure 4.11 Complex-valued dispersion spectrum of the metamaterial $\mathcal{M}$: exact versus matched approximate solutions: (a) wave frequency and wave damping, (b) wave damping (c) wave frequency.

4.5. Forced wave propagation

For time-harmonic forced waves, the generalized external forces applied at the generic ring pointed by the position vector $\mathbf{x}_n$ can be expressed as $\mathbf{f}_n = \mathbf{p}\, H(t)\exp(St)\exp(\imath\mathbf{K}\cdot\mathbf{x}_n)$ and $g_n = m\, H(t)\exp(St)\exp(\imath\mathbf{K}\cdot\mathbf{x}_n)$, where $H(t)$ is the unit step function, $\mathbf{p}$ and m are time-independent force amplitudes, S is the complex-valued forcing frequency and $\mathbf{K}$ is the real-valued forcing wavevector. Since the coordinate origine can conveniently located at the centroid of the loaded ring

$(\mathbf{x}_n = \mathbf{0})$, the right-hand terms of the equations (4.1) governing the forced dynamics of the reference ring read

$$\begin{aligned} \mathbf{f}(S,t) &= \mathbf{p}\ H(t)\exp(St) \\ g(S,t) &= m\ H(t)\exp(St), \end{aligned} \tag{4.15}$$

where the real part of the complex-valued frequency S is assumed not null and negative in the general case, in order to account for generic, exponentially decaying external loads. Consequently, since the linear algebraic equations (4.5) have been written in the matrix form $\mathbf{C}(\mathbf{k},s)\hat{\mathbf{U}} = \hat{\mathbf{F}}(S,s)$, the right-hand term $\hat{\mathbf{F}}(S,s) = \left(\hat{\mathbf{f}}(S,s) \quad \hat{g}(S,s) \quad \mathbf{0} \quad 0\right)^T$ is obtained by applying the bilateral Laplace transform to equation (4.15), yielding

$$\begin{aligned} \hat{\mathbf{f}}(S,s) &= \frac{\mathbf{p}}{s-S} \\ \hat{g}(S,s) &= \frac{m}{s-S}, \end{aligned} \tag{4.16}$$

where $s = S$ can be easily recognized as a simple pole of the transformed external forces.

Assigned a generic forcing frequency S, the stationary lattice response is described by the transformed displacement vector in the Bloch-Laplace space

$$\hat{\mathbf{U}}(S,\mathbf{k},s) = \mathbf{D}(\mathbf{k},s)\hat{\mathbf{F}}(S,s), \tag{4.17}$$

where the six-by-six matrix $\mathbf{D}(\mathbf{k},s) = \mathbf{C}(\mathbf{k},s)^{-1}$ is also known as dynamic *compliance* matrix. According to this formulation, the roots of the characteristic equations $\det\mathbf{C}(\mathbf{k},s) = 0$, that define the Floquet-Bloch spectrum of the metamaterial, are expected to determine poles in the components of the compliance matrix $\mathbf{D}(\mathbf{k},s)$. From the mechanical viewpoint, the forced response amplitude is essentially determined by the relative position between these spectral poles and the poles of the transformed external forces.

Therefore, accordingly with the procedure proposed by Slepyan (2012), (and also in Kunin 2012; Movchan and Slepyan 2014), the transformed displacement vector $\hat{\mathbf{U}}(S,\mathbf{k},s)$ can be antitransformed by the inverse space-dicrete Fourier transform, leading to the transformed displacement vector $\hat{\mathbf{U}}(S,s)$ of the *n*-th ring in the Laplace space. The stationary lattice response is finally expressed in the time-dependent complex-valued displacement vector $\mathbf{U}(S,t)$ by applying the inverse bilateral Laplace transform

$$\mathbf{U}(S,t) = \mathcal{L}^{-1}\left[\hat{\mathbf{U}}(S,s)\right] = \frac{1}{2\pi\,\imath}\int_{r-\imath\,\infty}^{r+\imath\,\infty}\hat{\mathbf{U}}(S,s)\exp(st)\,\mathrm{d}s, \qquad r \in \mathbb{R}, \tag{4.18}$$

which is evaluated as $\mathbf{U}(S,t) = \sum R\left(\hat{\mathbf{U}}(S,s)\exp(st)\right)$, where R stands for the residual of $\hat{\mathbf{U}}(S,s)\exp(st)$ and the sum is extended to all the poles of $\hat{\mathbf{U}}(S,s)$.

4.5.1. Compliance matrix

In order to determine and discuss the forced response of the particular metamaterial $\mathcal{M}$, the dynamic

compliance matrix can be analyzed first. The non-dimensional complex-valued component $\tilde{D}_{11}(\tilde{\mathbf{k}}_0,\tilde{s})=D_{11}(\tilde{\mathbf{k}}_0,\tilde{s})E_s$ is considered for a fixed non-dimensional wavevector $\tilde{\mathbf{k}}_0$. Selecting the particular wavevector $\tilde{\mathbf{k}}_0=(1\ 0)^T$, the loci of the null real and imaginary parts of the $\tilde{D}_{11}$-denominator (coincident with the $\tilde{\mathbf{C}}(\tilde{\mathbf{k}}_0,\tilde{s})$-determinant) are shown in Figure 4.12a (curves in blue-scale) in the plane of the real and imaginary part of the complex frequency $\tilde{s}$. In the general case, the crossing points of the loci do not identify points of polar singularities or poles for the dynamic compliance, since they can coincide with intersections between the continuous loci of the null real and null imaginary parts of the $\tilde{D}_{11}$-numerator (curves in red-scale). On the contrary, the poles for the dynamic compliance are identified by the few crossing points in which the denominator vanishes for non-null values of the numerator. These peculiar points are characteristic properties of the metamaterial and can be referred to as *complex resonance points*. For the particular $\tilde{D}_{11}$- component under investigation, three distinct resonance points can be recognized (marked by yellow circles). The magnitude of the complex-valued component $\tilde{D}_{11}(\tilde{\mathbf{k}}_0,\tilde{s})$ is found to rapidly but continuously grow up in the closeness of these points, approaching infinite values (Figure 4.12b). It can be remarked that the resonance points actually coincide with some of the $\tilde{s}$-values already identified by the dispersion function $\tilde{s}(\tilde{\mathbf{k}}_0)$ in the free vibration analysis. In particular, the resonance points can be associated to the first acoustic branch (point A_1), to one of the purely damping branches (point D_1), and to one of the optical branches (point O_1) of the complex-valued spectrum shown in Figure 4.6a. Similarly, resonance points associable to the same or some other branches of the metamaterial spectrum can be found for each component of the compliance matrix (Figure 4.13).

4.5.2. Forced response

Focusing on the transformed displacements of the metamaterial $\mathcal{M}$ under the effect of the external complex-valued exponentially decaying force $\hat{\mathbf{F}}(S_0,s)$ with fixed forcing frequency S_0, the wavevector $\tilde{\mathbf{k}}$-dependence of the complex-valued displacement component $\hat{U}_1$ is firstly analyzed.

According to equation (4.17), the displacement component is expressed by the linear combination $\hat{U}_1=D_{11}\hat{F}_1+D_{12}\hat{F}_2+D_{13}\hat{F}_3$. In Figure 4.13, the magnitude of the non-dimensional component $\tilde{\hat{U}}_1=\hat{u}_1\sqrt{E_s/(M_1 a)}$ is reported over the first square Brillouin zone $\mathcal{B}$ for the particular non-dimensional forcing frequency $\tilde{S}_0=3\imath$ and for unitary values of the non-dimensional force amplitudes. Choosing different values of the complex frequency $\tilde{s}$, strongly dissimilar values of the $\tilde{\hat{U}}_1$-magnitude are obtained, depending on whether the frequency $\tilde{s}$ falls within the stop band ($\tilde{s}_1=-1+\imath$, see Figure 4.14a) or close to a dispersion curve within a pass band ($\tilde{s}_2=-2.51+3.05\imath$, see Figure 4.14b). As first remark, the magnitude of the linear combination $\tilde{\hat{U}}_1$ is geometrically non-symmetric in the square Brillouin zone $\mathcal{B}$, in the general case. However, the cubic symmetry of the metamaterial microstructure can be verified to systematically determine doubly symmetric magnitudes of each term contributing to the linear combination. As major remark, when the frequency $\tilde{s}$ cannot resonate because it falls within the stop band ($\tilde{s}_1$ associated to point P_1 in Figure 4.6a), the metamaterial response does not show any evident peak

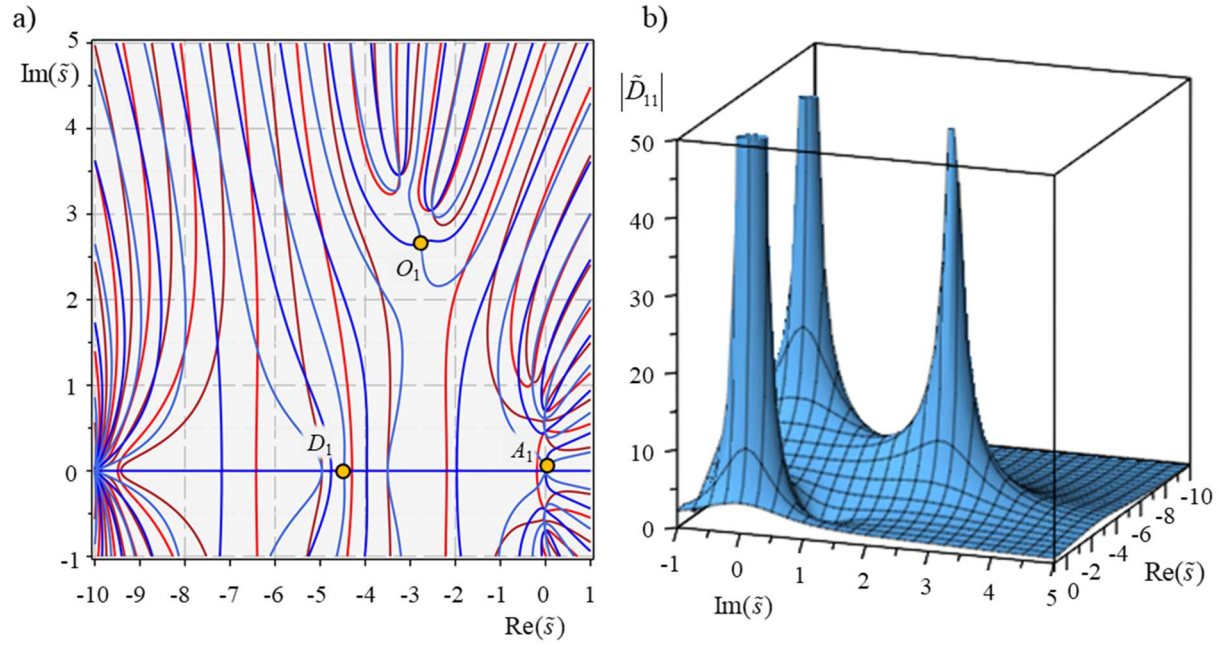

Figure 4.12 Compliance matrix of the particular metamaterial $\mathcal{M}$: (a) loci of the null real and null imaginary parts of the $\tilde{D}_{11}$ -numerator (curves in red-scale) and $\tilde{D}_{11}$ -denominator (curves in blue-scale), (b) magnitude of $\tilde{D}_{11}$.

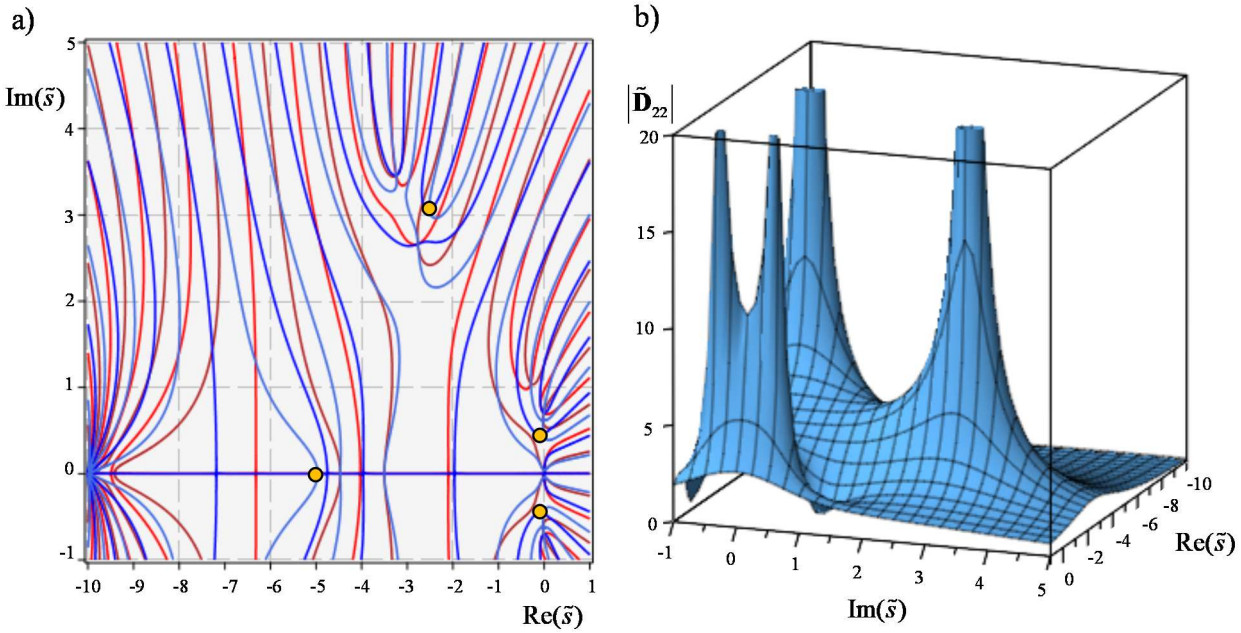

Figure 4.13 Compliance matrix of the particular metamaterial $\mathcal{M}$: (a) loci of the null real and null imaginary parts of the $\tilde{D}_{22}$ -numerator (curves in red-scale) and $\tilde{D}_{22}$ -denominator (curves in blue-scale), (b) magnitude of $\tilde{D}_{22}$.

in the entire Brillouin zone $\mathcal{B}$, independently of the wavevector $\tilde{\mathbf{k}}$ (Figure 4.14a). On the contrary, when the frequency falls within the pass band ($\tilde{s}_2$ associated to point P_2 in Figure 4.6a), the metamaterial

response can reach infinite-valued amplitudes, depending on whether the $(\tilde{s},\tilde{\mathbf{k}})$-combination lies on one of the dispersion curves (Figure 4.14b). Indeed, infinite-valued amplitudes are obtained for the frequency $\tilde{s}_2$ at resonance, that is in the closeness of the wavenumber $\tilde{k}_1 = 1$ (Figure 4.14c), which exactly corresponds to a dispersion curve of the spectrum (point P_2 in Figure 4.6a) and also to one of the singularities (point O_1) of the compliance matrix coefficient $\tilde{D}_{11}$ (shown in Figure 4.12 for $\tilde{\mathbf{k}}_0 = (1\ 0)^T$ or $\xi = 1$ in Figure 4.6a). On the contrary, if a slight variation is introduced to shift the frequency $\tilde{s}$ from

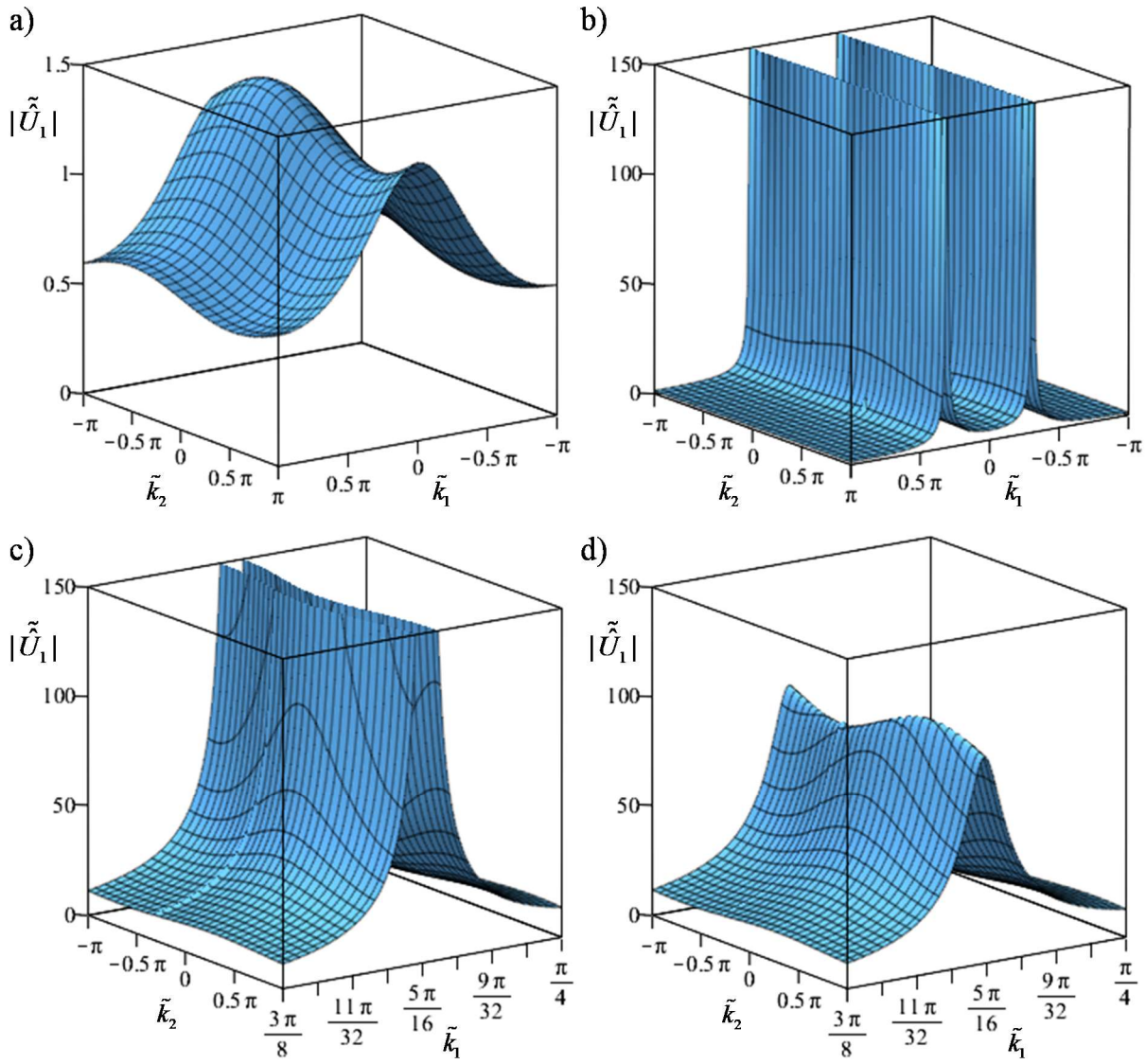

Figure 4.14 Magnitude of the displacement component $\tilde{\hat{U}}_1$ in the forced response of the particular metamaterial $\mathcal{M}$: (a) not-resonant complex frequency $\tilde{s}_1 = -1+\imath$ falling within the stopband, (b),(c) complex frequency $\tilde{s}_2 = -2.51+3.05\imath$ falling within the passband at resonance, (d) complex frequency $\tilde{s}_3 = 1.005\ \tilde{s}_2$ falling within the passband at quasi-resonance.

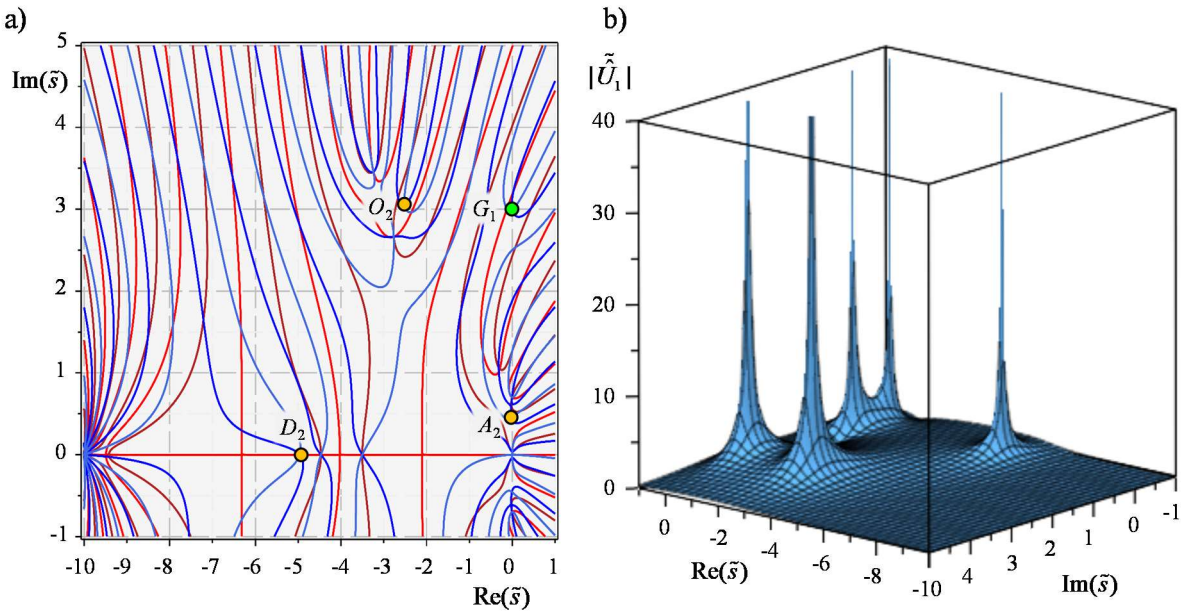

Figure 4.15 Response of the particular metamaterial $\mathcal{M}$ to non-resonant force ($\tilde{S}_1 = 3\imath$): (a) loci of the null real and null imaginary parts of the displacement component $\tilde{\hat{U}}_1$-numerator (curves in red-scale) and $\tilde{\hat{U}}_1$-denominator (curves in blue-scale), (b) magnitude of $\tilde{\hat{U}}_1$.

the dispersion curve (quasi-resonance), the metamaterial response reaches high but finite-valued amplitudes (see for instance the $\tilde{\hat{U}}_1$-magnitude shown in Figure 4.14d for $\tilde{s}_3 = 1.005\ \tilde{s}_2$).

Therefore, attention is focused on the frequency $\tilde{s}$-dependence of the complex-valued displacement component $\hat{U}_1$ of the metamaterial $\mathcal{M}$, which is again analyzed under the effect of the external complex- valued exponentially decaying force $\hat{\mathbf{F}}(S_0, s)$ with fixed forcing frequency S_0. In Figure 4.15, the non- dimensional component $\tilde{\hat{U}}_1$ is reported versus the real and imaginary parts of the frequency $\tilde{s}$ for the wavevector $\tilde{\mathbf{k}}_0 = (1\ 0)^T$, if the external forces are characterized by the forcing frequency $\tilde{S}_0 = 3\imath$ and unitary amplitudes. In this case the forcing frequency does not resonate with any of the metamaterial frequencies. The continuous loci of the null real and null imaginary parts of the $\tilde{\hat{U}}_1$-denominator are shown in Figure 4.15a (curves in blue-scale). All the crossing points of the loci that do not identify poles, because they also coincide with intersections between the continuous loci of the null real and null imaginary parts of the $\tilde{\hat{U}}_1$-numerator (curves in red-scale), are not significant. The remaining crossing points identify poles of the forced response. Among them, three poles (points D_2, O_2, A_2 marked by yellow dots) are characteristic properties of the metamaterial, while a fourth pole (point G_1 marked by green dot) is associated to the forcing frequency. It is worth noting that the $\hat{U}_1$-poles do not correspond exactly to the $\tilde{D}_{11}$-poles in Figure 4.12a, due to the second and third contributions to the linear combination $\hat{U}_1 = D_{11}\hat{F}_1 + D_{12}\hat{F}_2 + D_{13}\hat{F}_3$. The magnitude of the complex-valued component $\hat{U}_1$ is found to rapidly but continuously grow up in the closeness of all the four poles (and their complex conjugates), approaching infinite values (Figure 4.15b).

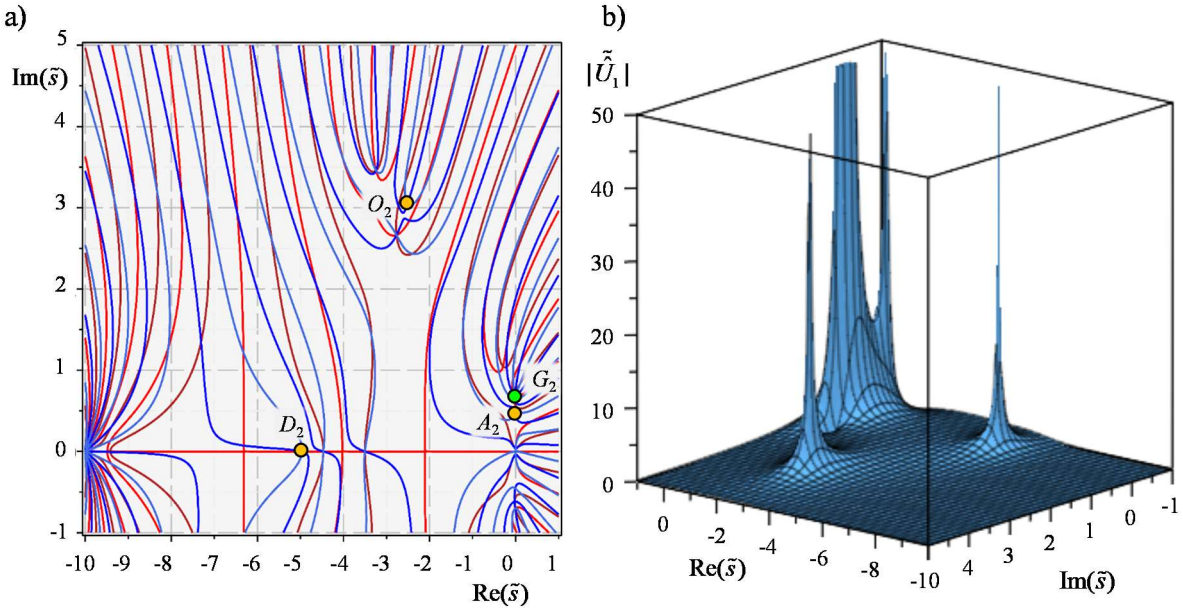

Figure 4.16 Response of the particular metamaterial $\mathcal{M}$ to quasi-resonant force ($\tilde{S}_2 = 0.701\imath$): (a) loci of the null real and null imaginary parts of the displacement component $\tilde{\hat{U}}_1$-numerator (curves in red-scale) and $\tilde{\hat{U}}_1$-denominator (curves in blue-scale), (b) magnitude of $\tilde{\hat{U}}_1$.

In Figure 4.16, the non-dimensional component $\tilde{\hat{U}}_1$ is reported versus the real and imaginary parts of the frequency $\tilde{s}$ for the wavevector $\tilde{\mathbf{k}}_0 = (1\ 0)^T$, if the external forces are characterized by the forcing frequency $\tilde{S}_2 = 0.701\imath$ and unitary amplitudes. In this case the forcing frequency quasi-resonates with one of the metamaterial frequencies. Again, four poles in the forced response of displacement component $\hat{U}_1$ can be detected (Figure 4.16a). As expected, the pole associated to the forcing frequency (point G_2 marked by green dot) is found to lie in the closeness of a characteristic pole (point A_2 marked by yellow dot) of the material. The magnitude of the complex-valued component $\hat{U}_1$ is found to rapidly but continuously grow up in the closeness of all the poles (and their complex conjugates), approaching infinite values (Figure 4.16b). In correspondence of the two close poles, the quasi-resonance condition is found to determine the mutual interaction between a pair of undistinguishable peaks.

ase velocity, defined by the relation (2.7), associated to the points P1 and P2, assumes the values monic force with complex frequency S, the double anti-transform should be applied to determine the displacement vector $\mathbf{U}(S,t)$. Without loss of generality, the anti-transform (4.18) can be applied to the integrand function $\hat{\mathbf{U}}(S_1,\mathbf{k}_1,s)$ of the space-discrete Fourier anti-transform for a single selected value $\mathbf{k}_1$ of the wavevector, for the sake of simplicity. According to this idea, the real and imaginary parts of the first anti-transformed component $U_1(\mathbf{k}_1,t) = \mathcal{L}^{-1}\left[\hat{U}_1(S_1,\mathbf{k}_1,s)\right]$ of the vector $\hat{\mathbf{U}}(S_1,\mathbf{k}_1,s)$ can be analyzed. In Figure 4.17, the time-histories of the non-dimensional real and imaginary parts $\mathrm{Re}\left(\tilde{U}_1(\tilde{\mathbf{k}}_1,\tau)\right)$ and $\mathrm{Im}\left(\tilde{U}_1(\tilde{\mathbf{k}}_1,\tau)\right)$ are reported in the non-dimensional τ-time domain for $\tilde{\mathbf{k}}_1 = (\pi\ \ 0)^T$.

Two different time-histories are compared, corresponding to a harmonic non-decaying external force (with purely imaginary frequency $S_1 = 3\imath$) and a harmonically decaying external force (with complex frequency $S_1 = -1/100 + 3\imath$), respectively. The comparison shows that – after a short transient – the

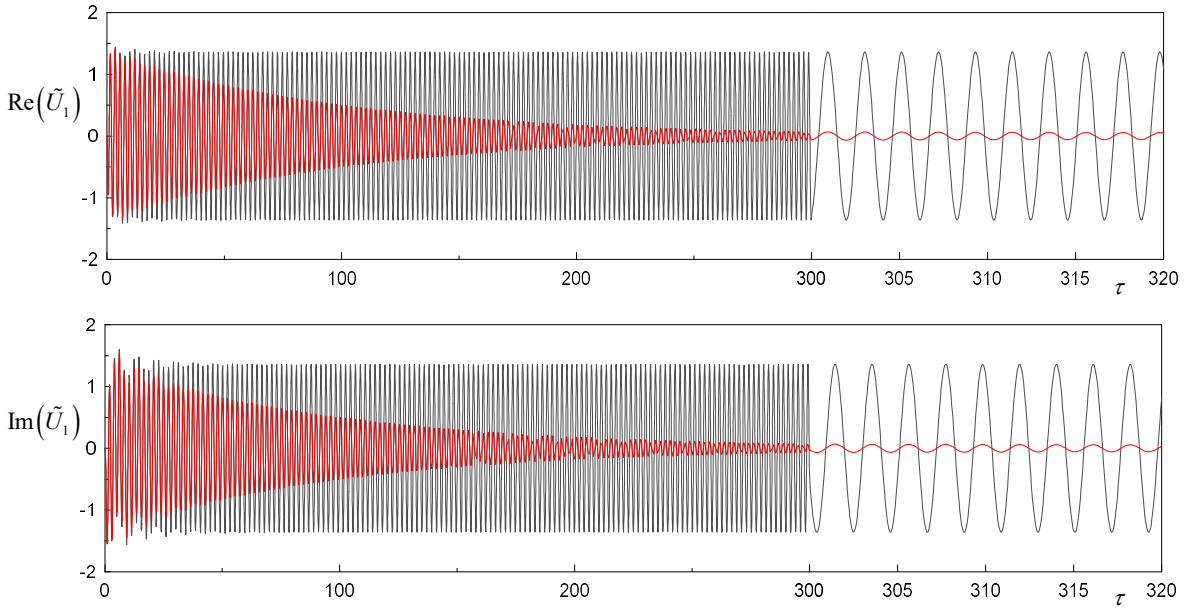

Figure 4.17 Time domain response of the particular metamaterial $\mathcal{M}$ to harmonically non-decaying external force ($\tilde{S}_1 = 3\imath$, gray curves) and harmonically decaying external force ($\tilde{S}_1 = -1/100 + 3\imath$, red curves) at fixed wavevector $\tilde{\mathbf{k}}_1 = (\pi \;\; 0)^T$: (a) non-dimensional real part of $\tilde{U}_1(\tilde{\mathbf{k}}_1, \tau)$; (b) non-dimensional imaginary part of $\tilde{U}_1(\tilde{\mathbf{k}}_1, \tau)$.

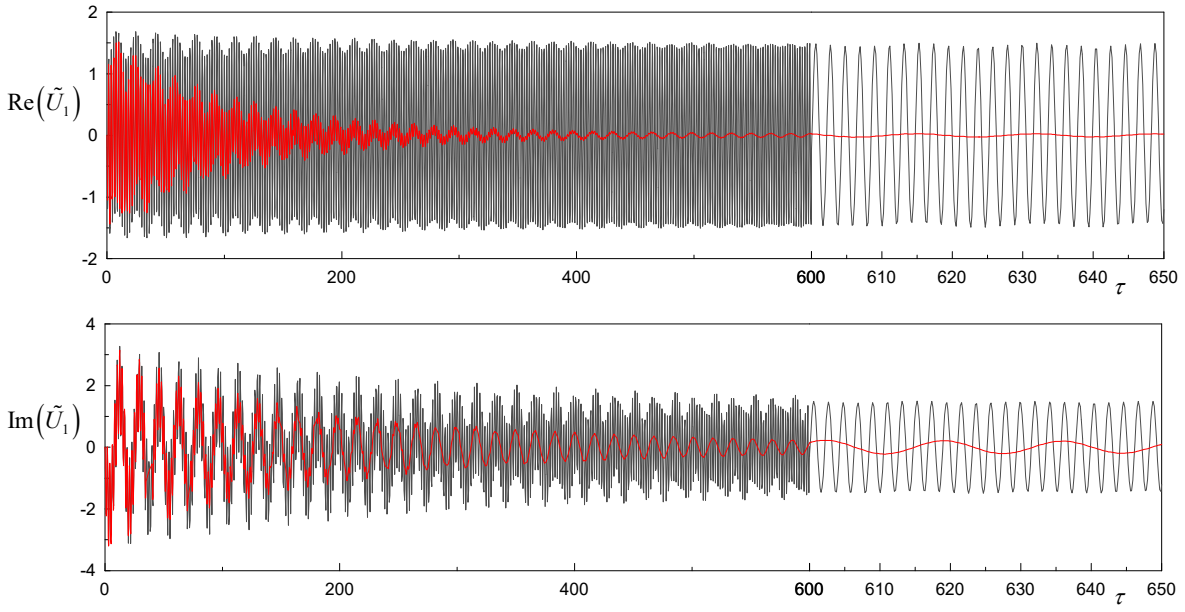

Figure 4.18 Time domain response of the particular metamaterial $\mathcal{M}$ to harmonically non-decaying external force ($\tilde{S}_1 = 3\imath$, gray curves) and harmonically decaying external force ($\tilde{S}_1 = -1/100 + 3\imath$, red curves) at fixed wavevector $\tilde{\mathbf{k}}_1 = (\pi/4 \;\; 0)^T$: (a) non-dimensional real part of $\tilde{U}_1(\tilde{\mathbf{k}}_1, \tau)$; (b) non-dimensional imaginary part of $\tilde{U}_1(\tilde{\mathbf{k}}_1, \tau)$.

stationary damped response to the non-decaying external force (gray time histories) oscillates with constant amplitude at the frequency of the external force. On the contrary, the damped response to the decaying external force (red time histories) oscillates with exponentially decreasing amplitudes. No

significant differences can be detected in the amplitudes of the real and imaginary parts of the complex valued response, whose respective phases are in quadrature, as expected. In Figure 4.18, the time-histories of the non-dimensional real and imaginary parts $\mathrm{Re}\left(\tilde{U}_1(\tilde{\mathbf{k}}_1,\tau)\right)$ and $\mathrm{Im}\left(\tilde{U}_1(\tilde{\mathbf{k}}_1,\tau)\right)$ are reported for $\tilde{\mathbf{k}}_1 = (\pi/4 \;\; 0)^T$. Again, two different time-histories are considered, corresponding to the harmonic non-decaying external force (with $S_1 = 3\imath$) and the harmonically decaying external force (with $S_1 = -1/100 + 3\imath$), respectively. The comparison shows that – after a significantly longer transient – the damped response to the non-decaying external force (gray time histories) tends to stationary oscillations with constant amplitude. The damped response to the decaying external force (red time histories) shows a long transient regime of oscillations, again with decreasing amplitudes.

CHAPTER 5

CONCLUSIONS

In chapter 2, the dispersion properties of monodimensional crystal lattices has been studied distinguishing between the lattice with monoatomic cell and the one with biatomic cell, including the mass-in-mass lattice, with focus on the effects that the presence of a viscoelastic device causes on the dispersive properties of the material. For damped material, the dispersion spectrum is characterized by complex-valued frequencies.

In chapter 3, a general mechanical formulation has been presented for describing the linear wave dynamics of non-dissipative beam lattice materials, characterized by a periodic cellular microstructure composed by a geometrically repetitive pattern of rings interconnected by flexible ligaments. The propagation of the Bloch waves in the bidimensional infinite material domain has been studied using three different models (beam lattice model, first order continuum model and homogenized micropolar continuum model) and a good agreement has been obtained by the comparison of the dispersion spectrum. Parametric analyses of the dispersion spectrum for a periodic tetrachiral material have been carried out for different values of geometric and mechanical parameters, with focus on how these differences affect the dispersion spectrum. The analyses obtained by varying the geometric parameters highlight some issues in satisfying the conditions of the existence of a full band gap in the low-frequency range. These conditions are related to the inertial characteristics of the ring and the slenderness of the ligaments and the physical realization would require a technical arrangement like a material with functionally-graded structural properties with tapered cross section or other modifications that destroy the invariant properties in the out-of-plane direction. The possibility to achieve a band gap at a target frequency has been analyzed enlarging the parameter space or removing some hypotheses of the reference model. In some cases, an enrichment of the low-frequency range with new dispersion curves has been observed. For a cell with massive ligaments, these curves are related to local waveforms, participating essentially by the ligaments dynamics. Furthermore, increasing the mass density of the ligaments it is possible to obtain, between the optic curves, a total band gap in the low-frequency range around the target center frequency. The opening of a full band gap has been observed also for a tetrachiral material with an intra-ring heavy filler and ligaments made by two material with different Young's Modulus. Increasing the ratio between the Young's Moduli of the ligaments the frequencies of the optical curves grow up and increasing the mass density of the intra-ring filler a total band gap between the second acoustic curves and the first optic curves in the low-frequency range has been observed. The optimization problem for the tetrachiral material has been studied and it is found that the problem does not admit solutions corresponding to full band gaps in the admissible parameter space. Partial band gaps are found by reformulating the optimization problem to obtaining the highest amplitude stop band at the lowest center frequency.

In chapter 4, the non-dissipative microstructure of a beam lattice has been enriched by introducing auxiliary dissipative oscillators, housed by the periodic rings and purposely tuned to realize an acoustic viscoelastic metamaterial by exploiting the dynamic mechanism of local resonance. Each auxiliary

oscillator, or resonator, has been viscoelastically coupled with the hosting ring. As peculiar aspect, the viscoelastic ring-resonator coupling has been derived by a proper mathematical formulation based on the Boltzmann superposition integral, whose kernel has been expressed by a Prony series. Accordingly, the free damped dynamics of the periodic cell is governed by a linear homogeneous system of integro-differential equations of motion. Therefore, imposing the quasi-periodicity conditions according to the Floquet-Bloch theory and applying the bilateral Laplace transform, a linear coupled system of ordinary differential equations with frequency-dependent coefficients has been ascertained to govern the free damped propagation of Bloch waves. Consequently, the associated nonlinear, non-polynomial eigenproblem has been stated and numerically solved to determine the complex-valued dispersion spectrum of the viscoelastic metamaterial characterized by a quadrilateral periodic cell. The acoustic and optical branches characterizing the complex-valued frequencies of the dispersion spectrum along the triangular boundary of the first Brillouin zone spanned by real-valued wavenumbers have been analyzed. Particularly, the complex spectra corresponding to different Taylor series approximations of the frequency-dependent rational coefficients governing the eigenproblem have been investigated. Finally, the forced dynamics of the viscoelastic metamaterial under the effects of harmonically decaying and non-decaying waves of external single frequency forces acting on the microstructure has been investigated. The metamaterial response has been determined and parametrically analyzed in terms of dynamic compliance matrices and displacement components, both in the frequency and the time domains.

Based on the work done, the following concluding remarks can be synthesized:

- Some limits in satisfying the conditions of the existence of a full band gap in the low-frequency range by variating the geometric parameters of the microstructured material have been observed. However, the actual possibility to achieve a band gap at a target frequency by enlarging the parameter space or removing some hypotheses of the reference model has been verified. The variation of the mechanic parameters causes changes on the band gap amplitude and on the center frequency and, therefore, the controlled variation of these parameters can be considered a proper mechanical tuning of the phononic filter realized by tetrachiral material.
- The dispersion spectrum is characterized by complex-valued dispersion functions for acoustic metamaterial with viscoelastic resonators. The classic eigenproblem and the complex spectrum associated to the standard dynamic equations with linear viscous damping have been recovered at the first-order approximation of the relaxation function. Due to the non-polynomial nature of the eigenproblem coefficients, the exact eigensolution is characterized by a number of complex spectral branches that can exceed the discrete model dimension. Exceeding spectral branches characterize also the eigensolution for high-order approximations of the eigenproblem coefficients. From a qualitative viewpoint, these exceeding branches have been found to enrich the purely real-valued part of the complex spectrum, corresponding to standing waves that do not propagate in space but are damped in time. Focusing on the propagating waves from a quantitative viewpoint, the exact and approximate eigensolutions shows that low-order approximations may determine non-negligible spectral effects, including the over-estimation or under-estimation of the stop bandwidth separating the acoustic from the optical branches.

- Poles and peaks dominate the complex frequency response functions to harmonic external forces applied to the metamaterial microstructure. These poles can either be related to the characteristic spectral properties of the metamaterial or be associated to the forcing frequency of the decaying or not-decaying external forces. The closeness between the forcing frequency and the branches of the dispersion spectrum determines resonant, quasi-resonant and non-resonant conditions.

From the theoretical viewpoint, future developments could be focused on studying the complex-valued waveforms associated to the spectral frequencies of the viscoelastic metamaterials. Indeed, these dispersion properties are fundamental spectral variables to determine both descriptive quantities, like the polarization factors of the wavefronts, and physical entities, like the directional fluxes of the mechanical energy transferred by the propagating waves (Bacigalupo and Lepidi, 2018). Moving from the standpoint of the beam lattice formulation in Chapter 4, the qualitative and quantitative effects of viscoelasticity on the energy flux flowing in non-conservative beam lattice metamaterials can be considered an affordable matter of study. In order to confirm the theoretical findings, instead, high-fidelity computational analyses are still required to verify the qualitative phenomena and quantitative results characterizing the forced response of the viscoelastic beam lattice metamaterials. In this respect, a supplementary effort to achieve small-scale experimental verifications would also be desiderable. To this purpose, hybrid systems that allow a realible physical-numerical simulation of the wave propagation through an infinite domain, by consistently overcoming the operational limit of finite experimental domains, is a promising frontier (Becker et al., 2018; van Manen et al., 2018). Finally, looking at the stimulating perspectives of modern microengineering design, a challenging task consists in the parametric multi-objective optimization of the viscoelastic metamaterial. Indeed, optimal physical realizations require solving a constrained optimization problem – perhaps by means of suited nonlinear programming techniques (Bacigalupo et al., 2019b) –, in which the admissible ranges of all the microstructural design variables are fixed consistently with the ingredient materials available to build the multi-phase viscoelastic metamaterial.

REFERENCES

Abramovitch, H., Burgard, M., Edery-Azulay, L., Evans, K.E., Hoffmeister, M., Miller, W., Scarpa, F., Smith, C.W., and Tee, K.F. (2010). Smart tetrachiral and hexachiral honeycomb: Sensing and impact detection. Composites Science and Technology, 70(7), 1072-1079.

Achenbach, J. (2012). Wave propagation in elastic solids (Vol. 16). Elsevier.

Alderson, A., Alderson, K.L., Attard, D., Evans, K.E., Gatt, R., Grima, J.N., Miller, W., Ravirala, N., Smith, C.W., and Zied, K. (2010). Elastic constants of 3-, 4- and 6-connected chiral and anti-chiral honeycombs subject to uniaxial in-plane loading. Composites Science and Technology, 70(7), 1042-1048.

Amosov, A., Kostin, I., Panasenko, G., and Smyshlyaev, V.P. (2013). Homogenization of a thermo-chemo-viscoelastic Kelvin-Voigt model. Journal of Mathematical Physics, 54(8), 081501.

Andreassen, E., and Jensen, J.S. (2013). Analysis of phononic bandgap structures with dissipation. Journal of Vibration and Acoustics, 135(4), 041015.

Ashby, M.F., Evans, T., Fleck, N.A., Hutchinson, J.W., Wadley, H.N.G., and Gibson, L.J. (2000). Metal foams: a design guide. Elsevier.

Auricchio, F., Bacigalupo, A., Gambarotta, L., Lepidi, M., Morganti, S., and Vadalà, F. (2019). A novel layered topology of auxetic materials based on the tetrachiral honeycomb microstructure. Materials & Design, 107883.

Babych, N.O., Kamotski, I.V., and Smyshlyaev, V.P. (2008). Homogenization of spectral problems in bounded domains with doubly high contrasts. Networks & Heterogeneous Media, 3(3), 413.

Bacigalupo, A., and De Bellis, M.L. (2015). Auxetic anti-tetrachiral materials: equivalent elastic properties and frequency band-gaps. Composite Structures, 131, 530-544.

Bacigalupo, A., and Gambarotta, L. (2014a). Homogenization of periodic hexa-and tetrachiral cellular solids. Composite Structures, 116, 461-476.

Bacigalupo, A., and Gambarotta, L. (2014b). Second-gradient homogenized model for wave propagation in heterogeneous periodic media. International Journal of Solids and Structures, 51(5), 1052-1065.

Bacigalupo, A., and Gambarotta, L. (2016). Simplified modelling of chiral lattice materials with local resonators. International Journal of Solids and Structures, 83, 126-141.

Bacigalupo, A., and Gambarotta, L. (2017a). Wave propagation in non-centrosymmetric beam-lattices with lumped masses: Discrete and micropolar modeling. International Journal of Solids and Structures, 118, 128-145.

Bacigalupo, A., and Gambarotta, L. (2017b). Dispersive wave propagation in two-dimensional rigid periodic blocky materials with elastic interfaces. Journal of the Mechanics and Physics of Solids, 102, 165-186.

Bacigalupo, A., and Gambarotta, L. (2017c). Damped Bloch Waves in Lattices Metamaterials with Inertial Resonators. Procedia engineering, 199, 1441-1446.

Bacigalupo, A., and Gambarotta, L. (2019). Generalized micropolar continualization of 1D beam lattices. International Journal of Mechanical Sciences, 155, 554-570.

Bacigalupo, A., Gambarotta, L., Lepidi, M., and Vadalà, F. (2019a). Acoustic waveguide filters made up of rigid stacked materials with elastic joints. Meccanica, 54(13), 2039-2052.

Bacigalupo, A., Gnecco, G., Lepidi, M., and Gambarotta, L. (2017). Optimal design of low-frequency band gaps in anti-tetrachiral lattice meta-materials. Composites Part B: Engineering, 115, 341-359.

Bacigalupo, A., and Lepidi, M. (2016). High-frequency parametric approximation of the Floquet-Bloch spectrum for anti-tetrachiral materials. International Journal of Solids and Structures, 97, 575-592.

Bacigalupo, A., and Lepidi, M. (2018). Acoustic wave polarization and energy flow in periodic beam lattice materials. International Journal of Solids and Structures, 147, 183-203.

Bacigalupo, A., Lepidi, M., Gnecco, G., and Gambarotta, L. (2016). Optimal design of auxetic hexachiral metamaterials with local resonators. Smart Materials and Structures, 25(5), 054009.

Bacigalupo, A., Lepidi, M., Gnecco, G., Vadalà, F., and Gambarotta, L. (2019b). Optimal design of the band structure for beam lattice metamaterials. Frontiers in Materials, 6, 2.

Becker, T.S., van Manen, D.J., Donahue, C.M., Bärlocher, C., Börsing, N., Broggini, F., Haag, T., Robertsson, J.O.A., Schmidt, D.R., Greenhalgh, S.A., and Blum, T.E. (2018). Immersive wave propagation experimentation: Physical implementation and one-dimensional acoustic results. Physical Review X, 8(3), 031011.

Berger, J.B., Wadley, H.N.G., and McMeeking, R.M. (2017). Mechanical metamaterials at the theoretical limit of isotropic elastic stiffness. Nature, 543(7646), 533.

Bertoldi, K., Vitelli, V., Christensen, J., and van Hecke, M. (2017). Flexible mechanical metamaterials. Nature Reviews Materials, 2(11), 17066.

Bigoni, D., Gei, M., and Movchan, A.B. (2008). Dynamics of a prestressed stiff layer on an elastic half space: filtering and band gap characteristics of periodic structural models derived from long-wave asymptotics. Journal of the Mechanics and Physics of Solids, 56(7), 2494-2520.

Bigoni, D., Guenneau, S., Movchan, A.B., and Brun, M. (2013). Elastic metamaterials with inertial locally resonant structures: Application to lensing and localization. Physical Review B, 87(17), 174303.

Bloch, F. (1929). Über die quantenmechanik der elektronen in kristallgittern. Zeitschrift für physik, 52(7-8), 555-600.

Brillouin, L. (1946). Wave propagation in periodic structures: electric filters and crystal lattices. Dover Publications, New York.

Brun, M., Movchan, A.B., & Slepyan, L.I. (2013). Transition wave in a supported heavy beam. Journal of the Mechanics and Physics of Solids, 61(10), 2067-2085.

Brunet, T., Merlin, A., Mascaro, B., Zimny, K., Leng, J., Poncelet, O., Aristégui, C., and Mondain-Monval, O. (2015). Soft 3D acoustic metamaterial with negative index. Nature Materials, 14(4), 384.

Cabras, L., and Brun, M. (2014). Auxetic two-dimensional lattices with Poisson's ratio arbitrarily close to -1. Proceedings of the Royal Society A: Mathematical, Physical and Engineering Sciences, 470(2172), 20140538.

Carcione, J.M. (2007). Wave fields in real media: Wave propagation in anisotropic, anelastic, porous and electromagnetic media (Vol. 38). Elsevier.

Carta, G., Brun, M., Movchan, A.B., Movchan, N.V., and Jones, I.S. (2014). Dispersion properties of vortex-type monatomic lattices. International Journal of Solids and Structures, 51(11-12), 2213-2225.

Carta, G., Brun, M., and Baldi, A. (2016). Design of a porous material with isotropic negative Poisson's ratio. Mechanics of Materials, 97, 67-75.

Chen, B.G.G., Liu, B., Evans, A.A., Paulose, J., Cohen, I., Vitelli, V., and Santangelo, C.D. (2016). Topological mechanics of origami and kirigami. Physical Review Letters, 116(13), 135501.

Chen, Y.J., Scarpa, F., Liu, Y.J., and Leng, J.S. (2013). Elasticity of anti-tetrachiral anisotropic lattices. International Journal of Solids and Structures, 50(6), 996-1004.

Chen, Z., Guo, B., Yang, Y., and Cheng, C. (2014). Metamaterials-based enhanced energy harvesting: A review. Physica B: Condensed Matter, 438, 1-8.

Cheung, K.C., Tachi, T., Calisch, S., and Miura, K. (2014). Origami interleaved tube cellular materials. Smart Materials and Structures, 23(9), 094012.

Christensen, R. (2012). Theory of viscoelasticity: an introduction. Elsevier.

Christensen P.W. and Klarbring A. (2004). An Introduction to Structural Optimization. Berlin: Springer.

Cicala, G., Recca, G., Oliveri, L., Perikleous, Y., Scarpa, F., Lira, C., Lorato, A., Grube, D.J., and Ziegmann, G. (2012). Hexachiral truss-core with twisted hemp yarns: Out-of-plane shear properties. Composite Structures, 94(12), 3556-3562.

Colquitt, D.J., Brun, M., Gei, M., Movchan, A.B., Movchan, N.V., and Jones, I.S. (2014). Transformation elastodynamics and cloaking for flexural waves. Journal of the Mechanics and Physics of Solids, 72, 131-143.

COMSOL Multiphysics User's Guide 2019.

Craster, R.V., and Guenneau, S. (Eds.). (2012). Acoustic metamaterials: Negative refraction, imaging, lensing and cloaking (Vol. 166). Springer Science & Business Media.

Craster, R.V., Kaplunov, J., and Pichugin, A.V. (2010). High-frequency homogenization for periodic media. Proceedings of the Royal Society A: Mathematical, Physical and Engineering Sciences, 466(2120), 2341-2362.

Cummer, S.A., Christensen, J., and Alù, A. (2016). Controlling sound with acoustic metamaterials. Nature Reviews Materials, 1(3), 16001.

De Bellis, M.L., Bacigalupo, A., and Zavarise, G. (2019). Characterization of hybrid piezoelectric nanogenerators through asymptotic homogenization. Computer Methods in Applied Mechanics and Engineering, 355, 1148-1186.

Del Toro, R., Bacigalupo, A., AND Paggi, M. (2019). Characterization of wave propagation in periodic viscoelastic materials via asymptotic-variational homogenization. International Journal of Solids and Structures, 172, 110-146.

DePauw, D., Al Ba'ba'a, H., and Nouh, M. (2018). Metadamping and energy dissipation enhancement via hybrid phononic resonators. Extreme Mechanics Letters, 18, 36-44.

Dirrenberger, J., Forest, S., and Jeulin, D. (2013). Effective elastic properties of auxetic microstructures: anisotropy and structural applications. International Journal of Mechanics and Materials in Design, 9(1), 21-33.

Dobrzynski, L., Djafari-Rouhani, B., and Duparc, O.H. (1984). Theory of surface phonons in superlattices. Physical Review B, 29(6), 3138.

Dowling, J.P. (1992). Sonic band structure in fluids with periodic density variations. The Journal of the Acoustical Society of America, 91(5), 2539-2543.

Drugan, W.J. (2017). Wave propagation in elastic and damped structures with stabilized negative-stiffness components. Journal of the Mechanics and Physics of Solids, 106, 34-45.

Evans, K.E. (1991). Auxetic polymers: a new range of materials. Endeavour, 15(4), 170-174.

Farzbod, F., and Leamy, M.J. (2011). Analysis of Bloch's method in structures with energy dissipation. Journal of Vibration and Acoustics, 133(5), 051010.

Ferry J.D., (1980). Viscoelastic properties of polymers. John Wiley & Sons.

Fleck, N.A., Deshpande, V.S., and Ashby, M.F. (2010). Micro-architectured materials: past, present and future. Proceedings of the Royal Society A: Mathematical, Physical and Engineering Sciences, 466(2121), 2495-2516.

Floquet, G. (1883). Sur les équations différentielles linéaires à coefficients périodiques. In Annales Scientifiques de l'École Normale Supérieure (Vol. 12, pp. 47-88).

Gatt, R., Attard, D., Farrugia, P. S., Azzopardi, K.M., Mizzi, L., Brincat, J.P., and Grima, J.N. (2013). A realistic generic model for anti-tetrachiral systems. Physica Status Solidi (b), 250(10), 2012-2019.

Gei, M. (2010). Wave propagation in quasiperiodic structures: stop/pass band distribution and prestress effects. International journal of solids and structures, 47(22-23), 3067-3075.

Gibson, L.J., Ashby, M.F., Schajer, G.S., and Robertson, C.I. (1982). The mechanics of two-dimensional cellular materials. Proceedings of the Royal Society of London. A. Mathematical and Physical Sciences, 382(1782), 25-42.

Gibson, L.J., and Ashby, M.F. (1999). Cellular solids: structure and properties. Cambridge University Press.

Gong, L., and Kyriakides, S. (2006). On the crushing stress of open cell foams. Journal of Applied Mechanics, 73(5), 807-814.

Green, A.E., and Naghdi, P.M. (1964). A general theory of an elastic-plastic continuum (No. AM-64-16). California Univ Berkeley Inst of Engineering Research.

Guenneau, S., Movchan, A., Pétursson, G., and Ramakrishna, S.A. (2007). Acoustic metamaterials for sound focusing and confinement. New Journal of Physics, 9(11), 399.

Haslinger, S.G., Movchan, N.V., Movchan, A.B., Jones, I.S., and Craster, R.V. (2017). Controlling flexural waves in semi-infinite platonic crystals with resonator-type scatterers. The Quarterly Journal of Mechanics and Applied Mathematics, 70(3), 216-247.

Hong-Gang, Z., Yao-Zong, L., Ji-Hong, W., Dian-Long, Y., Gang, W., and Xi-Sen, W. (2006). Sound absorption of locally resonant sonic materials. Chinese Physics Letters, 23(8), 2132.

Hsu, J.C., and Wu, T.T. (2007). Lamb waves in binary locally resonant phononic plates with two-dimensional lattices. Applied Physics Letters, 90(20), 201904.

Huang, H.H., Sun, C.T., and Huang, G.L. (2009). On the negative effective mass density in acoustic metamaterials. International Journal of Engineering Science, 47(4), 610-617.

Hussein, M.I. (2009). Theory of damped Bloch waves in elastic media. Physical Review B, 80(21), 212301.

Hussein, M.I., and Frazier, M.J. (2013). Metadamping: An emergent phenomenon in dissipative metamaterials. Journal of Sound and Vibration, 332(20), 4767-4774.

Hussein, M.I., Leamy, M.J., and Ruzzene, M. (2014). Dynamics of phononic materials and structures: Historical origins, recent progress, and future outlook. Applied Mechanics Reviews, 66(4), 040802.

Jang, W.Y., Kraynik, A.M., and Kyriakides, S. (2008). On the microstructure of open-cell foams and its effect on elastic properties. International Journal of Solids and Structures, 45(7-8), 1845-1875.

Kadic, M., Milton, G.W., van Hecke, M., and Wegener, M. (2019). 3D metamaterials. Nature Reviews Physics, 1(3), 198-210.

Kamotski, I.V., and Smyshlyaev, V.P. (2019). Bandgaps in two-dimensional high-contrast periodic elastic beam lattice materials. Journal of the Mechanics and Physics of Solids, 123, 292-304.

Khelif, A., Achaoui, Y., Benchabane, S., Laude, V., and Aoubiza, B. (2010). Locally resonant surface acoustic wave band gaps in a two-dimensional phononic crystal of pillars on a surface. Physical Review B, 81(21), 214303.

Khelif, A., Aoubiza, B., Mohammadi, S., Adibi, A., and Laude, V. (2006). Complete band gaps in two-dimensional phononic crystal slabs. Physical Review E, 74(4), 046610.

Khelif, A., Choujaa, A., Benchabane, S., Djafari-Rouhani, B., and Laude, V. (2004). Guiding and bending of acoustic waves in highly confined phononic crystal waveguides. Applied Physics Letters, 84(22), 4400-4402.

Kraynik, A.M., Reinelt, D.A., and van Swol, F. (2004). Structure of random foam. Physical Review Letters, 93(20), 208301.

Krushynska, A.O., Kouznetsova, V.G., and Geers, M.G.D. (2016). Visco-elastic effects on wave dispersion in three-phase acoustic metamaterials. Journal of the Mechanics and Physics of Solids, 96, 29-47.

Kunin, I.A. (2012). Elastic media with microstructure I: one-dimensional models (Vol. 26). Springer Science & Business Media.

Kushwaha, M.S., Halevi, P., Dobrzynski, L., and Djafari-Rouhani, B. (1993). Acoustic band structure of periodic elastic composites. Physical Review Letters, 71(13), 2022.

Lakes, R. (2009). Viscoelastic materials. Cambridge University Press.

Langley, R.S. (1994). On the modal density and energy flow characteristics of periodic structures. Journal of Sound and Vibration, 172(4), 491-511.

Lee, J.H., Singer, J.P., and Thomas, E.L. (2012). Micro-/nanostructured mechanical metamaterials. Advanced Materials, 24(36), 4782-4810.

Lepidi, M. (2013). Multi-parameter perturbation methods for the eigensolution sensitivity analysis of nearly-resonant non-defective multi-degree-of-freedom systems. Journal of Sound and Vibration, 332(4), 1011-1032.

Lepidi, M., and Bacigalupo, A. (2018). Multi-parametric sensitivity analysis of the band structure for tetrachiral acoustic metamaterials. International Journal of Solids and Structures, 136, 186-202.

Lepidi, M., and Bacigalupo, A. (2018). Parametric design of the band structure for lattice materials. Meccanica, 53(3), 613-628.

Li, J., and Chan, C.T. (2004). Double-negative acoustic metamaterial. Physical Review E, 70(5), 055602.

Liu, X.N., Hu, G.K., Sun, C.T., and Huang, G.L. (2011). Wave propagation characterization and design of two-dimensional elastic chiral metacomposite. Journal of Sound and Vibration, 330(11), 2536-2553.

Liu, X.N., Huang, G.L., and Hu, G.K. (2012). Chiral effect in plane isotropic micropolar elasticity and its application to chiral lattices. Journal of the Mechanics and Physics of Solids, 60(11), 1907-1921.

Liu, Z., Zhang, X., Mao, Y., Zhu, Y.Y., Yang, Z., Chan, C.T., and Sheng, P. (2000). Locally resonant sonic materials. Science, 289(5485), 1734-1736.

Lombardo, M., and Askes, H. (2012). Higher-order gradient continuum modelling of periodic lattice materials. Computational Materials Science, 52(1), 204-208.

Lorato, A., Innocenti, P., Scarpa, F., Alderson, A., Alderson, K.L., Zied, K.M., Raviral, N., Miller W., Smith, C.W., and Evans, K.E. (2010). The transverse elastic properties of chiral honeycombs. Composites Science and Technology, 70(7), 1057-1063.

Lu, M.H., Feng, L., and Chen, Y.F. (2009). Phononic crystals and acoustic metamaterials. Materials Today, 12(12), 34-42.

Luongo, A., and Romeo, F. (2005). Real wave vectors for dynamic analysis of periodic structures. Journal of Sound and Vibration, 279(1-2), 309-325.

Luongo, A., and Ferretti, M. (2015). Can a semi-simple eigenvalue admit fractional sensitivities?. Applied Mathematics and Computation, 255, 165-178.

Lv, C., Krishnaraju, D., Konjevod, G., Yu, H., and Jiang, H. (2014). Origami based mechanical metamaterials. Scientific Reports, 4, 5979.

Ma, G., and Sheng, P. (2016). Acoustic metamaterials: From local resonances to broad horizons. Science Advances, 2(2), e1501595.

Magid, L.M. (1964). Mechanical energy flow in crystal lattices. Physical Review, 134(1A), A158.

Malischewsky, P.G., Lorato, A., Scarpa, F., and Ruzzene, M. (2012). Unusual behaviour of wave propagation in auxetic structures: P-waves on free surface and S-waves in chiral lattices with piezoelectrics. Physica Status Solidi (b), 249(7), 1339-1346.

Manimala, J.M., and Sun, C.T. (2014). Microstructural design studies for locally dissipative acoustic metamaterials. Journal of Applied Physics, 115(2), 023518.

Mead, D.J. (1973). A general theory of harmonic wave propagation in linear periodic systems with multiple coupling. Journal of Sound and Vibration, 27(2), 235-260.

Mead, D.J., and Markuš, Š. (1983). Coupled flexural-longitudinal wave motion in a periodic beam. Journal of Sound and Vibration, 90(1), 1-24.

Mead, D.J. (1996). Wave propagation in continuous periodic structures: research contributions from Southampton, 1964–1995. Journal of Sound and Vibration, 190(3), 495-524.

Merheb, B., Deymier, P.A., Jain, M., Aloshyna-Lesuffleur, M., Mohanty, S., Berker, A., and Greger, R.W. (2008). Elastic and viscoelastic effects in rubber/air acoustic band gap structures: A theoretical and experimental study. Journal of Applied Physics, 104(6), 064913.

Meza, L.R., Zelhofer, A.J., Clarke, N., Mateos, A.J., Kochmann, D.M., and Greer, J.R. (2015). Resilient 3D hierarchical architected metamaterials. Proceedings of the National Academy of Sciences, 112(37), 11502-11507.

Mindlin, R.D. (1963). Microstructure in linear elasticity (No. TR-50). Columbia Univ New York Dept of Civil Engineering and Engineering Mechanics.

Misseroni, D., Colquitt, D.J., Movchan, A.B., Movchan, N.V., and Jones, I.S. (2016). Cymatics for the cloaking of flexural vibrations in a structured plate. Scientific Reports, 6, 23929.

Moiseyenko, R.P., and Laude, V. (2011). Material loss influence on the complex band structure and group velocity in phononic crystals. Physical Review B, 83(6), 064301.

Morini, L., and Gei, M. (2018). Waves in one-dimensional quasicrystalline structures: dynamical trace mapping, scaling and self-similarity of the spectrum. Journal of the Mechanics and Physics of Solids, 119, 83-103.

Movchan, A.B., and Slepyan, L.I. (2014). Resonant waves in elastic structured media: dynamic homogenisation versus Green's functions. International Journal of Solids and Structures, 51(13), 2254-2260.

Mukherjee, S., and Lee, E.H. (1975). Dispersion relations and mode shapes for waves in laminated viscoelastic composites by finite difference methods. Computers & Structures, 5(5-6), 279-285.

Neville, R. M., Scarpa, F., and Pirrera, A. (2016). Shape morphing Kirigami mechanical metamaterials. Scientific Reports, 6, 31067.

Niederreiter, H. (1992). Random number generation and quasi-Monte Carlo methods (Vol. 63). Siam.

Oudich, M., Assouar, M.B., and Hou, Z. (2010). Propagation of acoustic waves and waveguiding in a two-dimensional locally resonant phononic crystal plate. Applied Physics Letters, 97(19), 193503.

Overvelde, J.T., Weaver, J.C., Hoberman, C., and Bertoldi, K. (2017). Rational design of reconfigurable prismatic architected materials. Nature, 541(7637), 347.

Paley, R.E.A.C., and Wiener, N. (1934). Fourier transforms in the complex domain (Vol. 19). American Mathematical Soc..

Pennec, Y., Djafari-Rouhani, B., Larabi, H., Vasseur, J.O., and Hladky-Hennion, A.C. (2008). Low-frequency gaps in a phononic crystal constituted of cylindrical dots deposited on a thin homogeneous plate. Physical Review B, 78(10), 104105.

Phani, A.S., and Hussein, M.I. (2013). Analysis of damped Bloch waves by the Rayleigh perturbation method. Journal of Vibration and Acoustics, 135(4), 041014.

Phani, A.S., Woodhouse, J., and Fleck, N.A. (2006). Wave propagation in two-dimensional periodic lattices. The Journal of the Acoustical Society of America, 119(4), 1995-2005.

Piccardo, G., Tubino, F., and Luongo, A. (2019). Equivalent timoshenko linear beam model for the static and dynamic analysis of tower buildings. Applied Mathematical Modelling, 71, 77-95.

Pierre, C., Castanier, M.P., and Chen, W.J. (1996). Wave localization in multi-coupled periodic structures: application to truss beams. 68-86.

Prall, D., and Lakes, R.S. (1997). Properties of a chiral honeycomb with a Poisson's ratio of -1. International Journal of Mechanical Sciences, 39(3), 305-314.

Rashed, M.G., Ashraf, M., Mines, R.A.W., and Hazell, P.J. (2016). Metallic microlattice materials: A current state of the art on manufacturing, mechanical properties and applications. Materials & Design, 95, 518-533.

Reda, H., Ganghoffer, J. F., and Lakiss, H. (2017). Micropolar dissipative models for the analysis of 2D dispersive waves in periodic lattices. Journal of Sound and Vibration, 392, 325-345.

Reda, H., Rahali, Y., Ganghoffer, J.F., and Lakiss, H. (2016). Wave propagation in 3D viscoelastic auxetic and textile materials by homogenized continuum micropolar models. Composite Structures, 141, 328-345.

Ren, X., Das, R., Tran, P., Ngo, T.D., and Xie, Y.M. (2018). Auxetic metamaterials and structures: a review. Smart Materials and Structures, 27(2), 023001.

Romeo, F., and Luongo, A. (2002). Invariant representation of propagation properties for bi-coupled periodic structures. Journal of Sound and Vibration, 257(5), 869-886.

Romeo, F., and Luongo, A. (2003). Vibration reduction in piecewise bi-coupled periodic structures. Journal of Sound and Vibration, 268(3), 601-615.

Rosi, G., and Auffray, N. (2016). Anisotropic and dispersive wave propagation within strain-gradient framework. Wave Motion, 63, 120-134.

Sainidou, R., Djafari-Rouhani, B., Pennec, Y., and Vasseur, J.O. (2006). Locally resonant phononic crystals made of hollow spheres or cylinders. Physical Review B, 73(2), 024302

Scarpa, F., Ouisse, M., Collet, M., and Saito, K. (2013). Kirigami auxetic pyramidal core: mechanical properties and wave propagation analysis in damped lattice. Journal of Vibration and Acoustics, 135(4), 041001.

Schaedler, T.A., and Carter, W.B. (2016). Architected cellular materials. Annual Review of Materials Research, 46, 187-210.

Sha, Y., Jiani, L., Haoyu, C., Ritchie, R.O., and Jun, X. (2018). Design and strengthening mechanisms in hierarchical architected materials processed using additive manufacturing. International Journal of Mechanical Sciences, 149, 150-163.

Shyu, T.C., Damasceno, P.F., Dodd, P.M., Lamoureux, A., Xu, L., Shlian, M., Shtein, M., Glotzer, S.C., and Kotov, N.A. (2015). A kirigami approach to engineering elasticity in nanocomposites through patterned defects. Nature Materials, 14(8), 785.

Slepyan, L.I. (2012). Models and phenomena in fracture mechanics. Springer Science & Business Media.

Smith, T.L., Rao, K., and Dyer, I. (1986). Attenuation of plate flexural waves by a layer of dynamic absorbers.

Smyshlyaev, V.P. (2009). Propagation and localization of elastic waves in highly anisotropic periodic composites via two-scale homogenization. Mechanics of Materials, 41(4), 434-447.

Smyshlyaev, V. P., and Cherednichenko, K.D. (2000). On rigorous derivation of strain gradient effects in the overall behaviour of periodic heterogeneous media. Journal of the Mechanics and Physics of Solids, 48(6-7), 1325-1357.

Spadoni, A., Ruzzene, M., Gonella, S., and Scarpa, F. (2009). Phononic properties of hexagonal chiral lattices. Wave motion, 46(7), 435-450.

Svanberg, K. (1987). The method of moving asymptotes - a new method for structural optimization. International Journal for Numerical Methods in Engineering, 24(2), 359-373.

Svanberg, K. (2002). A class of globally convergent optimization methods based on conservative convex separable approximations. SIAM Journal on Optimization, 12(2), 555-573.

Thompson, D.J. (2008). A continuous damped vibration absorber to reduce broad-band wave propagation in beams. Journal of Sound and Vibration, 311(3-5), 824-842.

Vadalà, F., Bacigalupo, A., Lepidi, M., and Gambarotta, L. (2018) Analytical and computational methods for modeling mechanical filters against Bloch wave propagation. Proceedings of the 23rd Conference of the Italian Association of Theoretical and Applied Mechanics 2017. 3:2096–106.

Vadalà, F., Bacigalupo, A., Lepidi, M., and Gambarotta, L. (2018). Bloch wave filtering in tetrachiral materials via mechanical tuning. Composite Structures, 201, 340-351.

Van der Pol, B. (1955). Operational calculus based on the two-sided Laplace integral.

van Manen, D.J., Becker, T.S., Börsing, N., Thomsen, H.R., Moleron, M., and Robertsson, J.O. (2018). Immersive experimentation: A new paradigm for low-frequency acoustic and elastic wave propagation experimentation. The Journal of the Acoustical Society of America, 144(3), 1758-1758.

Volterra, V. (1913). Lecons sur les fonctions de lignes. Paris: Goutier-Villard.

Wang, G., Wen, X., Wen, J., Shao, L., and Liu, Y. (2004). Two-dimensional locally resonant phononic crystals with binary structures. Physical Review Letters, 93(15), 154302.

Wang, P., Casadei, F., Kang, S.H., and Bertoldi, K. (2015). Locally resonant band gaps in periodic beam lattices by tuning connectivity. Physical Review B, 91(2), 020103.

Wei, Z.Y., Guo, Z.V., Dudte, L., Liang, H.Y., and Mahadevan, L. (2013). Geometric mechanics of periodic pleated origami. Physical Review Letters, 110(21), 215501.

Wu, W., Hu, W., Qian, G., Liao, H., Xu, X., and Berto, F. (2019). Mechanical design and multifunctional applications of chiral mechanical metamaterials: A review. Materials & Design, 107950.

Wu, T.T., Huang, Z.G., Tsai, T.C., and Wu, T.C. (2008). Evidence of complete band gap and resonances in a plate with periodic stubbed surface. Applied Physics Letters, 93(11), 111902.

Yang, S., Page, J. H., Liu, Z., Cowan, M.L., Chan, C.T., and Sheng, P. (2004). Focusing of sound in a 3D phononic crystal. Physical Review Letters, 93(2), 024301.

Yu, D., Liu, Y., Wang, G., Zhao, H., and Qiu, J. (2006). Flexural vibration band gaps in Timoshenko beams with locally resonant structures. Journal of Applied Physics, 100(12), 124901.

Zadpoor, A.A. (2019). Meta-biomaterials. Biomaterials Science.

Zhao, Y. P., and Wei, P.J. (2009). The band gap of 1D viscoelastic phononic crystal. Computational Materials Science, 46(3), 603-606.

Zheng, X., Lee, H., Weisgraber, T.H., Shusteff, M., DeOtte, J., Duoss, E.B., Kuntz, J.D., Biener M.M., Ge Q., Jackson J.A., Kucheyev, S.O. Fang N.X., and Spadaccini C.M. (2014). Ultralight, ultrastiff mechanical metamaterials. Science, 344(6190), 1373-1377.

Zhu, D., Huang, X., Hua, H., and Zheng, H. (2016). Vibration isolation characteristics of finite periodic tetra-chiral lattice coating filled with internal resonators. Proceedings of the Institution of Mechanical Engineers, Part C: Journal of Mechanical Engineering Science, 230(16), 2840-2850.